MICROWAVE AND MILLIMETER-WAVE CONCURRENT MULTIBAND LOW-NOISE AMPLIFIERS AND RECEIVER FRONT-END IN SIGE BICMOS TECHNOLOGY

A Dissertation

by

JAEYOUNG LEE

Submitted to the Office of Graduate and Professional Studies of
Texas A&M University
in partial fulfillment of the requirements for the degree of

DOCTOR OF PHILOSOPHY

Chair of Committee,	Cam Nguyen
Committee Members,	Jose Silva-Martinez
	Chin B. Su
	Ben Zoghi
Head of Department,	Miroslav M. Begovic

August 2015

Major Subject: Electrical Engineering

Copyright 2015 Jaeyoung Lee

ABSTRACT

A fully integrated SiGe BiCMOS concurrent multiband receiver front-end and its building blocks including multiband low-noise amplifiers (LNAs), single-to-differential amplifiers and mixer are presented for various Ku-/K-/Ka-band applications. The proposed concurrent multiband receiver building blocks and receiver front-end achieve the best stopband rejection performances as compared to the existing multiband LNAs and receivers.

First, a novel feedback tri-band load composed of two inductor feedback notch filters is proposed to overcome the low Q-factor of integrated passive inductors, and hence it provides superior stopband rejection ratio (SRR). A new 13.5/24/35-GHz concurrent tri-band LNA implementing the feedback tri-band load is presented. The developed tri-band LNA is the first concurrent tri-band LNA operating up to millimeter-wave region.

By expanding the operating principle of the feedback tri-band load, a 21.5/36.5-GHz concurrent dual-band LNA with an inductor feedback dual-band load and another 23/36-GHz concurrent dual-band LNA with a new transformer feedback dual-band load are also presented. The latter provides more degrees of freedom for the creation of the stopband and passbands as compared to the former.

A 22/36-GHz concurrent dual-band single-to-differential LNA employing a novel single-to-differential transformer feedback dual-band load is presented. The developed LNA is the first true concurrent dual-band single-to-differential amplifier. A novel 24.5/36.5 GHz concurrent dual-band merged single-to-differential LNA and mixer implementing the proposed single-to-differential transformer feedback dual-band load is also presented. With a 21-GHz LO signal, the down-converted dual IF bands are located at 3.5/15.5 GHz for two passband signals at 24.5/36.5 GHz, respectively. The proposed merged LNA and mixer is the first fully integrated concurrent dual-band mixer operating up to millimeter-wave frequencies without using any switching mechanism.

Finally, a 24.5/36.5-GHz concurrent dual-band receiver front-end is proposed. It consists of the developed concurrent dual-band LNA using the single-to-single transformer feedback dual-band load and the developed concurrent dual-band merged LNA and mixer employing the single-to-differential transformer feedback dual-band load. The developed concurrent dual-band receiver front-end achieves the highest gain and the best NF performances with the largest SRRs, while operating at highest frequencies up to millimeter-wave region, among the concurrent dual-band receivers reported to date.

DEDICATION

To my parents and my wife

ACKNOWLEDGEMENTS

I would like to thank my committee chair, Dr. Cam Nguyen, and my committee members, Dr. Jose Silva-Martinez, Dr. Chin B. Su, and Dr. Ben Zoghi, for their guidance and support throughout the course of this research.

Thanks also go to the department faculty and staff for making my time at Texas A&M University a great experience. Thanks to my colleagues, Kyoungwoon Kim, Donghyun Lee, Youngman Um, Sunhwan Jang, Juseok Bae, Yuan Luo, and Chadi Geha. Especially, I wish to thank to my dear friend, Dr. Cuong Huynh, for his insightful discussions and help.

I also want to extend my gratitude to the U.S. Air Force Office of Scientific Research and the U.S. National Institute of Justice as well as Texas A&M University at Qatar and the Qatar National Research Fund (a member of Qatar Foundation) for the financial support of this research. I wish to acknowledge the chip fabrication of TowerJazz Semiconductor and continuous technical support of Rohde & Schwarz.

Finally, I would like to thank to my mother and father for their endless support and encouragement. I am really thankful to my wife, Eunju Park, for her support, patience and devoted love.

TABLE OF CONTENTS

Page

ABSTRACT ···· ii

DEDICATION ···· iv

ACKNOWLEDGEMENTS ···· v

TABLE OF CONTENTS ···· vi

LIST OF FIGURES ···· viii

LIST OF TABLES ···· xiii

CHAPTER

I INTORDUCTION ···· 1

- 1.1 Review of Multiband Receiver Architectures and Multiband LNAs ···· 1
- 1.2 Proposed Concurrent Dual-band Receiver and Multiband LNAs ···· 5

II ANALYSIS AND DESIGN OF CONCURRENT MULTIBAND LOADS ···· 10

- 2.1 Conventional Dual-band Load ···· 10
- 2.2 Conventional Tri-band Load ···· 11
  - 2.2.1 Analysis of Conventional Tri-band Load ···· 12
  - 2.2.2 Design Example of Conventional Tri-band Load ···· 17
- 2.3 Proposed Modified Tri-band Load ···· 20
  - 2.3.1 Analysis of Proposed Modified Tri-band Load ···· 21
  - 2.3.2 Design Example of Proposed Modified Tri-band Load ···· 23
- 2.4 Proposed Feedback Tri-band Load ···· 28
- 2.5 Summary and Conclusion ···· 32

III CONCURRENT TRI-BAND LOW-NOISE AMPLIFIER ···· 33

- 3.1 Design of Concurrent Tri-band Low-Noise Amplifier ···· 33
- 3.2 Experimental and Simulated Results ···· 42
- 3.3 Summary and Conclusion ···· 45

CHAPTER

IV CONCURRENT DUAL-BAND LOW-NOISE AMPLIFIERS 48

- 4.1 Analysis and Design of Concurrent Dual-band Loads 49
  - 4.1.1 Conventional Dual-band Load 49
  - 4.1.2 Proposed Inductor Feedback Dual-band Load 52
  - 4.1.3 Proposed Transformer Feedback Dual-band Load 54
- 4.2 Concurrent Dual-band Low-Noise Amplifiers 56
  - 4.2.1 Design of Dual-band LNAs Employing Proposed Feedback Dual-band Loads 57
  - 4.2.2 Enhancement of Stopband Rejection Performance 61
  - 4.2.3 Control of Stopband Rejection and Gain Balance 64
- 4.3 Experimental and Simulated Results 67
- 4.4 Summary and Conclusion 71

V CONCURRENT DUAL-BAND SINGLE-TO-DIFFERENTIAL LOW-NOISE AMPLIFIER 74

- 5.1 Review of Single-ended Feedback Multiband Loads 76
- 5.2 Design of Single-to-Differential Transformer Feedback Dual-band Load 77
- 5.3 Design of Concurrent Dual-band Single-to-Differential LNA 81
- 5.4 Experimental and Simulated Results 89
- 5.5 Summary and Conclusion 94

VI CONCURRENT DUAL-BAND MERGED LOW-NOISE AMPLIFIER AND MIXER 96

- 6.1 Design of Concurrent Dual-band Merged LNA and Mixer 97
- 6.2 Experimental and Simulated Results 99
- 6.3 Summary and Conclusion 109

VII CONCURRENT DUAL-BAND RECEIVER FRONT-END 111

- 7.1 Design of Concurrent Dual-band Receiver Front-end 111
- 7.2 Experimental and Simulated Results 114
- 7.3 Summary and Conclusion 125

VIII SUMMARY AND CONCLUSION 126

REFERENCES 129

LIST OF FIGURES

FIGURE Page

1.1 Simplified multiband receiver front-end configurations with (a) separate parallel receiver front-ends (with separate antennas), (b) separate antennas and LNAs, (c) separate antennas and wideband or reconfigurable LNA, and (d) single concurrent multiband antenna and LNA. 2

1.2 Proposed concurrent dual-band receiver front-end as part of a double-conversion receiver. 5

2.1 (a) Concurrent dual-band CMOS LNA reported in [5]. (b) Responses of wideband load, notch filter, and dual-band load constructed from the combined wideband load and notch filter. 11

2.2 Tri-band load: (a) conventional, (b) modified, and (c) conceptual construction of tri-band load using a wideband load and two notch filters. ... 12

2.3 Insertion loss for (a) the dual-band notch filter and wideband load for different k, L_1 and C_1, and (b) the conventional tri-band load for different k, L_1 and C_1. 14

2.4 Insertion losses of the modified tri-band load for different k' (a) and various modified tri-band loads in Table 2.3 (b). 26

2.5 Insertion losses of the conventional tri-band load (a) and modified tri-band load (b) as the Q-factor of the integrated inductors is changed from 5 to 30. 27

2.6 Equivalent-circuit models of the feedback tri-band load (a), (b) at node X, and (c) at node Y. f_{Pi} and f_{Sn} are the pass-band and stop-band frequencies, respectively. 29

2.7 Insertion loss and impedance magnitudes of the equivalent circuits at nodes X, Y (a, b) and the feedback tri-band load (c). 30

3.1 Schematic and component values of the new concurrent TBLNA using the feedback tri-band load. 34

3.2 Simulated power gain of the tri-band LNA with and without the out-of-band rejection filter. 37

FIGURE

3.3 Alternative loads of the first stage to verify the effectiveness of the new feedback tri-band load with feedback notches: (a) wideband load by opening node *Y′* and (b) modified tri-band load by grounding node *Y′*. ·················· 38

3.4 Simulated power gain of the tri-band LNA with the feedback tri-band load, modified tri-band load, and wideband load. ······································· 39

3.5 Simulated power gain for different inverting amplifier gain *A* (a) and stopband rejection ratio (SRR) as a function of A (b) of the tri-band LNA. ·· 40

3.6 Die micrograph of the fabricated concurrent tri-band LNA. ···················· 42

3.7 Measured and simulated results for (a) power gain, (b) NF, (c) S_{11} and S_{22}, and (d) S_{12}. ·· 43

3.8 Measured stability factors K and B_1. ··· 44

3.9 Measured input P_{1dB} and input IP_3 at: (a) 13.5 GHz, (b) 24 GHz, and (c) 35 GHz.·· 45

4.1 (a) Conventional and (b) modified dual-band loads. (c) Equivalent circuit of the proposed inductor feedback dual-band load.································· 49

4.2 (a) Transformer-based dual-band load and (b) equivalent circuit of the proposed transformer feedback dual-band load.····································· 55

4.3 Schematic of the concurrent dual-band LNA employing the inductor feedback dual-band load shown in Fig. 4.1(c). ····································· 56

4.4 Schematic of the concurrent dual-band LNA employing the transformer feedback dual-band load shown in Fig. 4.2(b). ····································· 57

4.5 Micrographs of the fabricated concurrent dual-band LNAs: (a) with the inductor feedback dual-band load, (b) with the transformer feedback dual-band load, and (c) zoom-in area of the transformer feedback dual-band load employed in (b). ··· 59

4.6 Power gain (S_{21}) simulation results of the concurrent dual-band LNAs having the inductor (a) and transformer (b) feedback dual-band loads with and without feedback. ·· 62

FIGURE

4.7 (a) Power gain (S_{21}) simulation results of the concurrent dual-band LNA with feedback inductor load for different V_{BE2} from 0.83 V to 0.94 V, (b) passband peak S_{21} and stopband minimum S_{21}, and (c) passband gain imbalance and SRR. 65

4.8 (a) Power gain (S_{21}) simulation results of the concurrent dual-band LNA with feedback transformer load for different V_{BE2} from 0.83 V to 0.94 V, (b) passband peak S_{21} and stopband minimum S_{21}, and (c) passband gain imbalance and SRR. 66

4.9 (a) Measured S_{21} of the concurrent dual-band LNA with feedback inductor load in passbands and stopband. (b) Measured gain imbalance and SRR obtained from (a). 68

4.10 (a) Measured S_{21} of the concurrent dual-band LNA with feedback transformer load in passbands and stopband. (b) Measured gain imbalance and SRR obtained from (a). 68

4.11 Measured and simulated results of the concurrent dual-band LNA with feedback inductor load in high gain and SRR modes: (a) power gain, (b) S_{11}, S_{22}, and S_{12}, and (c) NF. 69

4.12 Measured and simulated results of the concurrent dual-band LNA with feedback transformer load in high gain and SRR modes: (a) power gain, (b) S_{11}, S_{22}, and S_{12}, and (c) NF. 70

5.1 (a) Full equivalent circuit and (b) a half-circuit of the proposed single-input to differential-output transformer feedback dual-band load. 78

5.2 Schematic of the concurrent dual-band single-input to differential-output LNA employing the transformer feedback dual-band load. 81

5.3 (a) Microphotograph of the fabricated concurrent dual-band single-to-differential LNA and (b) Close-up microphotograph around the transformer feedback single-to-differential dual-band load shown in (a). 84

5.4 Transformer 3D EM simulation results for self-inductances (L_{P}, L_{S}), Q-factor (Q_P and Q_S for the respective primary and secondary inductors), and mutual coupling coefficient (K). 85

FIGURE

5.5 Single-ended power gain (S_{21}, S_{31}) simulation results of the concurrent dual-band single-to-differential LNA with and without transformer feedback. 86

5.6 Single-ended power gain (S_{21}, S_{31}) simulation results of the concurrent dual-band single-to-differential LNA for different V_{BE3} from 0.87 V to 1 V with a 0.01-V step. 87

5.7 Measured and simulated single-input to differential-output power gains ($\mathrm{S}_{21,\mathrm{ds}}$) and measured single-input to common-mode gain ($\mathrm{S}_{21,\mathrm{cs}}$). 89

5.8 Measured and simulated results for single-input to single-output: single-ended (S_{21}, S_{31}) power gain (a) and phase (b), differential gain imbalance (c), and differential phase imbalance (d). 90

5.9 Measured and simulated results comparison. (a) NF, (b) measured stability factor, (c) input and output matching (S_{11}, S_{22}, and S_{33}), (d) reverse isolation (S_{12} and S_{13}). 91

5.10 (a) Measured input $\mathrm{P}_{1\mathrm{dB}}$. Measured input IP_3 (IIP_3) at 21.5 GHz (low-passband) (b) and 36 GHz (high-passband) (c). 92

6.1 Schematic of the concurrent dual-band merged LNA and mixer employing the transformer feedback single-to-differential dual-band load. 97

6.2 (a) Microphotograph of the fabricated concurrent dual-band single-to-differential merged LNA and mixer and (b) Close-up microphotograph around the transformer feedback single-to-differential dual-band load shown in (a). 100

6.3 Measured and simulated single-ended conversion gain for Ports 1 to 2 and 1 to 3 (S_{21}, S_{31}): (a) GB mode, (b) SRR mode, and (c) combined conversion gain graphs of GB and SRR modes for comparison. (d) Measured differential gain imbalance between two signal paths ($|S_{21,\mathrm{dB}}| - |S_{31,\mathrm{dB}}|$). 101

6.4 Measured single-ended NF for Ports 1 to 2 and 1 to 3 (NF_{21}, NF_{31}). 102

6.5 Measured and simulated matching responses at: (a) RF input (Port1), (b) IF output (Ports 2 and 3), and (c) LO input (Port 4). 104

FIGURE

6.6 Measured single-ended conversion gain for Ports 1 to 2 and 1 to 3 (S_{21}, S_{31}) as a function of LO power at: (a) high GB mode and (b) high SRR mode. ··· 105

6.7 Measured single-ended conversion gain for Ports 1 to 2 and 1 to 3 (S_{21}, S_{31}) as a function of RF power at: (a) high GB mode and (b) high SRR mode.···· 106

6.8 Measured single-ended input IP_3: $IP_{3,21}$ (a) and $IP_{3,31}$ (b) at high GB mode. $IP_{3,21}$ (c) and $IP_{3,31}$ (d) at high SRR mode. ·· 107

7.1 Developed receiver front-end as part of a concurrent dual-band double-conversion receiver. ·· 112

7.2 Microphotograph of the fabricated concurrent dual-band receiver front-end consisting of the dual-band LNA shown in Fig. 4.4 followed by the dual-band merged LNA and mixer shown in Fig. 6.1. ·························· 114

7.3 Measured single-ended conversion gains of the receiver front-end for S_{21} and S_{31} paths: (a) Rx mode 1 for low-gain, (b) Rx mode 2 for passband gain balance, (c) Rx mode 3 for high-gain, (d) Rx mode 4 for high SRR, and (e) Rx mode 5 for stopband notch balance.····················· 115

7.4 Measured single-ended NFs at Port 2 and Port 3 (NF_{21}, NF_{31}).················ 117

7.5 Measured and simulated matching responses at: (a) RF input (Port1), (b) IF output (Ports 2 and 3), and (c) LO input (Port 4). ························ 118

7.6 Measured single-ended conversion gain for Ports 1 to 2 and 1 to 3 (S_{21}, S_{31}) as a function of LO power at: (a) Rx mode 1, (b) Rx mode 2, (c) Rx mode 3, and (4) Rx mode 4. ··· 120

7.7 Measured single-ended input P_{1dB} for Ports 1 to 2 and 1 to 3 (S_{21}, S_{31}) as a function of RF power at: (a) Rx mode 1, (b) Rx mode 2, (c) Rx mode 3, and (4) Rx mode 4. ··· 121

7.8 Measured single-ended input IP_3: $IIP_{3,21}$ at Port 2 (a), (c), (e), (g) and $IIP_{3,31}$ at Port 3 (b), (d), (f), (h) for Rx modes 1 to 4, respectively.············ 122

LIST OF TABLES

TABLE Page

2.1 Component Values of Conventional Tri-band Loads 19

2.2 Component Values of Modified Tri-band Load 24

2.3 Component Values for Various Modified Tri-band Loads 24

3.1 Performance Summary of the Developed Concurrent Tri-band LNA and Existing Concurrent Multiband LNAs 46

4.1 Component Values of Concurrent Dual-band LNAs 58

4.2 Simulated Performance Summary of dual-band LNAs With and Without Feedback 63

4.3 Performance Summary and Comparison of Concurrent Multiband LNAs 72

5.1 Component Values of Concurrent Dual-band Single-to-Differential LNA 82

5.2 Performance Summary of Single-to-Differential Baluns and LNAs 93

6.1 Measured Performance of the Concurrent Dual-band Merged LNA and Mixer 108

6.2 Performance Summary and Comparison of Dual-band Mixers 108

7.1 Operation Modes Summary of the Proposed Concurrent Dual-band Receiver Front-end 113

7.2 Performance Summary of Concurrent Dual-band Receiver Front-end 119

7.3 Port-to-Port Isolation of Concurrent Dual-band Receiver Front-end 123

7.4 Performance Comparison of Dual-band Receivers 124

CHAPTER I

INTRODUCTION

1.1 Review of Multiband Receiver Architectures and Multiband LNAs

Demands for multi-standard multiband receivers have rapidly increased over the past decade as modern wireless communication systems and applications requiring multiband operations have evolved, particularly those intended for single-chip implementations. Implementation of several different applications and/or standards at various frequency bands into a single chip requires better receiver architectures and system integration, which ultimately improves the performance and drives down the power consumption, size and cost to satisfy stringent system specifications and competitive market requirements.

The integration complexity, power consumption, size, and cost of multiband receiver primarily depend on the receiver architectures as shown in Fig. 1.1. Multiple receiver front-ends composed of antennas, low-noise amplifiers (LNAs), and mixers for individual frequency bands can be integrated in parallel as shown in Fig. 1.1(a). This configuration is complex to integrate and consumes large area and power [1], [2]. By using a band-select switch preceding a wideband or multiband mixer, multiband receiver front-ends can be simplified as shown in Fig. 1.1(b) [3]. A wideband or multiband reconfigurable LNA can be used after a band-select switch to replace multiple LNAs as shown in Fig. 1.1(c), which further simplifies and reduces the size and power consumption for multiband receiver front-ends [4]. The aforementioned receiver

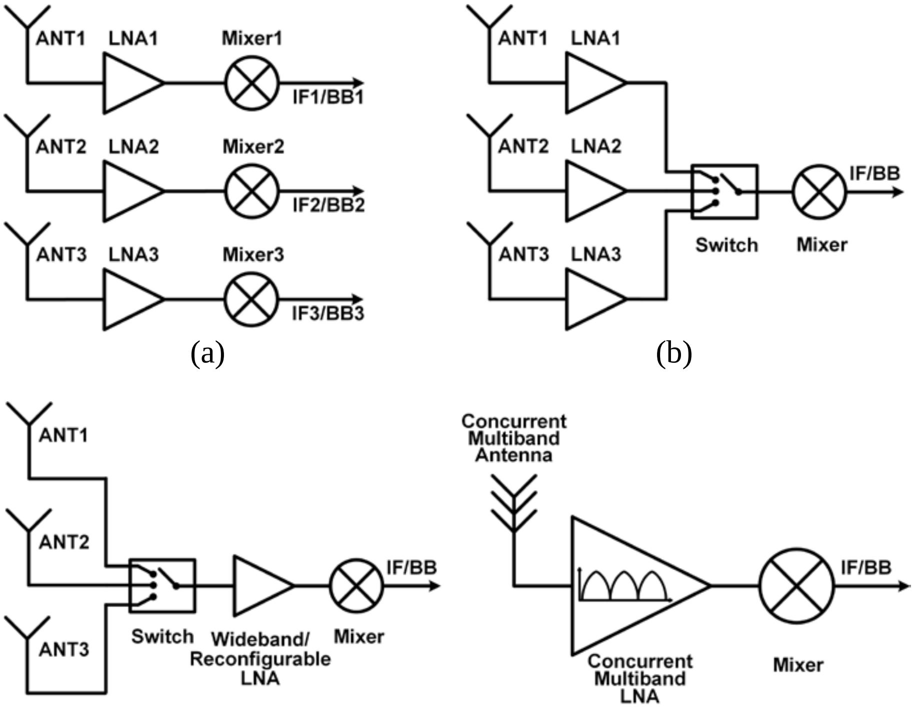

(a) (b)

(c) (d)

Fig. 1.1 Simplified multiband receiver front-end configurations with (a) separate parallel receiver front-ends (with separate antennas), (b) separate antennas and LNAs, (c) separate antennas and wideband or reconfigurable LNA, and (d) single concurrent multiband antenna and LNA.

architectures in Fig. 1.1(b) and (c), however, receive and process only one frequency band at a time due to their switching functionality and hence are not concurrently operated.

Concurrent multiband receivers receive and process multiple frequency bands simultaneously [5]. They are thus capable of providing multitask or multifunction to meet consumer needs in modern wireless communications. Concurrent multiband receivers require at least some of their components to operate concurrently at different frequency bands which results in substantial reduction of size, cost and power dissipation. Fig. 1.1(d) shows a simplified concurrent multiband receiver, typically consisting of an off-chip antenna, and on-chip LNA and mixer. While the mixer can be designed as a multiband or wideband component with more degrees of freedom in terms of matching and noise figure performances, the LNA should perform as a concurrent multiband device and hence requires proper input matching to the antenna, low noise figure (NF), high gain, and high linearity at multiple individual bands to handle multiple input signals simultaneously. Therefore, the design of concurrent multiband LNAs is the most critical issue for the implementation of fully integrated low-cost and low-power concurrent multi-band receivers.

Research and development of concurrent multiband LNAs have gained significant interests in recent years. The design of on-chip concurrent multiband LNAs is quite challenging due to their stringent requirements over multiband as mentioned above. Several concurrent dual-band LNAs operating below 6 GHz [5]–[9] and 6-to-24 GHz [10]–[12] have been developed. However, concurrent tri-band LNAs have been rarely implemented. Particularly, there has been only one concurrent tri-band LNA reported to date in 0.945/2.4/5.25-GHz bands [13]. The tri-band LNAs in [14] and [15] were not fabricated and only simulation performances were reported for wireless communication applications below 6 GHz, such as GSM and Wi-Fi. Moreover, no concurrent tri-band LNA working at higher frequencies up to millimeter-wave regime has been reported. As the need for receivers working concurrently over more than two bands and the demand for higher operating frequencies increase, the development of dual-band and tri-band LNAs in high microwave (> 20 GHz) and millimeter-wave becomes necessary, particularly at 28/38 GHz for 5G wireless communications, 24/60 GHz ISM applications, 24/77 GHz automotive radar sensors, etc.

One of the main challenges in the design of concurrent multiband LNAs is the creation of multiple pass-bands with good gain and gain balance, and multiple stop-bands in between with adequate rejection. The first reported concurrent dual-band LNA in [5] was designed at 2.45/5.25 GHz using off-chip capacitor and inductors having high quality (Q) factor at the LNA input and achieved a good stop-band rejection ratio of around 40 dB and a gain imbalance of 1.5 dB between the two peak gain frequencies. Thereafter, concurrent dual-band LNAs in [6]–[10] and tri-band LNAs in [14] and [15] have used integrated passive notch filters consisting of several inductors and capacitors to realize the required stop-band rejections. Multiband LNAs using integrated passive notch filters, however, suffer from poor stop-band rejection performance, due to the fact that stop-band rejection with integrated passive components depends mainly on the low Q-factor of the integrated inductors. Using high-Q inductors can enhance the stop-band rejection, yet leading to large integration area in addition to difficulty in the design of high-Q inductors.

Alternative methods for higher stop-band performance in concurrent multiband amplifiers were presented in [11]–[13]. The concurrent dual-band amplifier in [11] implemented synthetic transmission lines to build the dual-frequency matching circuits. Even though this dual-band amplifier shows good stop-band rejection ratio (SRR) of more than 40 dB, it occupies a large area and exhibits 13-dB gain degradation at higher pass-band, thus providing poor NF performance. The dual-band tunable concurrent amplifier in [12] separates the output path of the amplifier into two independent paths for low-band and high-band operations, but it requires an additional off-chip LNA. The concurrent tri-band LNA in [13] uses two active notch filters that provides a negative resistance to overcome the low Q-factor of integrated inductors. Furthermore, the additional active devices used in [12] and [13] lead to higher power consumption consequently.

1.2 Proposed Concurrent Dual-band Receiver and Multiband LNAs

The proposed double-conversion concurrent dual-band receiver architecture is shown in Fig. 1.2. The first down-conversion for the received signals at high microwave and millimeter-wave input frequencies (24.5/36.5 GHz) is performed via the LNA and RF mixer with a 21-GHz local oscillator (LO) signal (LO1). The IF signals (3.5/15.5 GHz) are filtered and amplified by the IF filter and the IF amplifier, respectively. Then, the second down-conversion is carried out via the IF mixer with the 3.5/15.5-GHz dual-band LO signals (LO2). The baseband (BB) low-pass filter (LPF) removes the out-of-

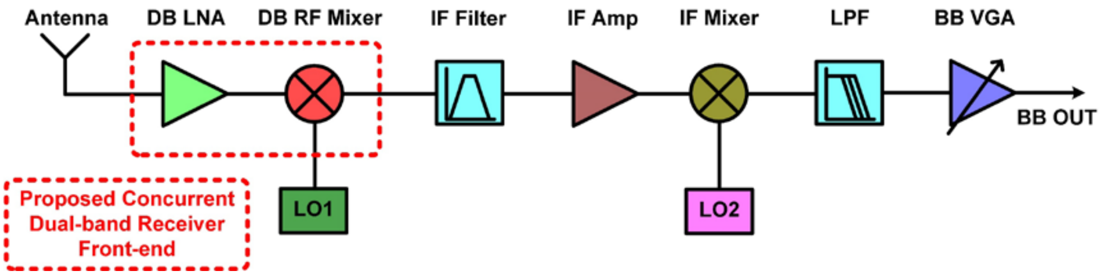

Fig. 1.2 Proposed concurrent dual-band receiver front-end as part of a double-conversion receiver.

band high frequency spurious signals and the variable gain amplifier (VGA) amplifies only the desired in-band signals. The IF filter, amplifier, and mixer as well as the BB LPF and VGA can be easily designed with either wideband or concurrent multiband configurations due to their lower operating frequencies and less design difficulties as compared to the RF front-end building blocks. Therefore, the development of multiband RF receiver front-end building blocks for Ku-/K-/Ka-band radar sensing applications, such as multiband (dual- and tri-band) LNAs, single-to-differential amplifiers and RF mixer, becomes more important.

In this dissertation, a new concurrent tri-band LNA implementing a novel feedback tri-band load composed of two feedback notch filters is presented first in Ch. II. The proposed feedback tri-band load overcomes the low Q-factor of integrated inductors, and hence provides superior stopband rejection performance. In addition, comparative analysis and design principles of the conventional tri-band load and the proposed modified and feedback tri-band loads, and their use in tri-band LNA design are also presented for the first time. The developed 13.5/24/35-GHz concurrent tri-band LNA in Ch. III provides stable and high SRRs of more than 30 dB without additional area and power consumption.

Two K-/Ka-band concurrent dual-band LNAs employing two different types of feedback dual-band loads are proposed in Ch. IV by significantly expanding the feedback notch technique used in the concurrent tri-band LNA. The concurrent dual-band LNAs use novel single-input to single-output (single-to-single) inductor and transformer feedback dual-band loads, respectively. Moreover, these dual-band LNAs also provide a unique characteristic to control the stopband rejection ratio by adjusting the bias level of second-stage amplifier. The analyses and designs of the conventional and proposed feedback dual-band loads are first introduced to provide the insight and signify the advantages of the feedback loads. Then, a 21.5/36.5-GHz concurrent dual-band LNA with an inductor feedback dual-band load and another 23/36-GHz concurrent dual-band LNA with a new transformer feedback dual-band load are presented. The latter provides more degrees of freedom for the creation of the stopband and passbands as compared to the former. Both the developed concurrent dual-band LNAs achieve the best NF and gain-balance performances among the concurrent multiband LNAs reported at high microwave and millimeter-wave frequencies.

In Ch. V, a new concurrent dual-band single-to-differential transformer feedback dual-band load as well as its use in the concurrent dual-band single-to-differential LNA are presented. The designed concurrent dual-band single-to-differential LNA converts two simultaneous independent single-ended input signals at around 22 and 36 GHz into 180° out-of-phase differential signals at its output without any switching activity by employing the proposed transformer feedback dual-band load. The developed concurrent dual-band single-to-differential LNA exhibits excellent gain, gain/phase balances, and NF performances as well as a great stopband rejection, validating the unique advantages of the proposed single-to-differential transformer feedback concurrent dual-band LNA. The developed LNA is the first true concurrent dual-band single-to-differential amplifier operating up to millimeter-wave frequencies and without using switching mechanism.

A concurrent dual-band merged single-to-differential LNA and RF-to-IF down-conversion mixer implementing the proposed single-to-differential transformer feedback dual-band load is presented in Ch. VI. The single-to-differential transformer feedback dual-band load is used as a concurrent dual-band transconductance (g_m) amplifier, which simultaneously converts two independent single-ended RF voltage signals at around 24.5 and 36.5 GHz into the 180° out-of-phase differential current signals flowing into the Gilbert-cell mixer switching core. With a 21-GHz single-ended LO signal, the down-converted dual IF bands are located at 3.5/15.5 GHz for two passband signals at 24.5/36.5 GHz, respectively. By varying the bias voltage of the second-stage's tail current source, the concurrent dual-band merged LNA and mixer can also control both the passband gains and SRR at the same time, and it shows the substantial improvement of stopband rejection performance and validates the effectiveness and unique operation characteristics of the proposed transformer feedback dual-band load and its use in the down-conversion mixer. The developed merged LNA and mixer is the first fully integrated concurrent dual-band mixer operating up to millimeter-wave frequencies without using any switching mechanism.

In Ch. VII, a new concurrent dual-band receiver front-end is proposed. It consists of the concurrent dual-band LNA using the single-to-single transformer feedback dual-band load presented in Ch. IV and the concurrent dual-band merged LNA and mixer employing the single-to-differential transformer feedback dual-band load presented in Ch. VI. The receiver front-end operates with RF passband frequencies at 24.5/36.5 GHz, LO frequency at 21 GHz, and IF frequencies at 3.5/15.5 GHz, accordingly. Since both of the dual-band LNA and the dual-band merged LNA and mixer have the functionality of controlling the stopband rejection and the passband gain balance by adjusting the bias level of second-stage inverting amplifier, the proposed receiver front-end has versatile operation modes by combining each operation mode of the dual-band LNA and the merged LNA and mixer. The developed concurrent dual-band receiver front-end achieves the highest gain and the best NF performances as well as the largest SRRs, while operating at highest frequencies up to millimeter-wave region, among the concurrent dual-band receivers reported to date.

Finally, the conclusions and summary of the works are provided in Ch. VIII.

CHAPTER II

ANALYSIS AND DESIGN OF CONCURRENT MULTIBAND LOADS[*]

This chapter presents the analyses and designs of three different tri-band loads: the conventional, modified and feedback tri-band loads. Although the proposed tri-band LNA only employs the feedback tri-band load, the analyses and designs of the other two loads are needed for the design of the feedback tri-band load.

2.1 Conventional Dual-band Load

Fig. 2.1(a) shows the concurrent dual-band LNA in [5], which uses conventional dual-band resonators: one at the input (dual-band input matching network) and another at the output (dual-band load resonator). In the dual-band input matching network, off-chip high-Q inductor (L_{g1}), bonding wire (L_{g2}), and capacitor (C_{g1}) are used to obtain simultaneous input matching and minimum NF at both desired frequencies. For the dual-band output load network, a wideband load with parallel L_1–C_1 tank and a notch filter composed of series L_2–C_2 are integrated in parallel. The load impedance (Z_{DB}) looking into the dual-band load can be derived as

$$Z_{DB}(s) = \frac{sL_1(1+s^2L_2C_2)}{s^4L_1L_2C_1C_2 + s^2(L_1C_1 + L_2C_2 + L_1C_2) + 1}. \tag{2.1}$$

---

[*] © 2013 IEEE. Reprinted, with permission, from J. Lee and C. Nguyen, "A 13/24/35-GHz Concurrent Tri-band LNA with Feedback Notches," in *IEEE Topical Meetings on Silicon Monolithic Integrated Circuits in RF Systems (SiRF) Dig.*, Jan. 2013, pp. 252–254. and J. Lee and C. Nguyen, "A Concurrent Tri-Band Low-Noise Amplifier With a Novel Tri-Band Load Resonator Employing Feedback Notches," *IEEE Transaction on Microwave Theory and Techniques*, vol. 61, no.12, pp. 4195–4208, Dec. 2013.

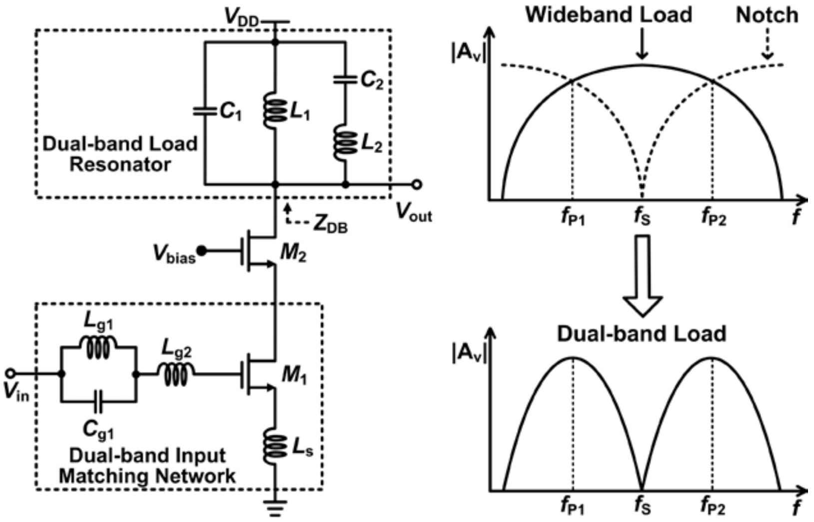

(a) (b)

Fig. 2.1 (a) Concurrent dual-band CMOS LNA reported in [5]. (b) Responses of wideband load, notch filter, and dual-band load constructed from the combined wideband load and notch filter.

Since the series L_2–C_2 notch introduces a zero at the frequency of $1/2\pi\sqrt{L_2C_2}$ over the wideband gain response of the parallel L_1–C_1 tank, the concurrent dual-band gain response can be obtained as illustrated in Fig. 2.1(b).

2.2 Conventional Tri-band Load

By expanding the construction concept of the conventional dual-band load in [5], a simple conventional tri-band load can be created as shown in Fig. 2.2(a). The parallel L_1–C_1 tank forms a wideband load covering the three bands of interest. Two notches formed by the series L_2–C_2 and L_3–C_3 pairs, representing the low- and high-band notches, respectively, are connected in parallel to the wideband load to establish two stop-bands, hence creating the dual-band notch filter. Fig. 2.2(c) shows the insertion loss responses (S_{21}) of these networks. By combining these responses together, a clear tri-band response for the conventional tri-band load can be achieved as shown in Fig. 2.2(c).

2.2.1 Analysis of Conventional Tri-band Load

As illustrated in Fig. 2.2(c), the second pass-band, f_{P2}, occurs at the crossing of the S_{21} of the parallel low- and high-band notches. The two notch frequencies determine the low stop-band (f_{S1}) and the high stop-band (f_{S2}) frequencies of the conventional tri-

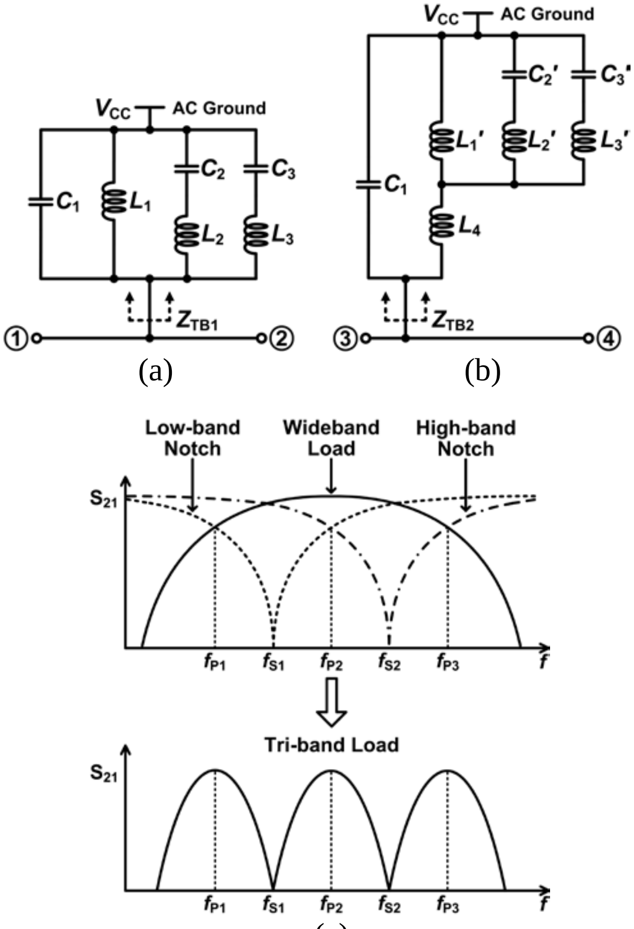

(a) (b)

(c)

Fig. 2.2 Tri-band load: (a) conventional, (b) modified, and (c) conceptual construction of tri-band load using a wideband load and two notch filters.

band load as shown in Fig. 2.2(c), respectively. As the wideband load covers the entire tri-band, its S_{21} would overlap that of the dual-band notch filter. This, together with the fact that its response is independent of the two notches, enables the first and third pass-band centered at f_{P1} and f_{P3}, respectively, to be placed where the dual-band notch filter and the wideband load responses cross each other as shown in Fig. 2.2(c). That is, f_{P1} and f_{P3} are determined by the pre-assigned f_{P2}, f_{S1}, f_{S2}, and wideband load response.

We now introduce new inductor L_{WB} and capacitor C_{WB} according to $L_1 = kL_{WB}$ and $C_1 = C_{WB}/k$, where k is a constant. Fig. 2.3 shows the insertion losses (S_{21}) of the dual-band notch filter, wideband load, and conventional tri-band load. By changing k, which satisfies $L_1 \cdot C_1 = kL_{WB} \cdot (C_{WB}/k)$, the first and third pass-band can be tuned as shown in Fig. 2.3(b). As L_1 is reduced and C_1 is increased, corresponding to decreasing k, f_{P1} and f_{P3} approach f_{P2}, causing sharp roll-off skirt characteristics at the upper and lower band-edge of the first and third pass-band, respectively, as seen in Fig. 2.3(b). In order to produce a symmetrical response for the tri-band load, we can choose the two notch frequencies as $f_{S1} = \sqrt{f_{P1} f_{P2}}$ and $f_{S2} = \sqrt{f_{P2} f_{P3}}$, satisfying the geometric centers of the three pass-bands. Accordingly, the first and third pass-band can be located at $f_{P1} = f_{S1}^2 / f_{P2}$ and $f_{P3} = f_{S2}^2 / f_{P2}$, respectively.

The impedance Z_{DBN} of the dual-band notch filter can be derived as

$$\begin{aligned}
&Z_{\mathrm{DBN}}(s) = \frac{N_{\mathrm{DBN}}(s)}{D_{\mathrm{DBN}}(s)} \\
&N_{\mathrm{DBN}}(s) = (1 + s^2 L_2 C_2)(1 + s^2 L_3 C_3) \\
&D_{\mathrm{DBN}}(s) = s\left[s^2 (L_2 + L_3) C_2 C_3 + (C_2 + C_3) \right].
\end{aligned} \tag{2.2}$$

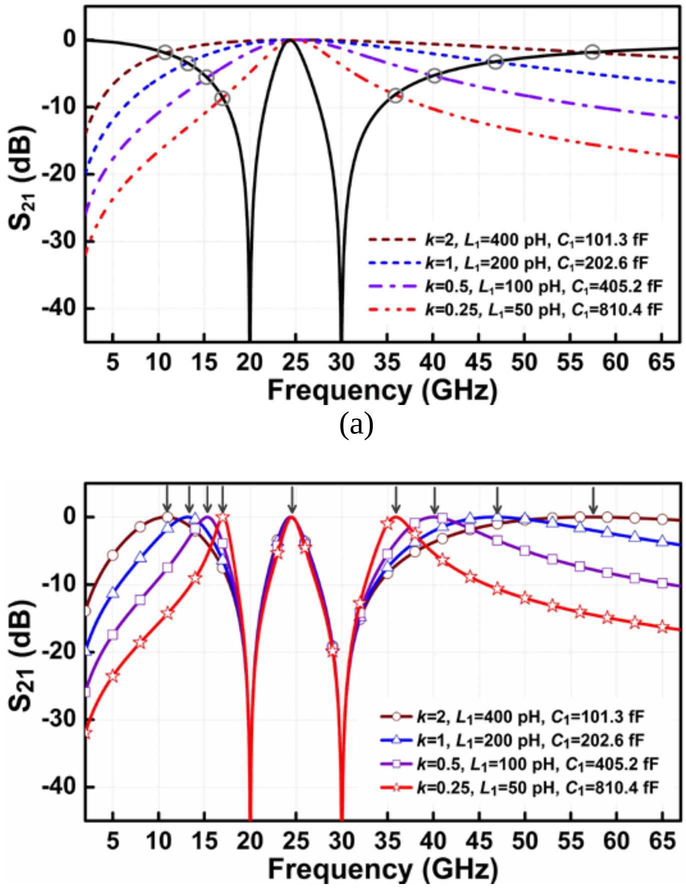

(a)

(b)

Fig. 2.3 Insertion loss for (a) the dual-band notch filter and wideband load for different *k*, L_1 and C_1, and (b) the conventional tri-band load for different *k*, L_1 and C_1. The top arrows denote the pass-bands of the tri-band load.

The numerator N_{DBN} in (2.2) defines the two zeros corresponding to the stop-band frequencies of the low and high stop-bands, respectively, as

$$\omega_{S1} = \frac{1}{\sqrt{L_2 C_2}}, \quad \omega_{S2} = \frac{1}{\sqrt{L_3 C_3}} \tag{2.3}$$

By letting the denominator D_{DBN} in (2.2) equal to zero, the pass-band frequency of the dual-band notch filter can be obtained as

$$\omega_{P2} = \sqrt{\frac{C_2 + C_3}{C_2 C_3 (L_2 + L_3)}}. \tag{2.4}$$

The impedance of the wideband load (L_1–C_1) is given by

$$Z_{WB}(s) = \frac{sL_1}{s^2 L_1 C_1 + 1}. \tag{2.5}$$

From (2.5), the resonant frequency of the wideband load, which defines its primary pass-band frequency, can be found as

$$\omega_{P,WB} = \frac{1}{\sqrt{L_1 C_1}} = \frac{1}{\sqrt{kL_{WB} \cdot \frac{C_{WB}}{k}}}. \tag{2.6}$$

The second pass-band frequency f_{P2} of the tri-band load is governed by either (2.4) or (2.6). However, since the pass-band dictated by the dual-band notch filter is more defined than that of the wideband load, particularly when k is large, as seen in Fig. 2.3(a), f_{P2} is mainly dominated by the location of ω_{P2} in (2.4). Therefore, L_2, C_2 and L_3, C_3 should be determined from (2.4) in conjunction with (2.3) from the specified f_{P2}, f_{S1} and f_{S2}.

Letting $L_1 = L_2 + L_3$ and $2C_1 = C_2 = C_3$ leads to $\omega_{P2} = \omega_{P,WB}$ which results in, upon using (2.4) and (2.6):

$$\frac{1}{L_1 C_1} = \frac{1}{(L_2 + L_3)\left(\frac{C_2 C_3}{C_2 + C_3}\right)}. \tag{2.7}$$

Equation (2.7) represents the condition under which a single f_{P2} exists and can be considered as the criterion for the optimal second pass-band frequency of the conventional tri-band load.

It is noted that since the L_1–C_1 tank is used mainly to control the skirt roll-off characteristics at the lower and upper band-edge of the first and third pass-band of the conventional tri-band load, respectively, as seen in Fig. 2.3(b), desired skirt roll-off characteristics should also be considered in the determination of L_1 and C_1.

The impedance of the conventional tri-band load in Fig. 2.2(a) can be derived as

$$\begin{aligned}
Z_{\mathrm{TB1}}(s) &= \frac{N_{\mathrm{TB1}}(s)}{D_{\mathrm{TB1}}(s)} \\
N_{\mathrm{TB1}}(s) &= sL_1(1+s^2L_2C_2)(1+s^2L_3C_3) \\
D_{\mathrm{TB1}}(s) &= s^6L_1L_2L_3C_1C_2C_3 \\
&\quad + s^4\begin{bmatrix} L_1L_2C_1C_2+(L_1L_2+L_2L_3+L_1L_3)C_2C_3 \\ +L_1L_3C_1C_3 \end{bmatrix} \\
&\quad + s^2\left[L_1C_1+(L_1+L_2)C_2+(L_1+L_3)C_3\right]+1.
\end{aligned} \tag{2.8}$$

The numerator N_{TB1} clearly shows that the conventional tri-band load indeed has the same stop-band zeros as the dual-band notch filter seen in (2.3). The denominator D_{TB1} can be recast as

$$\begin{aligned}
D_{\mathrm{TB1}}(s) &= (s^2L_1C_1+1)(s^2L_2C_2+1)(s^2L_3C_3+1) \\
&\quad + s^2L_1\left[s^2(L_2+L_3)C_2C_3+(C_2+C_3)\right].
\end{aligned} \tag{2.9}$$

By letting the second term of (2.9) equal to zero, it is found that a pass-band frequency of the conventional tri-band load occurs at the same location of that given in (2.4) for the dual-band notch filter. This thus confirms that the second pass-band of the conventional tri-band load indeed originates from the pass-band of the dual-band notch filter as discussed earlier.

Equating D_{TB1} in (2.8) to zero leads to

$$\begin{aligned}&\omega^6 L_1L_2L_3C_1C_2C_3\\&-\omega^4\begin{bmatrix}L_1L_2C_1C_2+(L_1L_2+L_2L_3+L_1L_3)C_2C_3\\+L_1L_3C_1C_3\end{bmatrix}\\&+\omega^2\left[L_1C_1+(L_1+L_2)C_2+(L_1+L_3)C_3\right]-1=0.\end{aligned}\tag{2.10}$$

The three poles representing the first, second, and third pass-band frequencies, ω_{P1}, ω_{P2}, and ω_{P3}, respectively, satisfy the following equations upon applying the factor theorem on (2.10):

$$\begin{aligned}&\omega_{P1}^2\omega_{P2}^2\omega_{P3}^2=\frac{1}{L_1L_2L_3C_1C_2C_3}\\&\frac{1}{\omega_{P1}^2}+\frac{1}{\omega_{P2}^2}+\frac{1}{\omega_{P3}^2}=L_1C_1+(L_1+L_2)C_2+(L_1+L_3)C_3.\end{aligned}\tag{2.11}$$

Equations (2.11) can be used to determine L_1 and C_1 together with L_2, C_2, and L_3, C_3, obtained from (2.3) and (2.4) as mentioned earlier, and desired f_{P1}, f_{P2}, and f_{P3}.

2.2.2 Design Example of Conventional Tri-band Load

As a design example showing a design procedure for the conventional tri-band load using the foregoing analysis, we consider f_{P1} and f_{P3} at around 15 and 35 GHz. We also select f_{S1} and f_{S2} as 20 and 30 GHz, respectively, from which f_{P2} can be estimated as around 25 GHz. The design is summarized as follows.

First, we calculate L_2 and L_3 from (2.3) by assuming initial C_2 and C_3 as 200 fF for the specified f_{S1} and f_{S2}. The following shows four possible combinations of L_2, C_2, and L_3, C_3, and corresponding f_{P2} calculated from (2.4):

(a) C_2 = 200 fF, L_2 = 316.6 pH, C_3 = 200 fF, L_3 = 140.7 pH, f_{P2} = 23.54 GHz

(b) C_2 = 200 fF, L_2 = 316.6 pH, C_3 = 140.7 fF, L_3 = 200 pH, f_{P2} = 24.37 GHz

(c) C_2 = 316.6 fF, L_2 = 200 pH, C_3 = 200 fF, L_3 = 140.7 pH, f_{P2} = 24.63 GHz

(d) C_2 = 316.6 fF, L_2 = 200 pH, C_3 = 140.7 fF, L_3 = 200 pH, f_{P2} = 25.49 GHz

Each combination of L_2, C_2, and L_3, C_3 produces slightly different f_{P2} and skirt characteristics of the stop-bands. Option (b) is selected as it exhibits the highest stop-band Q-factor as described later, as well as the most symmetric skirt characteristics at both stop-bands. L_1 can be determined as 84.7 pH by substituting the product L_1C_1 in (2.11). Substituting the obtained L_1 into (2.6) then gives C_1 = 498.2 fF.

Although (2.6) and (2.11) can provide valid values for L_1 and C_1, they do not provide insight of the skirt roll-off characteristics of the tri-band load mentioned in Section 2.2.1. To overcome this drawback, the final values for L_1 and C_1 can be selected making use of a graphical analysis based on Fig. 2.3. This procedure begins by choosing an initial value for k and L_1. Herein, we choose k = 1 and L_1 = 200 pH to make the tri-band load impedance sufficiently high to achieve high LNA gain, as will be described shortly. C_1 is then calculated from (2.6) and the response of the tri-band load is plotted as shown in Fig. 2.3(b), from which f_{P1}, f_{P2}, and f_{P3} can be identified. The process is repeated for different k values. Table 2.1 summarizes the results including the Q-factor of the dual-band notch filter at the two stop-bands. The stop-band Q-factor is defined as

$$\mathrm{Q}_{S1,2} = \frac{\omega_{S1,2}}{\Delta\omega_P}, \tag{2.12}$$

where $\omega_{S1,2}$ is the stop-band notch frequencies in (2.3) and $\Delta\omega_P$ is the 3-dB bandwidth measured from the pass-band frequency in (2.4). An optimum value for k is chosen such that it produces f_{P1}, f_{P2}, and f_{P3} as close to the specified frequencies as possible. This k can be found between 0.25 and 0.5 according to Table 2.1. It can also be inferred from

TABLE 2.1

COMPONENT VALUES OF CONVENTIONAL TRI-BAND LOADS

	k=0.25	k=0.5	k=1	k=2	Unit
L_1	50	100	200	400	pH
C_1	810.4	405.2	202.6	101.3	fF
f_{P1}	17.0	15.3	13.2	10.8	GHz
f_{P2}	24.5	24.5	24.4	24.4	GHz
f_{P3}	35.9	40.0	46.6	57.1	GHz
Q_{S1}	3.48	3.07	2.68	2.39	-
Q_{S2}	3.47	2.82	2.31	1.93	-

Table 2.1 that such an optimum k would also correspond to L_1 and C_1 values close to the calculated values obtained earlier.

As L_1 and C_1 are reduced and increased, respectively, corresponding to decreasing k, as seen in Table 2.1, f_{P1} and f_{P3} approach f_{P2}, causing sharp roll-off skirt characteristics at the upper and lower band-edge of the first and third pass-band, respectively, as can be deduced from Fig. 2.3(b) mentioned earlier. In practice, C_1 is directly connected to the output node of an LNA and includes all parasitic capacitances at the tri-band load, hence the larger C_1, the lower LNA gain at high frequencies. Therefore, C_1 should be as small as possible to increase the LNA gain at high frequencies, especially in the mm-wave frequency regime. This, in fact, leads to the limitation of the conventional tri-band load in obtaining both sharp roll-off skirt characteristic and high LNA gain at the same time. In addition, the bandwidths of the two pass-bands at f_{P1} and f_{P3} become narrower as L_1 is reduced and C_1 is increased, which are undesirable for many mm-wave applications, such as high-data-rate transmission. The modified tri-band load to be presented below would overcome these problems of the conventional tri-band load.

2.3 Proposed Modified Tri-band Load

By separating L_1 in Fig. 2.1(a) into two parts, L_1' and L_4, and connecting the two notches to the node between L_1' and L_4, a new modified tri-band load can be generated as shown in Fig. 2.1(b). The impedance Z_{TB2} of the modified tri-band load can be derived as

$$\begin{aligned}
Z_{\mathrm{TB2}}(s) &= \frac{N_{\mathrm{TB2}}(s)}{D_{\mathrm{TB2}}(s)} \\
N_{\mathrm{TB2}}(s) &= sL_S\left[1+s^2\left(L_2'+L_P\right)C_2'\right]\left[1+s^2\left(L_3'+L_P\right)C_3'\right] \\
D_{\mathrm{TB2}}(s) &= s^6 L_S\left(L_2'L_3'+L_2'L_P+L_3'L_P\right)C_1C_2'C_3' \\
&\quad + s^4\begin{bmatrix} L_S\left(L_2'+L_P\right)C_1C_2' \\ +(L_1'L_2'+L_2'L_3'+L_1'L_3')C_2'C_3' \\ +L_S\left(L_3'+L_P\right)C_1C_3' \end{bmatrix} \\
&\quad + s^2\left[L_SC_1+(L_1'+L_2')C_2'+(L_1'+L_3')C_3'\right]+1,
\end{aligned} \tag{2.13}$$

where $L_S = L_1'+L_4$ and $L_P = L_1'L_4/(L_1'+L_4)$ are the equivalent series and parallel inductances of L_1' and L_4, respectively. The modified tri-band load reduces to the conventional tri-band load when $L_4 = 0$ as expected. As can be seen from (2.13), the modified tri-band load provides an additional degree of freedom to choose the stop-band and pass-band frequencies through L_S and L_P as compared to the conventional tri-band load using a single load inductor. Since L_S and L_P are composed of L_1' and L_4, the stop-band and pass-band frequencies of the modified tri-band load are effectively controlled by L_1' and L_4, in general, or the ratio of L_1' and L_4 in particular. The following analysis discusses the selection of proper values for L_1', L_4, and their ratio.

2.3.1 Analysis of Proposed Modified Tri-band Load

From the numerator of (2.13), the stop-band notch frequencies of the modified tri-band load, f_{S1} and f_{S2}, can be found as

$$f_{S1} = \frac{1}{2\pi\sqrt{\left(L_2' + \frac{L_1'L_4}{L_1' + L_4}\right)C_2'}} = \frac{1}{2\pi\sqrt{L_{N1}C_2'}} \tag{2.14}$$

$$f_{S2} = \frac{1}{2\pi\sqrt{\left(L_3' + \frac{L_1'L_4}{L_1' + L_4}\right)C_3'}} = \frac{1}{2\pi\sqrt{L_{N2}C_3'}} \tag{2.15}$$

where $L_{N1} = L_2'+L_P$ and $L_{N2} = L_3'+L_P$ represent the effective notch inductances at f_{S1} and f_{S2}, respectively. When $L_4 = 0$ (or $L_1' = 0$), f_{S1} and f_{S2} become $1\Big/2\pi\sqrt{L_2'C_2'}$ and $1\Big/2\pi\sqrt{L_3'C_3'}$, respectively, which are the same as those for the conventional tri-band load, as expected.

On the other hand, since L_S and L_P in the denominator of (2.13) can also affect the pass-band locations, the inductance values of L_1' and L_4 should be chosen to produce the desired pass-band and stop-band frequencies at the same time. To facilitate the finding of the pass-band locations, the denominator D_{TB2} in (2.13) is rewritten as

$$\begin{aligned} D_{\mathrm{TB2}}(j\omega) = {} & \omega^6 L_S \left(L_2' L_3' + L_2' L_P + L_3' L_P\right) C_1 C_2' C_3' \\ & - \omega^4 \begin{bmatrix} L_S \left(L_2' + L_P\right) C_1 C_2' \\ +(L_1' L_2' + L_2' L_3' + L_1' L_3') C_2' C_3' \\ +L_S \left(L_3' + L_P\right) C_1 C_3' \end{bmatrix} \\ & + \omega^2 \left[L_S C_1 + (L_1' + L_2') C_2' + (L_1' + L_3') C_3' \right] - 1 \\ & = 0. \end{aligned} \tag{2.16}$$

The three poles, ω_{P1}, ω_{P2}, and ω_{P3}, corresponding to the pass-bands of the modified tri-band load, satisfy the following conditions obtained from (2.16) via the factor theorem:

$$\omega_{P1}^2 \omega_{P2}^2 \omega_{P3}^2 = \frac{1}{(L_S L_2' L_3' + L_S L_P L_2' + L_S L_P L_3') C_1 C_2' C_3'} \tag{2.17}$$

$$\begin{aligned} & \omega_{P1}^2 + \omega_{P2}^2 + \omega_{P3}^2 \\ & = \frac{1}{\left(L_4 + L_{E1}\right) C_1} + \frac{1}{\left(L_2' + L_{E3}\right) C_2'} + \frac{1}{\left(L_3' + L_{E2}\right) C_3'} \end{aligned} \tag{2.18}$$

$$\frac{1}{\omega_{P1}^2} + \frac{1}{\omega_{P2}^2} + \frac{1}{\omega_{P3}^2} = L_S C_1 + (L_1' + L_2') C_2' + (L_1' + L_3') C_3', \tag{2.19}$$

where, in (2.18), $L_{\mathrm{E1}} = L_1' \| L_2' \| L_3'$, $L_{\mathrm{E2}} = L_2' \| L_1' \| L_4$, and $L_{\mathrm{E3}} = L_3' \| L_1' \| L_4$. Following a method similar to that used for the design of the conventional tri-band load, we can find the component values of the modified tri-band load through (2.14), (2.15), and (2.17)–(2.19).

Similar to the case of the conventional tri-band load, we introduce a parameter k' to the inductors L_1' and L_4 shown in Fig. 2.1(b), which will help facilitate the design using a graphical analysis. By defining $L_1' = k' L_{\mathrm{S}}$ and $L_4 = (1-k') L_{\mathrm{S}}$, the equivalent parallel inductance L_{P} can be rewritten as $L_{\mathrm{P}} = L_1' \| L_4 = k'(1-k') L_{\mathrm{S}}$. Substituting L_{P} into (2.14) and (2.15) leads to the new expression for the stop-band frequencies as

$$f_{S1} = \frac{1}{2\pi\sqrt{[L_2' + k'(1-k')L_S]C_2'}} \tag{2.20}$$

$$f_{S2} = \frac{1}{2\pi\sqrt{[L_3' + k'(1-k')L_S]C_3'}}. \tag{2.21}$$

where $0 < k' \leq 1$. Note that $k'=0$ and $k'=1$ result in the wideband and conventional tri-band loads, respectively. The effective notch inductances L_{N1} and L_{N2} can be derived as

$$L_{N1} = L_2' + L_P = L_2' + k'(1-k')L_S \tag{2.22}$$

$$L_{N2} = L_3' + L_P = L_3' + k'(1-k')L_S \tag{2.23}$$

From (2.22) and (2.23), the two notch inductors L_2' and L_3' of the modified tri-band load can be found as

$$L_2' = L_{N1} - k'(1-k')L_S \tag{2.24}$$

$$L_3' = L_{N2} - k'(1-k')L_S. \tag{2.25}$$

2.3.2 Design Example of Proposed Modified Tri-band Load

As an example, we design a modified tri-band load based on the conventional tri-band load with $k = 1$ described in Table 2.1. For the conventional tri-band load, the wideband load inductor L_1 was chosen as 200 pH in order to provide a high LNA gain for the three pass-bands as discussed in the previous section. Therefore, equivalently, we maintain the same load inductor of L_S = 200 pH, which is the sum of the two separate inductors L_1' and L_4, for the modified tri-band load. This results in k' = 1. Also, by using the same capacitors of C_1 = 202.6 fF, $C_2' = C_2$ = 200 fF and $C_3' = C_3$ = 140.7 fF, the effective notch inductors L_{N1} and L_{N2} of the modified tri-band load can be mapped into the two notch inductors L_2 and L_3 of the conventional tri-band load, respectively, to maintain the same f_{S1} and f_{S2} according to (2.3) and (2.14), (2.15), so that $L_{N1} = L_2 = 316.6$ pH and $L_{N2} = L_3 = 200$ pH. Table 2.2 summarizes the component values for different values of k' and Fig. 2.4(a) shows the corresponding responses of the modified tri-band load. Table 2.2 also includes the values for f_{S1} and f_{S2} obtained through Fig.

TABLE 2.2
COMPONENT VALUES OF MODIFIED TRI-BAND LOAD

	k'=0	k'=0.25	k'=0.5	k'=0.75	k'=1	Unit
L_1'	0	50	100	150	200	pH
L_4	200	150	100	50	0	pH
L_2'	316.6	273.2	256	273.2	316.6	pH
L_3'	200	170.8	165.2	170.8	200	pH
f_{P1}	-	18.9	16.7	14.8	13.2	GHz
f_{P2}	25	25.5	26.4	26.1	24.4	GHz
f_{P3}	-	31.2	34	39	46.6	GHz
Q_{S1}	-	18.52	5.13	3.05	2.68	-
Q_{S2}	-	40	14.25	5.49	2.31	-

TABLE 2.3
COMPONENT VALUES FOR VARIOUS MODIFIED TRI-BAND LOADS

Component	Modified TB Load 1	Modified TB Load 2	Modified TB Load 3	Modified TB Load 4	Unit
L_1'	50	50	50	50	pH
L_4	25	50	100	150	pH
L_2'	298.8	289	278.6	273.2	pH
L_3'	185	178.7	173.2	170.8	pH
C_1	540.4	405.3	270.2	202.6	fF
C_2'	200	200	200	200	fF
C_3'	140.7	140.7	140.7	140.7	fF

2.4(a) and the stop-band Q. Finally, the two notch inductors L_2' and L_3' of the modified tri-band load can be obtained from (2.24) and (2.25), which are chosen to produce f_{S1} and f_{S2} as close to the desired frequencies of 20 and 30 GHz as possible. It is noted that, in Fig. 2.4(a), the graph with $k' = 1$ also represents the insertion loss of the conventional tri-band load with $k = 1$ described in Table 2.1 and shown in Fig. 2.3(b).

It is recognized that the only way to tune the pass-band frequencies of the conventional tri-band load is to change its L_1–C_1 tank values as shown in Fig. 2.3, which inadvertently affects the LNA gain and hence is not desirable. On the other hand, using a proper ratio k' between L_1' and L_4 by adjusting the two notch inductors L_2' and L_3' accordingly, the modified tri-band load can provide both the frequency tuning capability for the pass-bands and the Q-tuning ability for the stop-bands simultaneously. This phenomenon is depicted in Fig. 2.4(b) using the modified tri-band described in Table 2.3.

We recall the frequency tuning behavior of the conventional tri-band load (Fig. 2.2(a)) illustrated in Fig. 2.3(b) in which, as L_1 is reduced and C_1 is increased, f_{P1} and f_{P3} approach f_{P2}, making the lower and upper pass-bands narrower while keeping the stop-bands almost the same. As C_1 is increased, the LNA gain also becomes smaller, which is undesirable. On the other hand, for the modified tri-band load, as L_4 is increased and C_1 is reduced with fixed L_1', f_{P1} and f_{P3} also move closer to f_{P2}, yet the bandwidths of the three pass-bands and two stop-bands becomes wider and narrower, respectively, which are desirable. The narrower notch-width implies higher notch Q-factor. Therefore, the modified tri-band load can also increase the robustness of both pass-bands and stop-

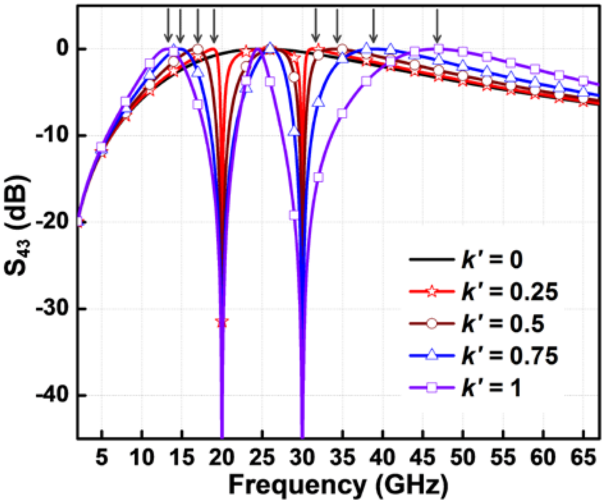

(a)

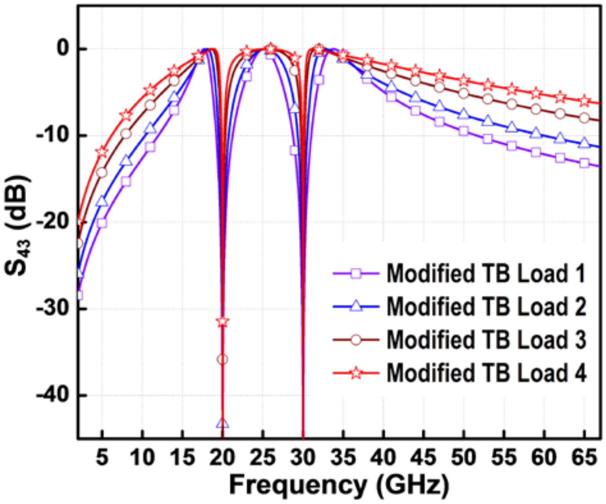

(b)

Fig. 2.4 Insertion losses of the modified tri-band load for different k' (a) and various modified tri-band loads in Table 2.3 (b). The top arrows denote the pass-bands of the tri-band load.

bands against the usual frequency shift at high frequencies caused by parasitic components and undesired coupling between interconnection lines. This frequency tuning behavior also leads to increased LNA gain in all pass-bands at high frequencies due to reduced C_1 and hence is desirable. These are the unique characteristics of the

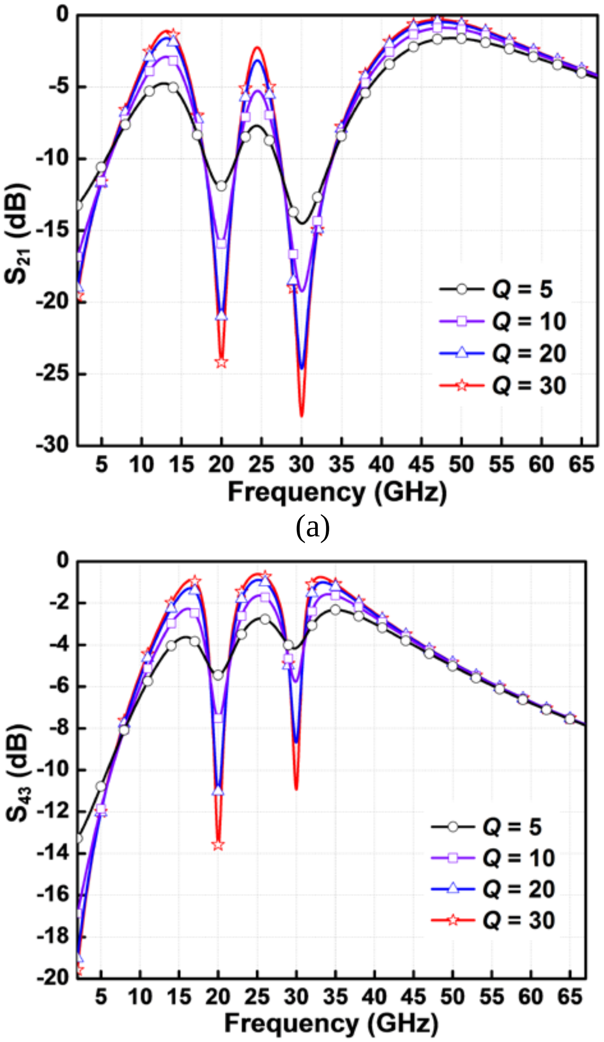

(a)

(b)

Fig. 2.5 Insertion losses of the conventional tri-band load (a) and modified tri-band load (b) as the Q-factor of the integrated inductors is changed from 5 to 30.

modified tri-band load, making it distinguishingly different from the conventional tri-band load.

The responses of both the conventional and modified tri-band loads are vulnerable to the low Q-factor of the integrated inductors for on-chip implementation as mentioned in Ch. I. To illustrate this, we show in Fig. 2.5 the insertion loss responses of the conventional and modified tri-band loads with varying Q-factor of the integrated inductors. As the Q-factor of the inductors is reduced, the gain balance between the pass-bands becomes worse and, especially, the stop-band rejection ratio degrades drastically. When the Q-factor is 10 at 25 GHz, which is a reasonable Q value in the frequency bands considered in this example, the maximum stop-band rejection ratios obtained from the conventional and the modified tri-band loads are only about 12 dB and 6 dB, respectively, which are not sufficient. This stop-band performance degradation has, in fact, been exhibited in most multiband LNAs using integrated passive inductors. In order to overcome this problem, a new feedback tri-band load configuration based on the modified tri-band load is proposed as follows.

2.4 Proposed Feedback Tri-band Load

Figure 2.6(a) shows the equivalent circuit model of the new feedback tri-band load. It is implemented using two feedback notches associated with an inverting amplifier ($-A$) in a closed-loop configuration to enhance the stop-band performance. The feedback tri-band load is formed partly from a transformation of the modified tri-band load described in Fig. 2.2(b). Specifically, the common AC ground node of C_2 and C_3 is detached from the power supply (V_{CC}) and rerouted to node Y of the feedback loop. Figs. 2.6(b) and (c) represent the equivalent circuit models looking into the feedback tri-band load at nodes X and Y, respectively. To facilitate our formulation and discussion, we show in Fig. 2.7 the insertion loss responses of the corresponding (open-loop load) equivalent circuits between ports 3-4 (S_{43}) in Fig. 2.6(b) and 5-6 (S_{56}) in Fig. 2.6(c), the impedances Z_L and Z_N at nodes X and Y, respectively, and the input impedance (Z_{11}) and transmission response (S_{21}) of the feedback tri-band load in Fig. 2.6(a), respectively. The final component values of the feedback tri-band load for the same frequency specifications of the conventional and modified tri-band loads are L_1=55 pH, L_2=110.7 pH, L_3=268 pH, L_4=135 pH, C_1=280 fF, C_2=200 fF, C_3=200 fF. These results have been

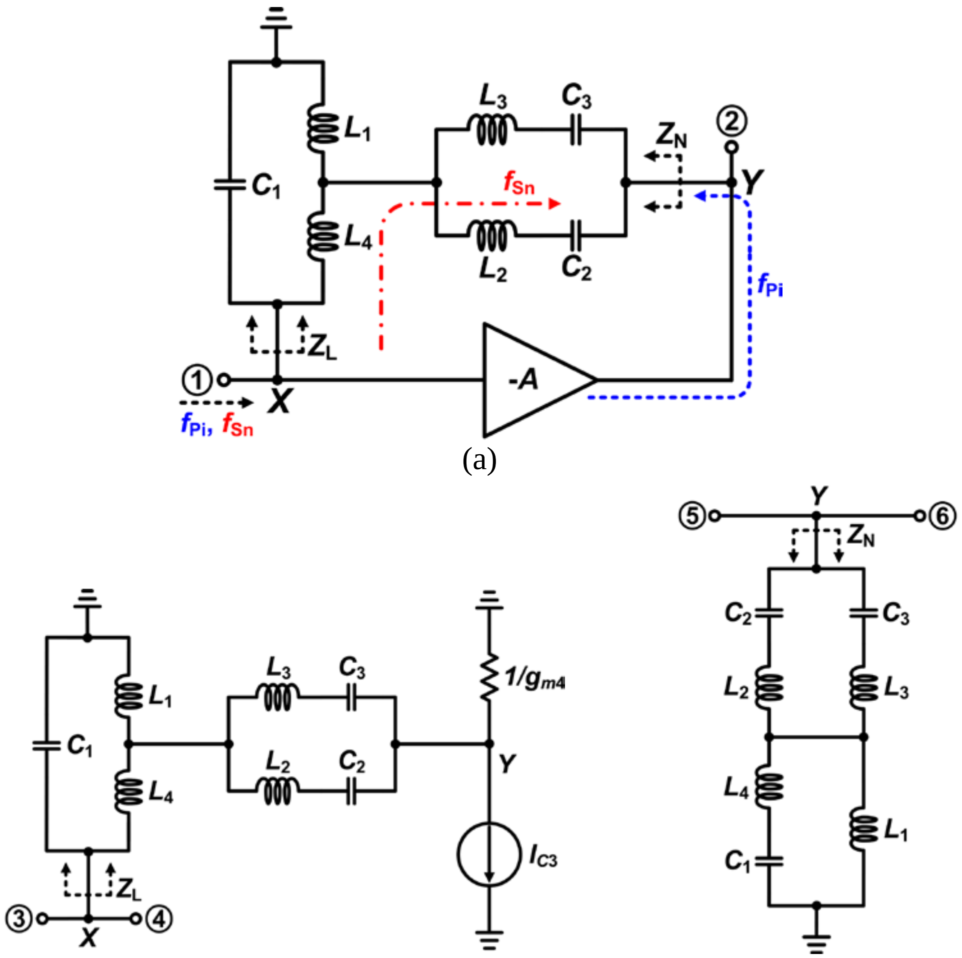

(b) (c)

Fig. 2.6 Equivalent-circuit models of the feedback tri-band load (a), (b) at node X, and (c) at node Y. f_{Pi} and f_{Sn} are the pass-band and stop-band frequencies, respectively.

obtained through several iterations based on the modified tri-band load with $k' = 0.25$. We use the same capacitors $C_2 = C_3 = 200$ fF for the feedback notches.

As seen in Fig. 2.7(b), at node X, each of the signals crossing three pass-bands corresponding to $f_{\mathrm{P}i}$ (i=1, 2, 3) sees a high-impedance load at each resonant frequency, whereas the two stop-band signals corresponding to $f_{\mathrm{S}n}$ (n=1, 2) see low-impedance

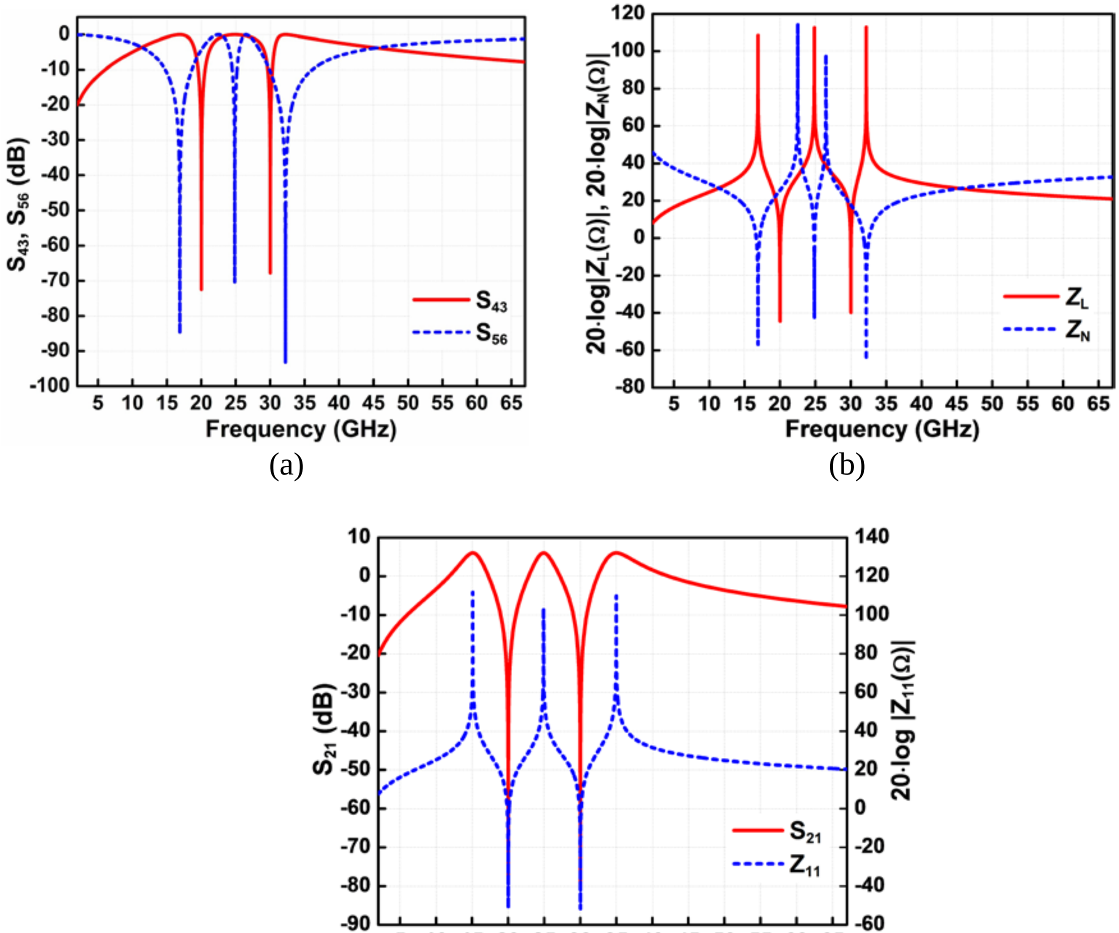

(a) (b)

(c)

Fig. 2.7 Insertion loss and impedance magnitudes of the equivalent circuits at nodes X, Y (a, b) and the feedback tri-band load (c).

loads. Therefore, most of the three pass-band signals and few of the two stop-band signals will go through the inverting amplifier. On the other hand, the majority of the two stop-band signals at node *X* flows into the tri-band load and feed-forwards to node *Y* via the notches.

For simplicity, we may assume $1/g_{m4}$ is negligibly small, and correspondingly the load impedance Z_L at node *X* in Fig. 2.6(b) can be equal to the impedance Z_{TB2} given in (2.13). While, the notch impedance Z_N at node *Y* in Fig. 2.6(c) can be derived as

$$\begin{aligned}
Z_{\mathrm{N}}(s) &= \frac{N_N(s)}{D_N(s)} \\
N_{\mathrm{N}}(s) &= s^6 L_S\left(L_2L_3 + L_2L_P + L_3L_P\right)C_1C_2C_3 \\
&\quad + s^4\begin{bmatrix} L_S\left(L_2+L_P\right)C_1C_2 \\ +(L_1L_2+L_2L_3+L_1L_3)C_2C_3 \\ +L_S\left(L_3+L_P\right)C_1C_3 \end{bmatrix} \\
&\quad + s^2\left[L_SC_1+(L_1+L_2)C_2+(L_1+L_3)C_3\right]+1 \\
D_N(s) &= s(s^2L_SC_1+1)\left[s^2(L_2+L_3)C_2C_3+(C_2+C_3)\right].
\end{aligned} \tag{2.26}$$

Comparing the impedances in (2.13) and (2.26) reveals that the numerator of Z_N is the reciprocal of the denominator of Z_L. Accordingly, the zeros of Z_N, corresponding to stop-band frequencies, are the same as the poles of Z_L, corresponding to pass-band frequencies, as clearly seen in Fig. 2.7(b), and satisfy (2.17)–(2.19). Therefore, a tri-band notch filter is created at node *Y* with its transmission response shown in Fig. 2.7(a). As a result, the pass-band signals see the low-impedance notches at node *Y* and are fed-back to node *X* through the notches. Meanwhile, the feed-forwarded and inverted stop-band signals from node *X* are combined together and cancelled out at node *Y*. Consequently, the feedback tri-band load in Fig. 2.6(a) can provide a negative feedback loop for the pass-band signals and a positive feed-forward path for the stop-band signals. Thereby, a clear concurrent tri-band response by the closed-loop operation can be obtained as shown in Fig. 2.7(c).

2.5 Summary and Conclusion

The new tri-band load composed of two passive LC notch filters with feedback has been proposed. It provides stable and high stop-band rejection especially needed in multiband components by overcoming the dependency of stop-band rejection performance on the low quality factor of integrated passive inductors. Also, the comparative analysis and comprehensive design principles of the conventional, modified, and new feedback tri-band loads were presented. It should be noted that the design principle of the feedback tri-band load with feedback notches is also applicable to the design of dual-band or multiband loads having more than three pass-bands.

CHAPTER III

CONCURRENT TRI-BAND LOW-NOISE AMPLIFIER*

This chapter presents a 13.5/24/35 GHz concurrent tri-band LNA implementing the proposed feedback tri-band load described in Ch. II. The developed concurrent tri-band LNA provides stable and high stop-band rejection ratios of more than 30 dB without additional area and power consumption. It achieves the lowest NF as well as the best SRRs among the reported concurrent tri-band LNAs. This LNA is the first concurrent tri-band LNA operating up to the mm-wave frequency regime.

3.1 Design of Concurrent Tri-band Low-Noise Amplifier

Figure 3.1 shows the schematic and main component values of the new concurrent tri-band LNA employing the feedback tri-band load with two feedback notches described in Ch. II. The tri-band LNA is based on a two-stage cascode topology to increase the forward gain and the reverse isolation. It has been designed using TowerJazz's 0.18-μm SiGe BiCMOS technology [16].

All transistors ($Q_{1\text{-}4}$) used in the tri-band LNA have identical size: one-finger emitter having 0.15-μm width and 10.16-μm length, and two-finger base and collector. The first and second stages consume 8 and 12 mA, respectively, from a 1.8-V supply

---

*© 2013 IEEE. Reprinted, with permission, from J. Lee and C. Nguyen, "A 13/24/35-GHz Concurrent Tri-band LNA with Feedback Notches," in *IEEE Topical Meetings on Silicon Monolithic Integrated Circuits in RF Systems (SiRF) Dig.*, Jan. 2013, pp. 252–254. and J. Lee and C. Nguyen, "A Concurrent Tri-Band Low-Noise Amplifier With a Novel Tri-Band Load Resonator Employing Feedback Notches," *IEEE Transaction on Microwave Theory and Techniques*, vol. 61, no.12, pp. 4195–4208, Dec. 2013.

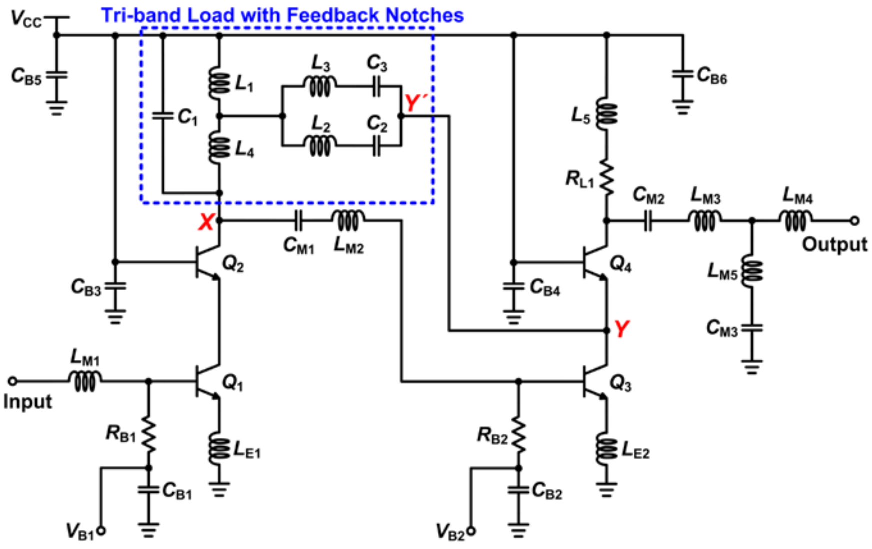

Component	Value	Unit
L_1	40	pH
L_2	230	pH
L_3	120	pH
L_4	160	pH
L_5	310	pH
L_{M1}	220	pH
L_{M2}	20	pH
L_{M3}	20	pH
L_{M4}	120	pH
L_{M5}	320	pH
L_{E1}	30	pH
L_{E2}	18.5	pH
C_1	70	fF
C_2	220	fF
C_3	220	fF
C_{M1}	300	fF
C_{M2}	254	fF
C_{M3}	33	fF
R_{L1}	21.7	Ω
$R_{B1,2}$	2	kΩ

Fig. 3.1 Schematic and component values of the new concurrent tri-band LNA using the feedback tri-band load.

voltage, which result in g_{m1} = 284 mS, g_{m2} = 283 mS, g_{m3} = 422 mS, and g_{m4} = 416 mS. The maximum f_T of 240 GHz is obtained from Q_3.

Referring to the feedback tri-band load shown in Fig. 2.6, node Y of the tri-band load is located between transistors Q_3 and Q_4 in the second stage amplifier as seen in Fig. 3.1. For simplicity, we assume that the transconductance g_{m3} and g_{m4} of Q_3 and Q_4, respectively, are identical and the output impedance of Q_2 is high enough. Also, we ignore the small degeneration inductor L_{E2} and the inter-stage matching components C_{M1} and L_{M2}. Then, from node X to Y, Q_3 can be represented as an ideal inverting amplifier with voltage gain (A) of 1 ($\approx g_{m3} \times 1/g_{m4}$). Thus, the feedback tri-band load using two passive notches embedded into the tri-band LNA closes a feedback loop with the inverting amplifier, as mentioned in Ch. II (See Fig. 2.6(a)).

Spiral inductors are used for the wideband loads (L_4, L_5) and the out-of-band rejection notch (L_{M5}), while microstrip transmission lines are used for inductors $L_{M1\text{-}4}$, $L_{E1\text{-}2}$, and $L_{1\text{-}3}$ for the input, output, and inter-stage matching purposes and the stop-band notches due to their high Q-factor at the desired frequencies. The input and output RF pads are also taken into account in the design of the matching networks. Approximate values for these inductors are provided in Fig. 3.1. For accurate design and accounting for the unavoidable parasitics and coupling effects, all inductors and interconnection lines are thoroughly characterized by the EM simulator IE3D [17].

The previously reported tri-band LNAs in [14] and [15] used three distinct resonators for the input matching at the desired frequencies. These tri-band input matching networks require more inductors and capacitors as compared to a wideband input matching network. Moreover, the noise introduced by the tri-band matching network and the unwanted coupling from the complex routing between the components and signal lines increases, especially at millimeter-wave frequencies. In order to achieve low NF, the proposed tri-band LNA adopts a wideband input matching technique using only a single high-Q inductor designed using a microstrip line at the base of Q_1 [18]. This simple wideband input matching technique can also minimize the undesired coupling by avoiding the routing complexity of the tri-band resonator components, which in turn leads to less die area. The input matching network of the proposed tri-band LNA is composed of L_{M1}, L_{E1}, and capacitance C_{PAD} between the input RF-pad and the substrate (not shown). The emitter degeneration inductors L_{E1} and L_{E2} are used to enhance the matching and stability. Since the base inductor L_{M1} directly affects the NF,

L_{M1} has been designed to exhibit not only minimum resistive loss needed for low NF, but also proper inductance for wideband input matching covering the whole tri-band. It is particularly noted that, while the noise and gain matching in single-band LNAs can be obtained simultaneously, it is extremely difficult to achieve both noise and gain matching simultaneously for multi-band LNAs. Moreover, simultaneous multi-band gain and NF matching at the input of LNAs would require many passive components, and hence inadvertently degrading the NF due to the resistive loss originated from the passive components. The employed wide-band matching technique can minimize the NF, thereby lessening the need and hence difficulty in simultaneous tri-band gain and NF matching.

The second-stage load is composed of L_5 and R_{L1}, and the output matching network consists of C_{M2-3} and L_{M3-5}. The output RF pad is also included in the output matching network. The load resistor R_{L1} enhances the stability and acts as a de-Q resistor, reducing the Q of L_5 to achieve wideband output matching characteristic. In order to obtain a distinct third pass-band and suppress undesired out-of-band interferences at higher frequencies, a band-stop filter composed of L_{M5} and C_{M3}, having a zero around 52 GHz, is inserted at the output of the second stage. Fig. 3.2 shows the simulated power gain of the tri-band LNA with and without the out-of-band rejection filter. As can be seen, the filter introduces a sharp roll-off skirt characteristic above 40 GHz and provides more than 20-dB out-of-band rejection ratio at 52 GHz.

The load inductor L_4 is realized by a spiral inductor and a microstrip inductor in order to reduce the layout area as well as the overall Q of the inductor. Thus, L_4 mainly

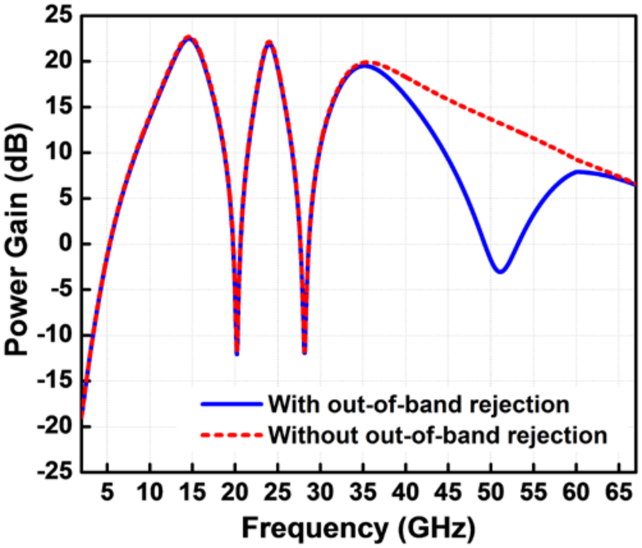

Fig. 3.2 Simulated power gain of the tri-band LNA with and without the out-of-band rejection filter.

contributes to the wideband load characteristic in conjunction with C_1. The other part of the load inductor, L_1, and the two feedback notch inductors, L_2 and L_3, are designed using microstrip lines to maximize the inductor Q. The approximate Q-factors of 28, 25, 28, and 16 are obtained for L_1, L_2, L_3, and L_4, respectively, by EM simulations. Note that since the load capacitor C_1 includes the parasitic capacitance at node X originated from the loading effects of C_{M1} and L_{M2} in the actual layout, its value (70 fF) is reduced from that (280 fF) of the ideal feedback tri-band load shown in Fig. 2.6(a), while others remain close to those of the feedback tri-band load as presented in Ch. II.

As mentioned in the preceding section, the feedback tri-band load using feedback network provides more stop-band rejection and stable stop-band performance as compared to the conventional and the modified tri-band loads. These advantages of the feedback tri-band load can be verified by considering the alternative loads as shown in

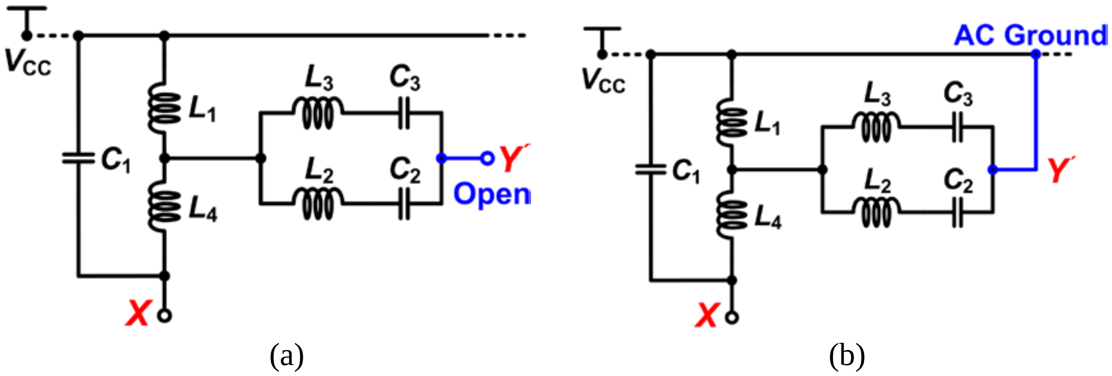

Fig. 3.3 Alternative loads of the first stage to verify the effectiveness of the new feedback tri-band load with feedback notches: (a) wideband load by opening node Y' and (b) modified tri-band load by grounding node Y'.

Fig. 3.3. These alternative loads are obtained by disconnecting the common node Y' between C_2 and C_3 from the node Y in the second stage of the tri-band LNA in Fig. 3.1: a wideband load by letting the common node Y' open and a modified tri-band load by rerouting the common node Y' to the power supply node V_{CC} as shown in Figs. 3.3(a) and (b), respectively. For verification purpose, these alternative loads are assumed to maintain the same load configuration and share the same components modeled by EM simulations from the feedback tri-band load; only the routing of node Y' is changed using an ideal line.Figure 3.4 shows the simulated results for the tri-band LNA using the two alternative and feedback tri-band loads. These responses have the same center frequency of 24 GHz. With the wideband load, obtained when node Y' is open, the response is wideband as exhibited by the parallel tank of C_1, L_1, and L_4. With the modified tri-band load, obtained when node Y' is connected to V_{CC}, the response displays a tri-band gain characteristic. However, since the Q-factor of the modified tri-band load is limited by

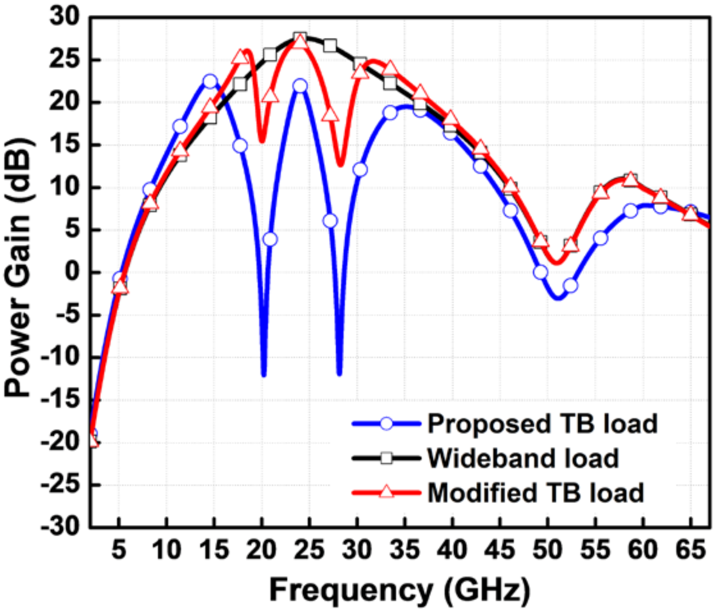

Fig. 3.4 Simulated power gain of the tri-band LNA with the feedback tri-band load, modified tri-band load, and wideband load.

that of the passive inductors, the stop-band rejection ratio can only reach 12 and 15 dB in the low and high stop-band, respectively.

Apparently, the concurrent tri-band LNA with the new feedback tri-band load exhibits deeper notch responses with more than 35-dB stop-band rejection ratio in both stop-bands, besides showing a clearer tri-band gain characteristic. In result, the tri-band LNA also maintains a good gain imbalance, which characterizes the gain difference between the highest and lowest peak gains in the three pass-bands, to below 3 dB with the well-balanced high notch depths at both stop-bands.

It is interesting to investigate the sensitivity of the stop-band rejection ratio against the inverting amplifier gain A in a closed loop operation. For the balanced notch depths, we recall that the second-stage transistors Q_3 and Q_4 exhibit g_{m3} = 422 mS and

g_{m4} = 416 mS, respectively, which lead to an amplifier gain of 1.01 ($g_{m3} \times 1/g_{m4}$). In the investigation, we adjust the bias current corresponding to g_{m4} of Q_4 and hence sweep the inverting amplifier gain, while keeping the bias current for g_{m3} of Q_3 the same. The

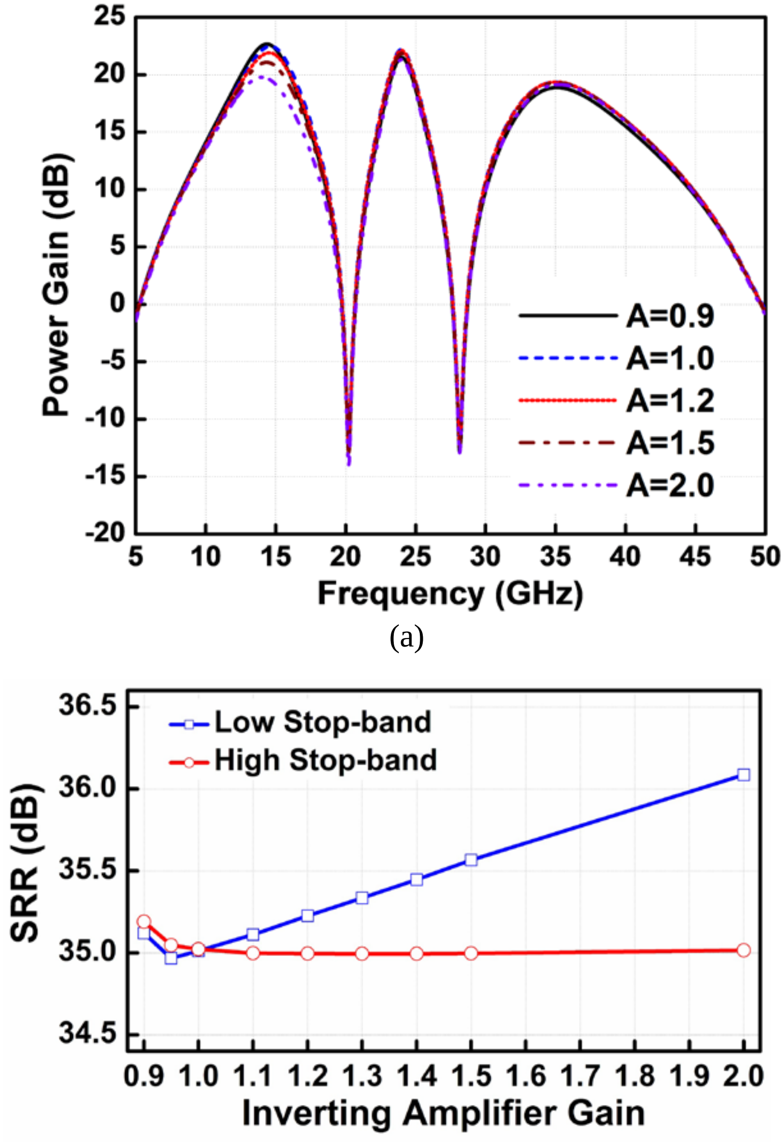

(a)

(b)

Fig. 3.5 Simulated power gain for different inverting amplifier gain A (a) and stopband rejection ratio (SRR) as a function of A (b) of the tri-band LNA.

inverting amplifier gain is tuned from 0.9 to 2.0, which ensures that Q_3 and Q_4 are in the forward active region. Fig. 3.5(a) shows the power gain of the tri-band LNA for different inverting amplifier gains. The high balanced notch depth responses at both stop-bands are well maintained with maximum gain degradation of about 2.9 dB in the first pass-band. The stop-band rejection ratios in both stop-bands remain around 35 dB or better as shown in Fig. 3.5(b). The results show that stable and high stop-band rejection performances over process variation and parasitic components can be achieved by the nature of the negative feedback network as discussed in [19].

3.2 Experimental and Simulated Results

The concurrent tri-band LNA was fabricated using TowerJazz's 0.18-μm SiGe BiCMOS process [16]. All inductors and most interconnection lines were implemented with the two topmost metal layers. The input and output RF pads with shield in the bottom-most metal layer have been designed to exhibit optimal capacitance to the substrate and satisfy the wideband matching requirement as parts of the matching networks described earlier. Fig. 3.6 shows the die photograph of the fabricated tri-band LNA. It occupies 1180 μm × 500 μm including RF pads.

The concurrent tri-band LNA was measured on-wafer. Fig. 3.7 shows the measured and simulated results for gain, NF, return loss, and reverse isolation. As can be seen in Fig. 3.7(a), the tri-band LNA exhibits measured power gains of 22.4/23.7/20.2 dB at 13.5/24/35 GHz, respectively, and maximum gain imbalance of 3.5 dB. The measured stop-band rejection ratios from the peak gain at 24 GHz to the loss at 17.7 GHz (low stop-band) and 28.7 GHz (high stop-band) are 41 and 30 dB, respectively. The

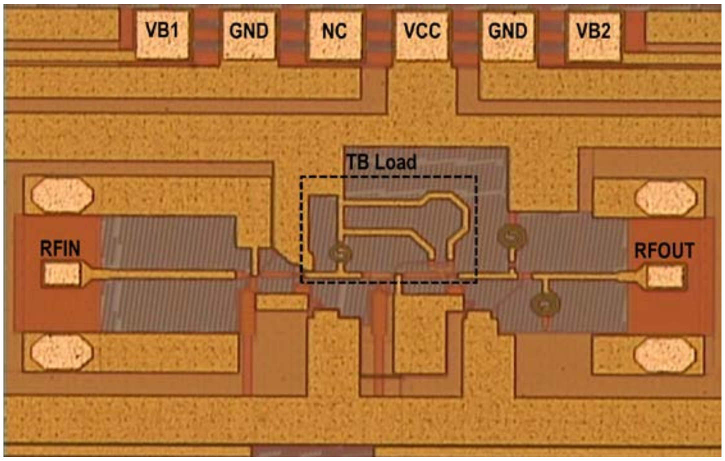

Fig. 3.6 Die micrograph of the fabricated concurrent tri-band LNA.

measured 3-dB pass-bands are 11.2–15.2, 22.4–25.8, and 32.1–38.5 GHz. Fig. 3.7(b) shows the best measured NF in the first, second, and third pass-band are 3.4, 3.2, and 3.7 dB, respectively. The measured input (S_{11}) and output (S_{22}) return losses are more than 9.5 and 7 dB, respectively, as seen in Fig. 3.7(c), and the measured reverse isolation (S_{12}) remains more than 45 dB across the entire tri-band as shown in Fig. 3.7(d). Fig. 3.8 shows the measured stability factors, satisfying the necessary and sufficient conditions for unconditional stability, $K > 1$ and $B_1 > 0$ [20]. Fig. 3.9 shows the measured input P_{1dB} (IP_{1dB}) and input IP_3 (IIP_3) with 1-MHz two-tone space at each peak-gain frequency. The

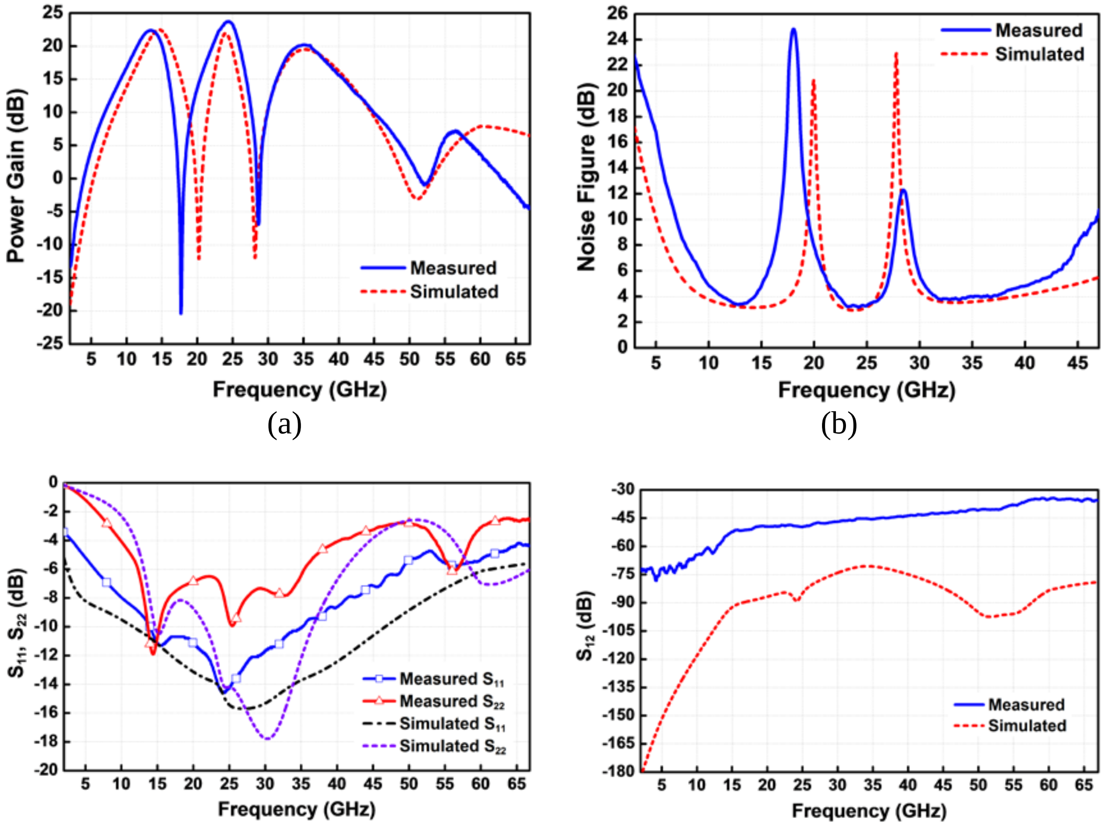

(a) (b)

(c) (d)

Fig. 3.7 Measured and simulated results for (a) power gain, (b) NF, (c) S_{11} and S_{22}, and (d) S_{12}.

tri-band LNA achieves IP_{1dB} of –21/–26.7/–24.1 dBm and IIP_3 of –13.5/–17.1/–16.1 dBm at 13.5/24/35 GHz, respectively. It consumes 36 mW with a supply voltage of 1.8 V.

Table 3.1 summarizes the measured performance of the concurrent tri-band LNA and those of published concurrent multiband LNAs. As can be seen, most concurrent dual-band and tri-band LNAs were designed for low-GHz RF applications except those in [10] and [11]. The developed tri-band LNA exhibits the best NF performance among the tri-band LNAs, while operating at much higher frequencies, and the dual-band LNAs reported in [10] and [11] which operate in similar frequency bands to 24 GHz. It also has better gain than most of the reported dual-band LNAs and tri-band LNAs, except [11] at 10 GHz which is a dual-band LNA and [13] which is a tri-band LNA operating at much lower frequencies. Also, the developed tri-band LNA achieves the best stop-band rejection ratios among the reported tri-band LNAs. The developed LNA is the first concurrent tri-band LNA operating up to the mm-wave frequency regime.

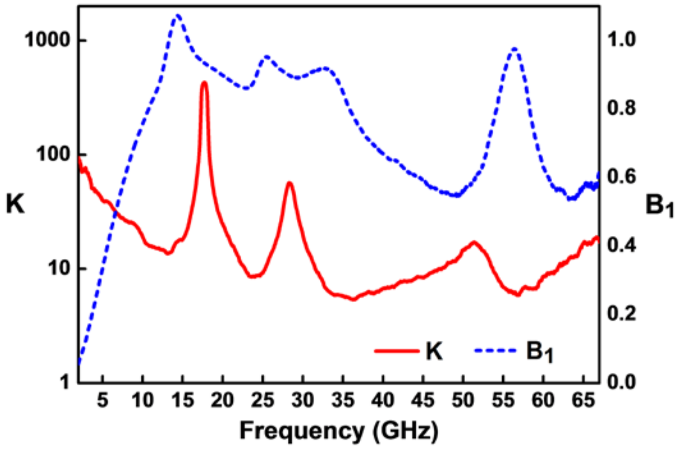

Fig. 3.8 Measured stability factors *K* and B_1.

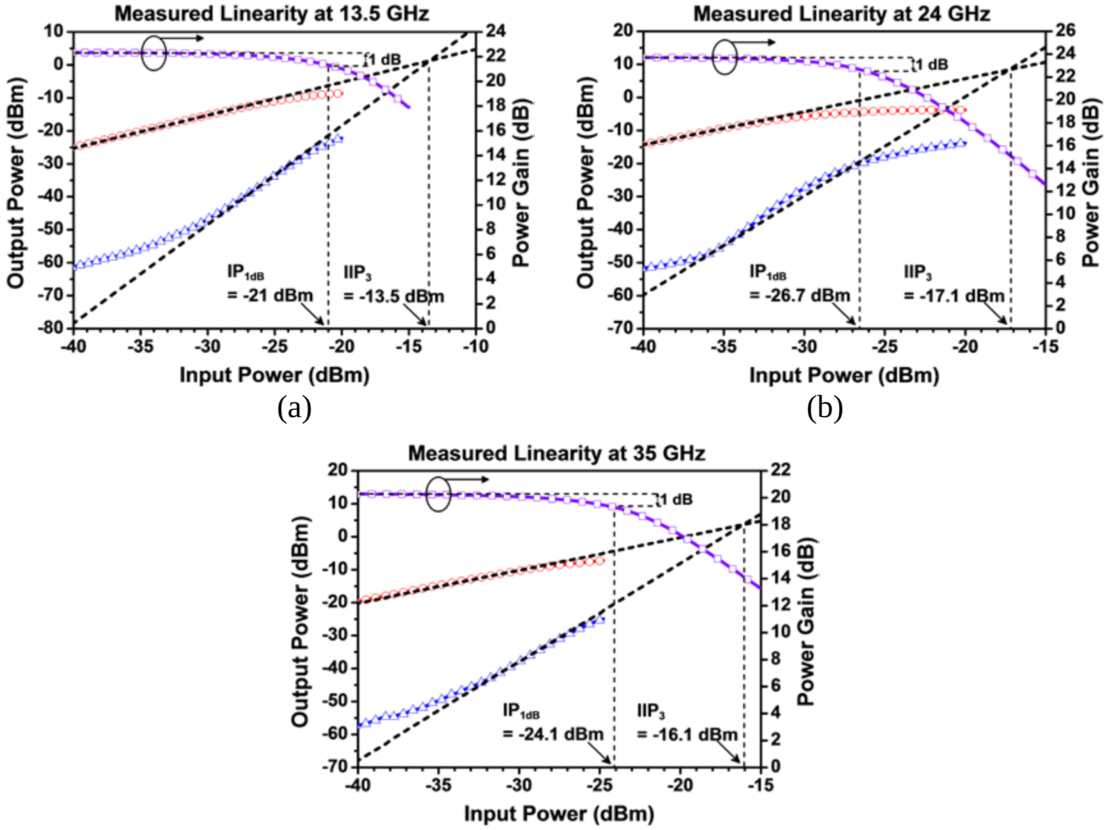

(a) (b)

(c)

Fig. 3.9 Measured input P_{1dB} and input IP_3 at: (a) 13.5 GHz, (b) 24 GHz, and (c) 35 GHz.

3.3 Summary and Conclusion

A 13.5/24/35-GHz concurrent tri-band LNA employing a novel feedback tri-band load with two feedback notch filters has been successfully implemented with excellent performance for the first time. The comparative analysis and comprehensive design principles of the conventional, modified, and new feedback tri-band loads have been presented. The effectiveness of the feedback tri-band load toward high stop-band rejection has been demonstrated. The proposed concurrent tri-band LNA using feedback notch technique can be implemented at other frequencies and expanded for other

TABLE 3.1
PERFORMANCE SUMMARY OF THE DEVELOPED CONCURRENT TRI-BAND LNA AND EXISTING CONCURRENT MULTIBAND LNAS

Ref.	Technology	Frequency (GHz)	Gain (dB)	NF (dB)	IIP$_3$ (dBm)	S$_{11}$ (dB)	Pass-band Gain Imbalance (dB)	Stop-band Rejection Ratio[b] (dB)	Power (mW)	Area (mm^2)
[5]	0.35-μm CMOS	2.45	14	2.3	0	–25	1.5	43	10	0.64
		5.25	15.5	4.5	5.6	–15				
[6]	0.18-μm CMOS	2.4	7.6	5.7	–1.5	–9.4	1	30	10.8	1.15
		5.7	8.6	6.8	–2.4	–6.2				
[7]	0.25-μm SiGe:C BiCMOS	2.14	20	2.8	–12.8	–12	6.2	25	13.2	0.95
		5.25	13.8	3.7	–10.3	–20.7				
[9]	0.35-μm SiGe BiCMOS	2.3	14.4	2.5	N/A	–12.8	0.1	26.1	11.9	0.29
		4.5	14.3	3.0	N/A	–11.5				
[10]	0.18-μm CMOS	18	9.2	5.7	–2	–23	2.8	9	8	0.33
		24.5	12	6.4	–3	–24				
[11]	0.13-μm CMOS	10	25.3	5.3	N/A	–24.4	13.2	44	12	1.14
		24	12.1	10.4	N/A	–17.9				
[13]	0.18-μm CMOS	0.945	18	4.6	–12.8	–7	6	8 / 8	32.4	1.34
		2.4	24	4.4	–15.3	–15				
		5.25	23	4.4	–14.7	–10				
[14][a]	0.25-μm CMOS	1.8	10.1	3.7	1.7	–10.6	1.7	8 / 24	39	1.68
		2.45	10.8	4.7	0	–10.4				
		5.25	11.8	6.3	4.5	–19.9				
[15][a]	0.18-μm CMOS	2.4	11.8	3.8	–3.0	–-10.3	1.8	5.3 / 7.7	13.5	0.75
		3.5	11.7	4.0	–2.1	–10.4				
		5.2	10	3.7	–0.4	–13.5				
This Work	**0.18-μm SiGe BiCMOS**	**13.5**	**22.4**	**3.4**	**–13.5**	**–9.5**	**3.5**	**41 / 30**	**36**	**0.59**
		24	**23.7**	**3.2**	**–17.1**	**–14.5**				
		35	**20.2**	**3.7**	**–16.1**	**–10.1**				

[a] Only simulated performances are reported.

[b] Difference between maximum pass-band gain and (low/high) stop-band loss.

concurrent multiband LNAs having dual-band or more than three pass-bands, which are attractive for multiband RF systems. Furthermore, the proposed feedback notch technique is an attractive solution for rejecting large image or blocker signals.

CHAPTER IV

CONCURRENT DUAL-BAND LOW-NOISE AMPLIFIERS[*]

To create apparent multiple passband and stopband responses, several concurrent multiband LNAs based on single-input single-output (single-to-single) topologies have been developed at microwave and millimeter-wave frequencies. The positive feedback transmission-line-based *LC*-ladder network [10] and synthetic quasi-TEM transmission lines [11] were employed to build the dual-band matching circuits. However, these dual-band LNAs suffer from low SRR at stopband [10] and large gain and NF imbalances between the passbands [11]. The concurrent dual-band LNA in [21] uses two active notch filters to overcome the low Q-factor of the integrated inductors, but it requires additional area and/or power dissipation. The concurrent tri-band LNAs presented in [22] and [23], which are reported in Ch. III, exhibit good gain balance and SRRs by employing a feedback tri-band load as compared to the previous works. However, the stopband performance of the feedback tri-band load is still governed by the notch capacitor values, which is prone to process variation, as well as the effective Q-factor of the feedback notch inductors affected by the physical inductor size relying on the given layout periphery of the feedback path. Therefore, controlling the effective Q-factor of the feedback notch filter would be necessary to maintain the high stopband rejection performance over unavoidable variations including process, voltage, and temperature.

---

[*] © 2015 IEEE. Reprinted, with permission, from J. Lee and C. Nguyen, "K-/Ka-band concurrent dual-band low-noise amplifiers using novel feedback dual-band loads with stopband rejection control," submitted to *IEEE Transaction on Microwave Theory and Techniques*, July 2015.

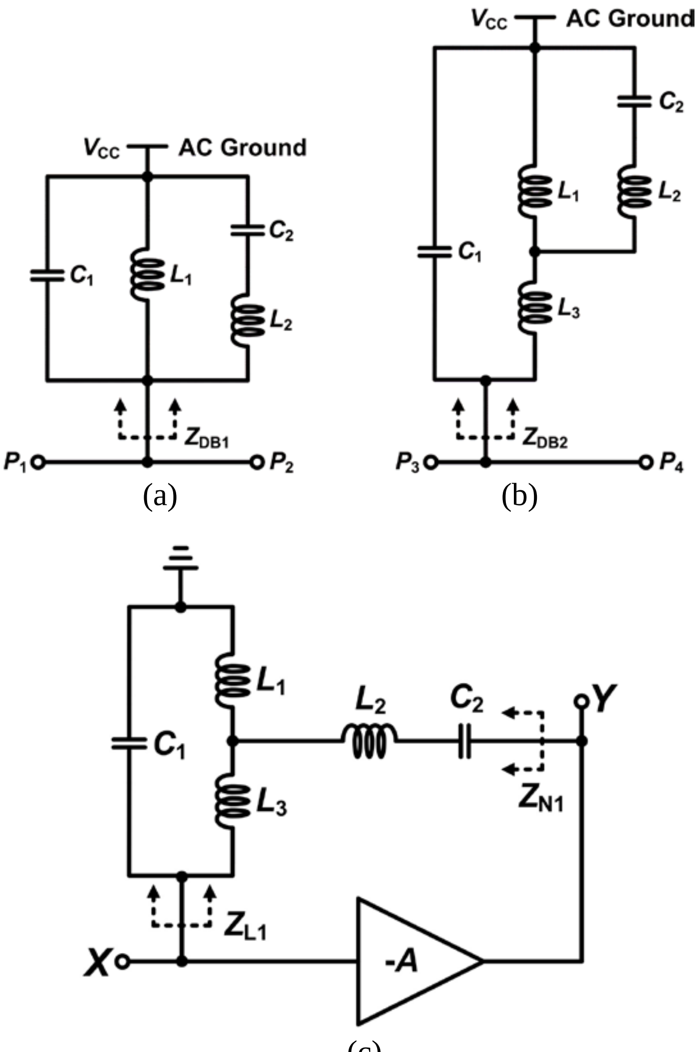

(a) (b)

(c)

Fig. 4.1 (a) Conventional and (b) modified dual-band loads. (c) Equivalent circuit of the proposed inductor feedback dual-band load.

To overcome these problems, two concurrent dual-band LNAs are proposed by employing two different types of feedback dual-band loads that significantly expand the feedback notch technique presented in the concurrent tri-band LNA in [23] and Ch. III of this dissertation. The developed concurrent dual-band LNAs are realized in a 0.18-μm BiCMOS process and are capable of controlling the stopband rejection performance by varying the bias levels of the constituent second-stage's inverting amplifier. The analyses and designs of the conventional and proposed feedback dual-band loads are firstly described to provide the insight and signify the advantages of the feedback loads. Then, a 21.5/36.5-GHz concurrent dual-band LNA with an inductor feedback dual-band load and another 23/36-GHz concurrent dual-band LNA with a new transformer feedback dual-band load are presented. The latter provides more degrees of freedom for the creation of the stopband and passbands as compared to the former. Both the developed concurrent dual-band LNAs achieve the best NF and gain-balance performance among the concurrent multiband LNAs reported at high microwave and millimeter-wave frequencies.

4.1 Analysis and Design of Concurrent Dual-band Loads

4.1.1 Conventional Dual-band Load

Figure 4.1(a) shows a conventional dual-band load [5], [21]. It is formed by combining the wideband resonator (L_1–C_1) and the stop-band notch filter (L_2–C_2) in parallel. The impedance Z_{DB1} of the conventional dual-band load is obtained as

$$\begin{aligned}
&Z_{\mathrm{DB1}}(s) = \frac{N_{\mathrm{DB1}}(s)}{D_{\mathrm{DB1}}(s)} \\
&N_{\mathrm{DB1}}(s) = sL_1(1+s^2L_2C_2) \\
&D_{\mathrm{DB1}}(s) = s^4L_1L_2C_1C_2 + s^2(L_1C_1 + L_2C_2 + L_1C_2) + 1.
\end{aligned} \tag{4.1}$$

By letting N_{DB1} and D_{DB1} in (4.1) equal to zero, the stopband notch frequency ($\omega_{S,DB1}$) and the two passband frequencies ($\omega_{P1,2,DB1}$) can be found respectively as

$$\omega_{S,DB1} = \frac{1}{\sqrt{L_2C_2}} \tag{4.2}$$

$$\omega_{P1,2,DB1} = \sqrt{\frac{\frac{C_1}{C_2}+\frac{L_2}{L_1}+1\pm\sqrt{\left(\frac{C_1}{C_2}+\frac{L_2}{L_1}+1\right)^2-4\frac{C_1L_2}{C_2L_1}}}{2C_1L_2}}. \quad (4.3)$$

Since the Q-factor of capacitor is usually much higher than that of an integrated inductor, the stopband rejection performance of the conventional dual-band load, as inferred from (4.2), mainly depends on the Q-factor of the notch inductor L_2 [23]. To overcome this issue, a modified dual-band load is created by separating the wideband load inductor L_1 in Fig. 4.1(a) into two inductors L_1 and L_3 as depicted in Fig. 4.1(b). The impedance Z_{DB2} of the modified dual-band load impedances can be derived as

$$\begin{aligned} &Z_{\mathrm{DB2}}(s)=\frac{N_{\mathrm{DB2}}(s)}{D_{\mathrm{DB2}}(s)} \\ &N_{\mathrm{DB2}}(s)=s^3[(L_1+L_3)L_2+L_1L_3]C_2+s(L_1+L_3) \\ &D_{\mathrm{DB2}}(s)=s^4[(L_1+L_3)L_2+L_1L_3]C_1C_2 \\ &\qquad\qquad +s^2[(L_1+L_3)C_1+(L_1+L_2)C_2]+1. \end{aligned} \quad (4.4)$$

From N_{DB2} and D_{DB2} in (4.4), the stopband and passband frequencies of the modified dual-band load can be found as

$$\omega_{S,DB2} = \sqrt{\frac{1}{(L_2+\frac{L_1L_3}{L_1+L_3})C_2}} = \sqrt{\frac{1}{(L_2+L_P)C_2}} \quad (4.5)$$

where $L_P=L_1L_3/(L_1+L_3)$, and

$$\omega_{P1,2,DB2} = \sqrt{\frac{\frac{L_1+L_2}{L_1+L_3}\cdot\frac{C_2}{C_1}+1\pm\sqrt{\left(\frac{L_1+L_2}{L_1+L_3}\cdot\frac{C_2}{C_1}+1\right)^2-4\frac{C_2}{C_1}\cdot\frac{L_2+\frac{L_1L_3}{L_1+L_3}}{L_1+L_3}}}{2C_2\left(L_2+\frac{L_1L_3}{L_1+L_3}\right)}}, \quad (4.6)$$

respectively. The notch inductor L_2 in the dual-band loads should be designed to meet the required inductance value for creating the stopband at the desired notch frequency described in (4.2) and (4.5).

With given passband and stopband frequencies, it is straight forward to determine the required inductor and capacitor values of the conventional and modified dual-band loads with (4.2)–(4.3) and (4.5)–(4.6), respectively. Comparing (4.2) and (4.5), it is evident that the modified dual-band load provides an additional degree of freedom in selecting the stopband notch frequency by adjusting the parallel inductance L_P consisting of L_1 and L_3. However, the stopband rejection performance is still limited by the effective Q-factors of the (passive) inductors L_2 and L_P. In order to compensate for the low Q-factor of the inductors, two new dual-band loads based on the feedback concept are proposed and implemented with inductor and transformer as follows.

4.1.2 Proposed Inductor Feedback Dual-band Load

Figure 4.1(c) shows the equivalent circuit of the proposed feedback dual-band load with an inductor notch. Even though this inductor feedback dual-band load is designed based on the feedback tri-band load in [23], it is necessary to describe its operation and design principles in order to understand the principle behind the development of the new transformer-based feedback dual-band load as well as to introduce unique characteristics of controlling the stopband rejection performance of the developed dual-band LNAs to be described in Section 4.2.

The inductor feedback dual-band load in Fig. 4.1(c) is created by rerouting the AC ground node of C_2 of the modified dual-band load in Fig. 4.1(b) to node Y of the inverting amplifier ($-A$) to form a closed loop. As illustrated in the schematic of the concurrent dual-band LNA shown in Fig. 4.3 (to be described later), this AC ground node is connected to node Y of the LNA's second stage. Referring to Fig. 4.1(c), the feedback dual-band load impedance Z_{L1} seen at node X is same as Z_{DB2} in (4.4) and can be obtained as

$$\begin{aligned} Z_{\mathrm{L1}}(s) &= Z_{\mathrm{DB2}}(s) = \frac{N_{\mathrm{L1}}(s)}{D_{\mathrm{L1}}(s)} \\ N_{\mathrm{L1}}(s) &= s^3[(L_1+L_3)L_2+L_1L_3]C_2 + s(L_1+L_3) \\ D_{\mathrm{L1}}(s) &= s^4[(L_1+L_3)L_2+L_1L_3]C_1C_2 \\ &\quad + s^2[(L_1+L_3)C_1+(L_1+L_2)C_2]+1. \end{aligned} \tag{4.7}$$

while, the notch impedance seen at node Y is derived as

$$\begin{aligned} Z_{\mathrm{N1}}(s) &= \frac{N_{\mathrm{N1}}(s)}{D_{\mathrm{N1}}(s)} \\ N_{\mathrm{N1}}(s) &= s^4[(L_1+L_3)L_2+L_1L_3)C_1C_2 \\ &\quad + s^2[(L_1+L_3)C_1+(L_1+L_2)C_2]+1 \\ D_{\mathrm{N1}}(s) &= s^3(L_1+L_3)C_1C_2 + sC_2. \end{aligned} \tag{4.8}$$

At node X, since $Z_{\mathrm{L1}} = Z_{\mathrm{DB2}}$, most of the stopband signal experiences a low impedance load, hence flowing into the embedded dual-band load and then feed-forwarding to node Y. On the other hand, the two passband signals see a high impedance load at node X, forcing them to travel toward the inverting amplifier together with a small amount of the residual stopband signal. Since most of feedforwarded and few of the inverted stopband signals are out-of-phase at node Y, they are cancelled out. Interestingly, as can be seen, the numerator N_{N1} in (4.8) is equal to the denominator D_{L1} in (4.7). This phenomenon creates a dual-band notch filter at the passband frequencies at node Y. Therefore, the passband signals see the low impedance Z_{N1} through the feedback path of the notch filter. The inductor feedback dual-band load indeed establishes a negative feedback loop with the inverting amplifier. As a result, a clear concurrent dual-band response with high stopband rejection performance can be achieved due to the interaction between the negative feedback passband signals and the cancellation of the feedforwarded and inverted stopband signals in the proposed feedback dual-band load.

4.1.3 Proposed Transformer Feedback Dual-band Load

Proper value for the notch inductor L_2 in the inductor feedback dual-band load is needed to create the desired stopband. However, the physical layout area of L_2 depends on the geometric dimension of the feedback path from the output node Y of the inverting amplifier to the input node X. This imposes difficulty in the design of the high-Q notch inductor and restricts the use of the inductor feedback notch technique in spite of its good stopband rejection capability. To overcome this restriction, another feedback dual-band load employing a transformer notch instead of an inductor notch is proposed as shown in Fig. 4.2. Fig. 4.2(a) shows a new dual-band load constructed by replacing the notch inductor L_2 in Fig. 4.1(b) with the transformer L_T. Fig. 4.2(b) illustrates the proposed transformer feedback dual-band load formed by rerouting the AC ground node of C_2 to node Y.

The transformer operates based on the mutual inductance (M) between the primary (L_{2P}) and secondary (L_{2S}) inductors. Apparently, the transformer notch provides

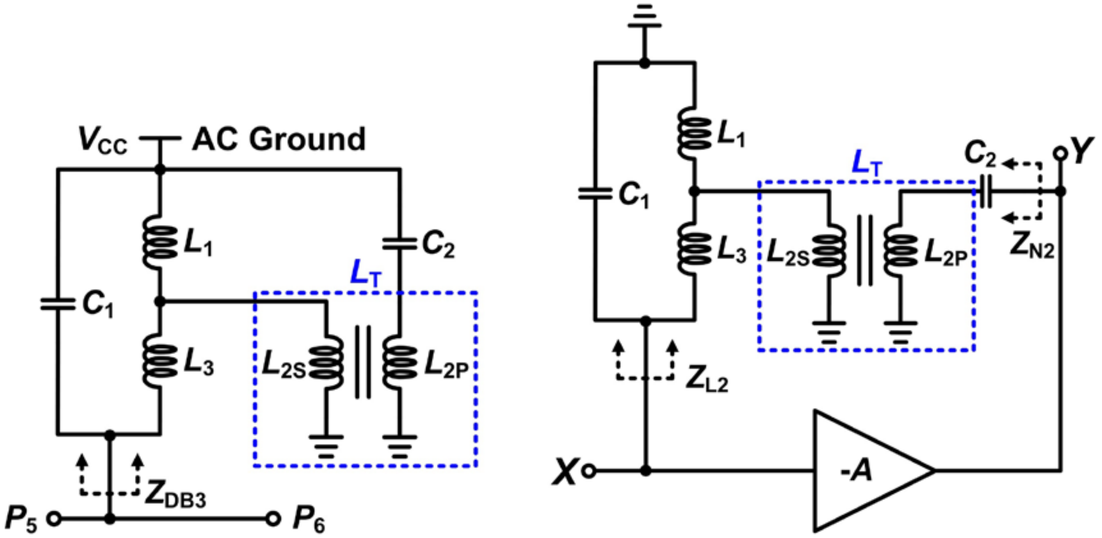

(a) (b)

Fig. 4.2 (a) Transformer-based dual-band load and (b) equivalent circuit of the proposed transformer feedback dual-band load.

more degrees of freedom to create the stopband response as compared to the single-inductor notch of the inductor feedback dual-band load described in Section II.A. The mutual inductance of the transformer can be represented as $M = k\sqrt{L_{2P}L_{2S}}$, where k is the magnetic coupling coefficient. By replacing the notch inductance L_2 in (4.5) with the transformer mutual inductance M, the stopband frequency of the proposed transformer feedback dual-band load can be obtained as

$$\omega_{S,DB3} = \sqrt{\frac{1}{(k\sqrt{L_{2P}L_{2S}} + \frac{L_1 L_3}{L_1 + L_3})C_2}} = \sqrt{\frac{1}{(M + L_P)C_2}}. \tag{4.9}$$

By choosing a proper structure for the transformer, adjusting the self-inductance values of the two winding inductors, and optimizing the magnetic coupling coefficient k on a given periphery of the feedback path, the proposed transformer feedback dual-band

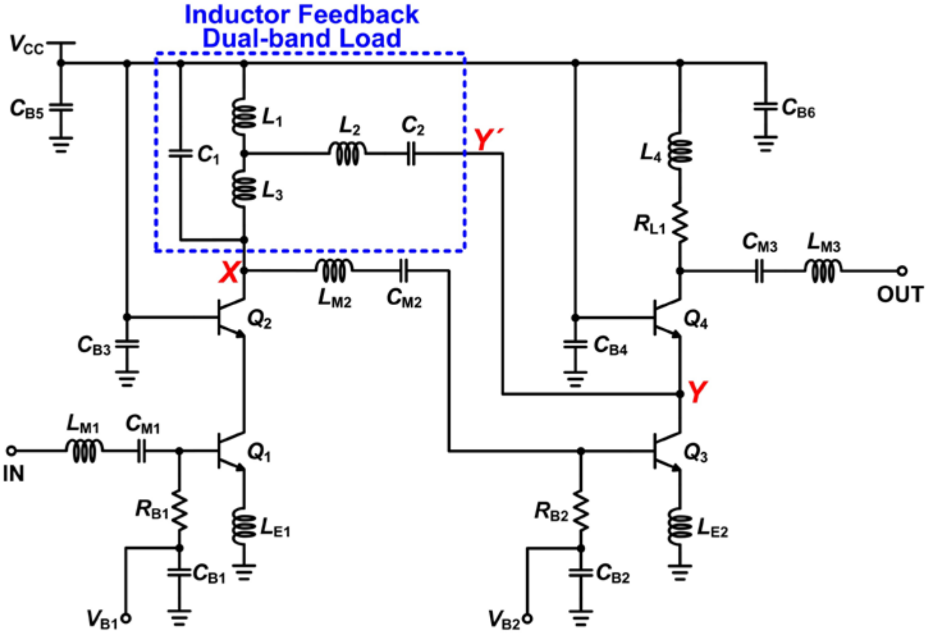

Fig. 4.3 Schematic of the concurrent dual-band LNA employing the inductor feedback dual-band load shown in Fig. 4.1(c).

load can provide more flexibility to control the effective Q-factor of the stopband notch inductance ($M + L_P$) as well as the coupling strength affecting the delivery of the feedback passband signals and feedforward stopband signal, which would improve the performance of dual-band LNAs.

4.2 Concurrent Dual-band Low-Noise Amplifiers

In this section, two concurrent dual-band LNAs employing the proposed inductor and transformer feedback dual-band loads are proposed as shown in Fig. 4.1(c) and Fig. 4.2(b), respectively. Figs. 4.3 and 4.4 show the schematics of the concurrent dual-band LNAs employing the inductor and transformer feedback dual-band loads, respectively. These concurrent dual-band LNAs were designed with the TowerJazz’s 0.18-μm

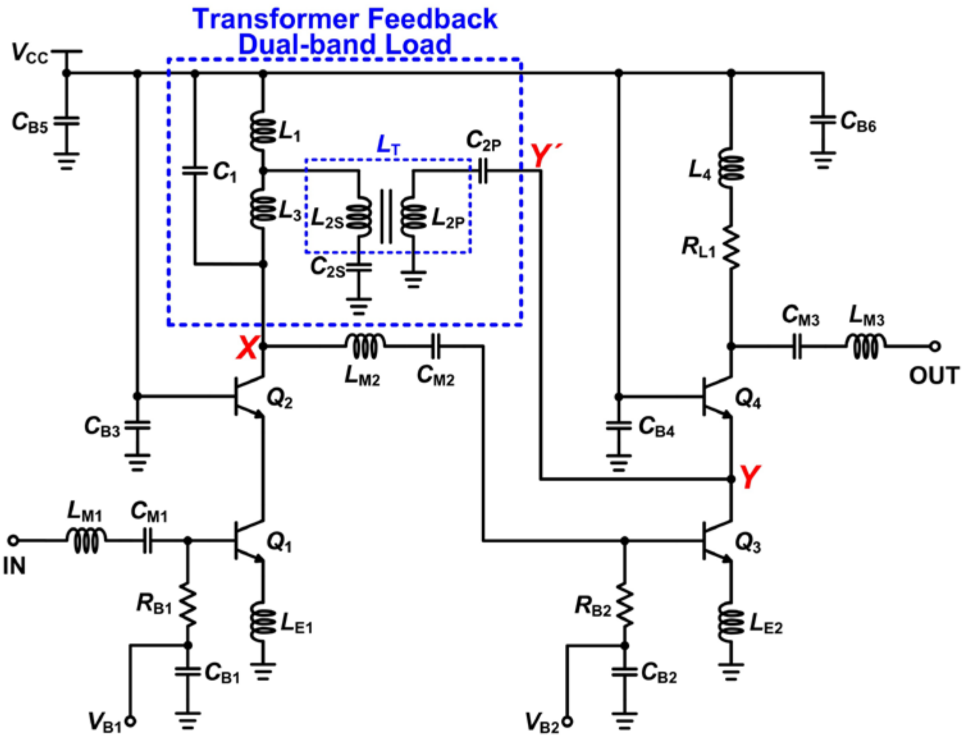

Fig. 4.4 Schematic of the concurrent dual-band LNA employing the transformer feedback dual-band load shown in Fig. 4.2(b).

BiCMOS process having f_T/f_{max} of 240/280 GHz [24] and aimed for various *K*-/*Ka*-band applications.

4.2.1 Design of Dual-band LNAs Employing Proposed Feedback Dual-band Loads

The concurrent dual-band LNAs are based on the same platform and have the same component values except those of the embedded feedback dual-band loads. A two-stage cascode topology was used to increase the power gain and the reverse isolation of the LNAs. Table 4.1 summarizes the passive component values used in the concurrent dual-band LNAs. It should be noted that the inductances shown in Table 4.1 are

TABLE 4.1
Component Values of Concurrent Dual-band LNAs

<table>
<tr><th>Component</th><th>LNA with Inductor</th><th>LNA with Transformer</th><th>Component</th><th>LNA with Inductor</th><th>LNA with Transformer</th></tr>
<tr><td>L_{M1}</td><td colspan="2">250 pH</td><td>C_{M1}</td><td colspan="2">1.585 pF</td></tr>
<tr><td>L_{M2}</td><td colspan="2">170 pH</td><td>C_{M2}</td><td>200.6 fF</td><td>104.1 fF</td></tr>
<tr><td>L_{M3}</td><td colspan="2">290 pH</td><td>C_{M3}</td><td colspan="2">143.2 fF</td></tr>
<tr><td>L_1</td><td>30 pH</td><td>50 pH</td><td>C_1</td><td>106.8 fF</td><td>43.1 fF</td></tr>
<tr><td rowspan="2">L_2</td><td rowspan="2">200 pH</td><td>132 pH (L_{2P})</td><td rowspan="2">C_2</td><td rowspan="2">192 fF</td><td>260.6 fF (C_{2P})</td></tr>
<tr><td>141 pH (L_{2S})</td><td>13.1 pF (C_{2S})</td></tr>
<tr><td>L_3</td><td>90 pH</td><td>100 pH</td><td>$C_{B1,2}$</td><td colspan="2">9.87 pF</td></tr>
<tr><td>L_4</td><td colspan="2">200 pH</td><td>$C_{B3,4}$</td><td colspan="2">11.8 pF</td></tr>
<tr><td>L_{E1}</td><td colspan="2">30 pH</td><td>R_{L1}</td><td colspan="2">21.7 Ohm</td></tr>
<tr><td>L_{E2}</td><td colspan="2">40 pH</td><td>$R_{B1,2}$</td><td colspan="2">2 kOhm</td></tr>
</table>

approximate values extracted from the 3D EM simulation results of IE3D [17], and they might be different with the schematic level inductor values.

The concurrent dual-band LNA in Fig. 4.3 employs the inductor feedback dual-band load between the first-stage's output node *X* and the second-stage's node *Y*. The concurrent dual-band LNA shown in Fig. 4.4 uses the transformer feedback dual-band load with a DC block capacitor (C_{2S}) added in series to the secondary winding inductor (L_{2S}) of the transformer. The transistor Q_3 of the second-stage common-emitter amplifier acts as an inverting amplifier seen in Figs. 4.1(c) and 4.2(b). All transistors ($Q_{1\text{-}4}$) have an identical size composed of a one-finger emitter having 0.13-μm width and 10.16-μm length, and two-finger base and collector.

A wideband matching technique [18] covering the entire dual passbands is used at both the input and output of the concurrent dual-band LNAs. This wideband matching

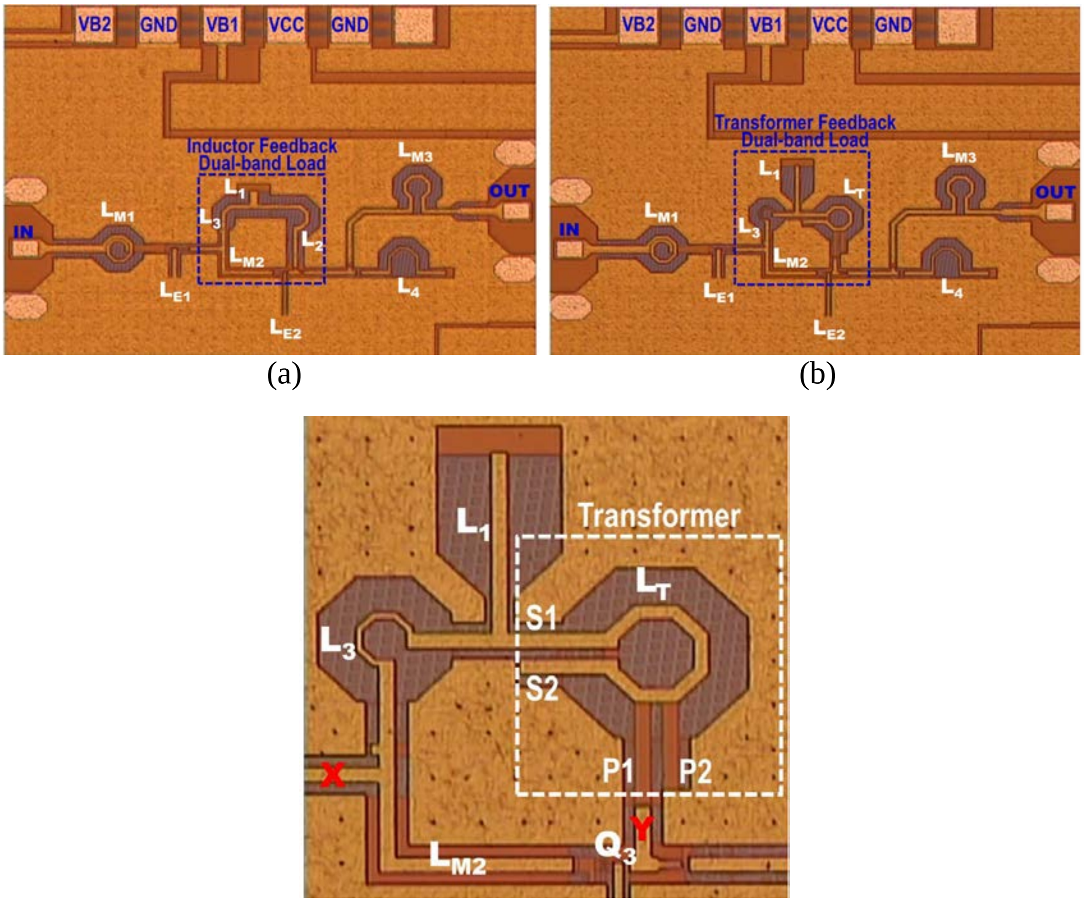

(a)

(b)

(c)

Fig. 4.5 Micrographs of the fabricated concurrent dual-band LNAs: (a) with the inductor feedback dual-band load, (b) with the transformer feedback dual-band load, and (c) zoom-in area of the transformer feedback dual-band load employed in (b).

at the LNA input requires less number of matching inductors as compared to the other dual-band LNAs in [5], [6], and [7], which employ dual-band input matching techniques for each passband, thereby resulting in smaller layout area as well as better NF performance due to lower routing metal resistances of inductors. The (small) inductances and parasitic capacitances of the input and output pads were taken account into the design of the matching networks. The emitter degeneration inductors (L_{E1}, L_{E2}) and the second-stage load resistor (R_{L1}) are used to provide good stability and matching performances over the desired passbands.

Figure 4.5 shows the photographs of the fabricated concurrent dual-band LNAs dies and the zoom-in area of the transformer feedback dual-band load. These LNAs occupy an identical area of 1.5 mm × 0.93 mm including pads, but the LNA core area is only 1.02 mm × 0.47 mm.

As every node-to-node interconnection line could behave as an inductor, transmission line, or a combination of these depending on its physical configuration, it is important to use proper types of interconnections for the actual layout of LNAs operating at high microwave (> 10 GHz) and millimeter-wave frequencies. To establish a firm ground plane as well as to provide small undesired (for interconnection) or desired inductances at the same time, the designed concurrent dual-band LNAs use two types of transmission lines – coplanar waveguide (CPW) and grounded coplanar waveguide (GCPW) [25]. For example, the matching inductors L_{M1}, L_{M3}, and $L_{1\text{-}4}$, are designed with hybrid inductor structures combining CPW and spiral inductors together. The emitter degeneration inductors L_{E1} and L_{E2} are designed with a CPW structure only to ensure small inductance values with concrete ground return paths. The interstage matching inductor L_{M2} is solely designed with a GCPW structure in order to provide a better ground plane for the isolated land enclosed by the feedback dual-band loads as seen in Fig. 4.5(c).

The L-shape transformer L_T seen in Fig. 4.5(c) is designed with a stacked metal structure using the two top-most metals M_6 and M_5. The parasitic capacitance at the first-stage's output node *X* causes more detrimental effect on the LNA gain degradation than that at the second-stage's node *Y*. Thus, the top metal M_6 is used for the secondary inductor (S1–S2) to minimize the parasitic capacitance at node *X*, while the metal M_5 is used for the primary inductor (P1–P2) connected to node *Y* seen in Fig. 4.5(c). The DC block capacitor C_{2S} is chosen to be much larger than C_{2P} so that not to create an undesired notch response within the desired passbands by the L_{2S}–C_{2S} pair in the secondary signal path. The notch response of more than 10 dB occurs at around 3.5 GHz by the L_{2S}–C_{2S} pair. Extensive EM simulations were carried out thoroughly for the inductors, from each inductor unit to the whole feedback dual-band load structure including the load inductors (L_1, L_3), the feedback transformer (L_T) and the inter-stage matching inductor (L_{M2}). The simulated performance of the designed feedback transformer is obtained with the magnetic coupling coefficient k of 0.42, the Q-factors of 15.7/16 and the self-inductance values of 141/132 pH for the primary/secondary inductors, respectively, at 30 GHz.

4.2.2 Enhancement of Stopband Rejection Performance

Recalling from the operation principle of the feedback dual-band loads explained in Section 4.1, the concurrent dual-band LNAs shown in Figs. 4.3 and 4.4 operate based on both the negative feedback loop of the passband signals as well as the feedforwarded and inverted stopband signal cancellation at node *Y*. The two passband signals see the high impedance load at node *X* and are delivered to the inverting amplifier together with a small amount of the stopband signal. However, since most of the stopband signal

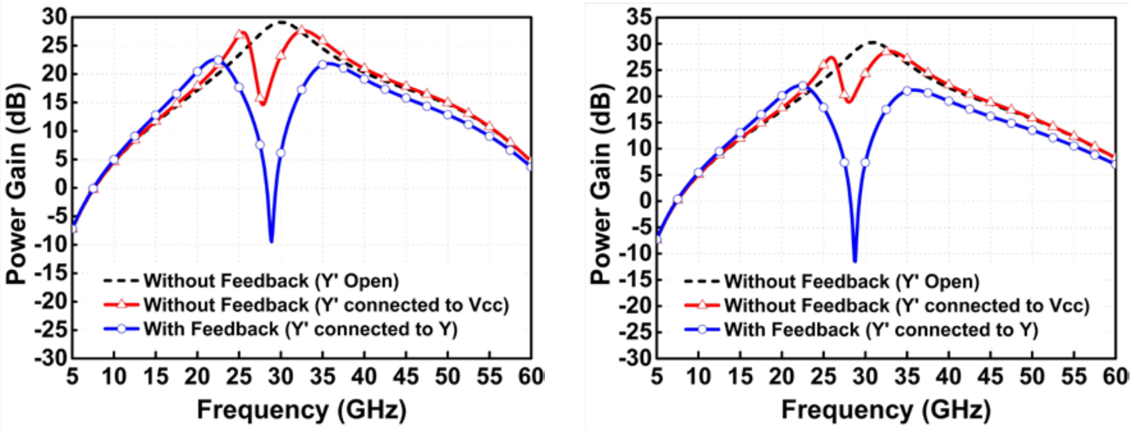

(a) (b)

Fig. 4.6 Power gain (S_{21}) simulation results of the concurrent dual-band LNAs having the inductor (a) and transformer (b) feedback dual-band loads with and without feedback.

experiences a low impedance load at node *X*, it flows into the embedded dual-band load and feedforwards to node *Y*. Most of feedforwarded and few of the inverted stopband signals are out-of-phase at node *Y*, hence cancelling out. Therefore, the concurrent dual-band LNAs achieve a clear concurrent dual-band response as well as high stopband rejection performance by compensating for the low Q-factor of the integrated inductors.

The creation of distinguishable passbands and stopband with high SRR can be examined with the power gain responses (S_{21}) of the concurrent dual-band LNAs with and without the feedback loop connection. From Figs. 4.3 and 4.4, by disconnecting node *Y′* from node *Y* of the second-stage and connecting *Y′* to the power supply node V_{CC}, the embedded inductor and transformer feedback dual-band loads are transformed to the modified dual-band loads shown in Figs. 4.1(b) and 4.2(a), respectively. On the other hand, when node *Y′* is disconnected from Y and left open, the embedded feedback dual-band loads can be seen as a simple wideband (or tuned) load composed of L_1, L_3

TABLE 4.2
SIMULATED PERFORMANCE SUMMARY OF DUAL-BAND LNAS WITH AND WITHOUT FEEDBACK

LNA	Without Feedback			With Feedback			Unit
	S_{21} at f_{P1}^{a}/f_{P2}^{b}	S_{21} at f_S^{c}	SRR	S_{21} at f_{P1}/f_{P2}	S_{21} at f_S	SRR	
With Inductor	27.3	14.6	12.7	22.5	−9.5	32.0	dB
	27.6		13.0	21.8		31.3	dB
With Transformer	27.4	18.8	8.6	22.0	−12.0	34.0	dB
	28.7		9.9	21.2		33.2	dB

[a-c] f_{P1}, f_{P2}, and f_S represent the respective low- and high-passband, and stopband frequencies exhibiting maximum passband gain and stopband loss.

and C_1, which resonates at around 30 GHz. Fig. 4.6 verifies the advantage and usefulness of the proposed feedback dual-band loads through comparisons of the simulated power gain responses of both LNAs with and without the feedback loop connection. Table 4.2 summarizes the simulation results. For simulations, the concurrent dual-band LNAs without the feedback loop connection keep the same EM simulated component values as those in the counterparts with the closed feedback loop, but only node Y' is ideally rerouted to the power supply node V_{CC} by opening the feedback loop Y–Y'. The proposed concurrent dual-band LNAs have been designed to achieve $S_{21} > 20$ dB with passband gain imbalance < 1 dB and SRR > 30 dB for this verification.

From Fig. 4.6 and Table 4.2, it is clearly seen that, as compared to the concurrent dual-band LNAs without feedback loop connection, those employing the feedback dual-band loads can achieve excellent SRRs, which are improved by 19.3/18.3 dB and 25.4/23.3 dB for the concurrent dual-band LNAs with the feedback inductor and transformer at low/high passbands (f_{P1}/f_{P2}), respectively. Furthermore, these LNAs can achieve much higher SRRs by adjusting the bias current of the second-stage's inverting amplifier as described in the following section.

4.2.3 Control of Stopband Rejection and Gain Balance

The proposed inductor and transformer feedback dual-band loads include an inverting amplifier in their closed loop configuration as shown in Fig. 4.1(c) and Fig. 4.2(b). The second-stage's transistors (Q_3) with a common-emitter (CE) topology of the concurrent dual-band LNAs shown in Figs. 4.3 and 4.4 act as the inverting amplifier. For simplicity, we assume that the interstage matching inductor (L_{M2}) and capacitor (C_{M2}) and the small degeneration inductor (L_{E2}) can be absorbed into the inverting amplifier. Adjusting the bias current of the second-stage amplifier in the complete dual-band LNAs provides fine tuning capability of both the passband power gain responses and the stopband rejection performance at the same time. This bias tuning technique can be effectively used to optimize the stopband notch depth by compensating for possible changes of the Q-factor of the feedback *LC* notch filter due to various design factors, notably the inevitable process variation. This is useful for finding the optimum bias points of the dual-band LNAs to achieve not only low gain imbalance between the passbands, but also high SRR at the stopband.

Figures 4.7(a) and 4.8(a) show the simulated S_{21} results of the LNAs as a function of V_{BE2}. As V_{BE2} is increased from 0.83 V to 0.94 V, (corresponding to increase of the base current I_{B2} from 2.07 μA to 15.52 μA, which results in increase of the collect current I_{C2} from 2.54 mA to 14.92 mA), the passband gains of both LNAs become

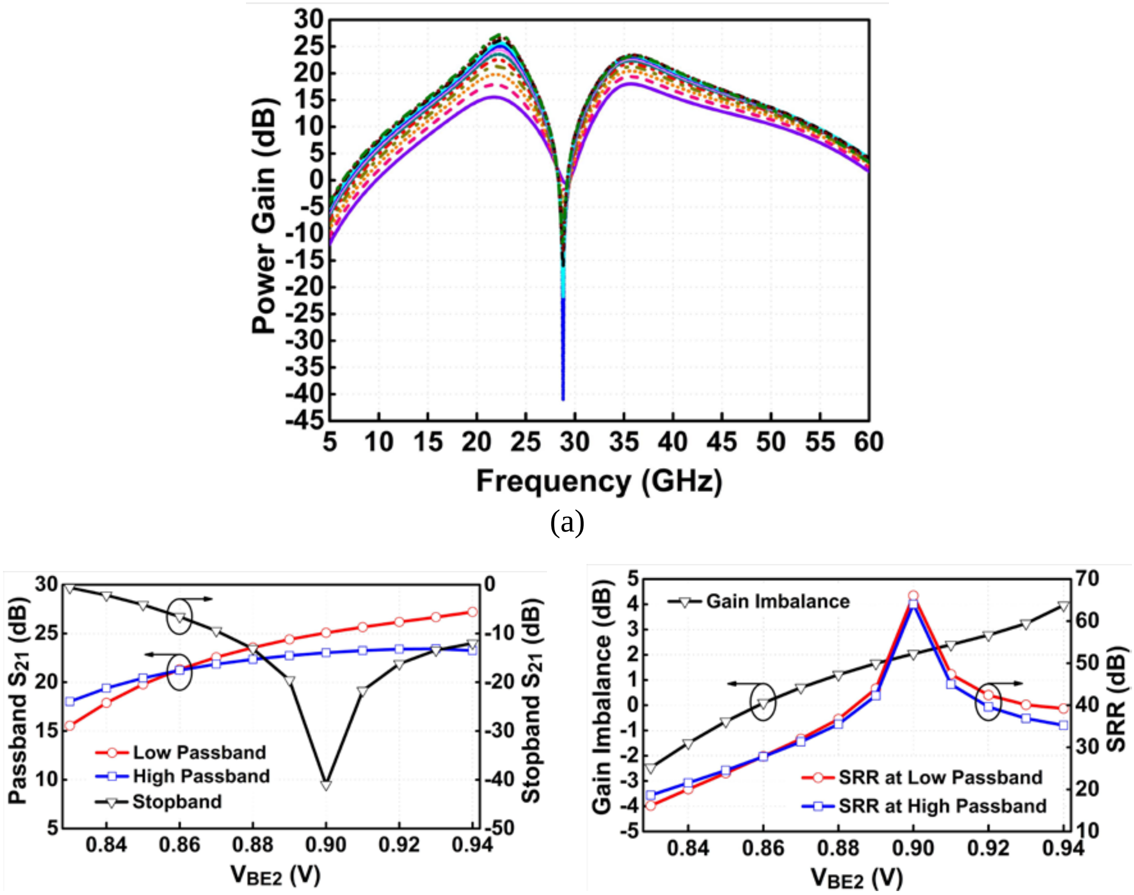

(a)

(b) (c)

Fig. 4.7 (a) Power gain (S_{21}) simulation results of the concurrent dual-band LNA with feedback inductor load for different V_{BE2} from 0.83 V to 0.94 V, (b) passband peak S_{21} and stopband minimum S_{21}, and (c) passband gain imbalance and SRR.

higher. However, the deep stopband notch responses only occur at certain bias points as shown in Figs. 4.7(b) and 4.8(b). These deep notches in the stopband happen when the feedforwarded stopband signal through the notch filter and the inverted stopband signal by the second-stage's inverting amplifier are exactly out-of-phase at node *Y*. The deepest stopband notch responses of −41/−39.3 dB are obtained with V_{BE2} of 0.9/0.886 V for the

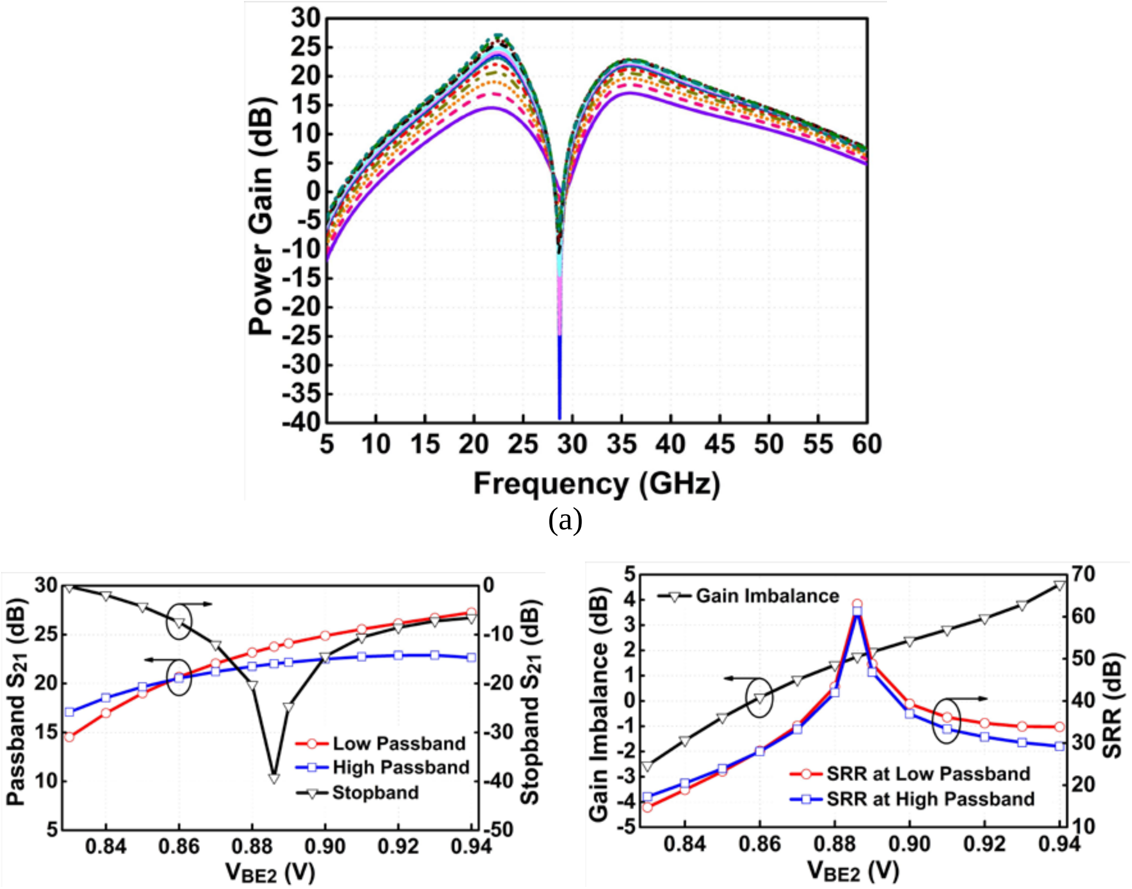

(a)

(b)

(c)

Fig. 4.8 (a) Power gain (S_{21}) simulation results of the concurrent dual-band LNA with feedback transformer load for different V_{BE2} from 0.83 V to 0.94 V, (b) passband peak S_{21} and stopband minimum S_{21}, and (c) passband gain imbalance and SRR.

dual-band LNA with feedback inductor/transformer, respectively. The passband signals exhibit higher gain responses as the V_{BE2} is increased and they experience no detrimental effect from the stopband signal cancellation.

The gain imbalance and SRR performances calculated from the S_{21} responses of the concurrent dual-band LNAs are shown in Figs. 4.7(c) and 4.8(c), respectively. The gain imbalance is calculated from the difference between the peak gains in the low- and high-passband. The SRR measures the difference between the peak gain in one passband and the highest rejection at the notch frequency of the stopband. When the V_{BE2} of larger than 0.87 V is applied, which corresponds to I_{B2} of 5.31 μA and I_{C2} of 6.07 mA, both the LNAs achieve the SRRs higher than 30 dB. The SRRs higher than 20 dB can be obtained when V_{BE2} larger than 0.84 V is applied. It is also found that there are certain V_{BE2} windows of around 30 mV (0.845-to-0.875 V) over which gain imbalance lower than 1 dB is achieved for both LNAs. Therefore, the concurrent dual-band LNAs can provide great flexibility in finding optimum bias operating points to achieve both low gain imbalance and high SRR performances by compromising the LNA specifications such as power gain and linearity. The substantial SRR improvement of the designed dual-band LNAs validates the unique characteristics and effectiveness of the proposed feedback dual-band loads.

4.3 Experimental and Simulated Results

The concurrent dual-band LNAs were measured on-wafer. For both LNAs, a 1.8-V power supply voltage (V_{CC}) was used, and the first-stage bias voltage (V_{BE1}) was fixed at 0.9 V, which drew around 9.5 mA. Then, the second-stage bias (V_{BE2}) was tuned to find optimum operating points for either a high gain with minimum gain imbalance (high gain mode) or a largest SRR (high SRR mode). Figs. 4.9 and 4.10 show the measured S_{21}, gain imbalance, and SRR of the concurrent dual-band LNAs as a function of V_{BE2}.

Comparing the simulated and measured results of these LNAs in Figs. 4.7 and 4.9 and 4.8 and 4.10, it is found that the measured optimum V_{BE2} bias points for the

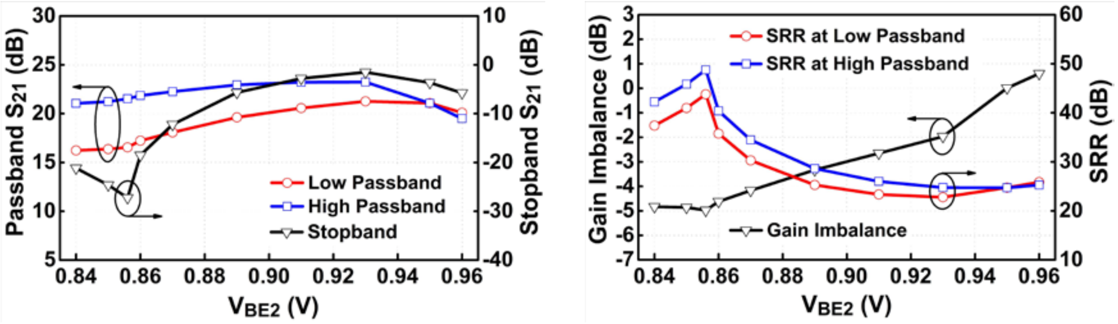

(a) (b)

Fig. 4.9 (a) Measured S_{21} of the concurrent dual-band LNA with feedback inductor load in passbands and stopband. (b) Measured gain imbalance and SRR obtained from (a).

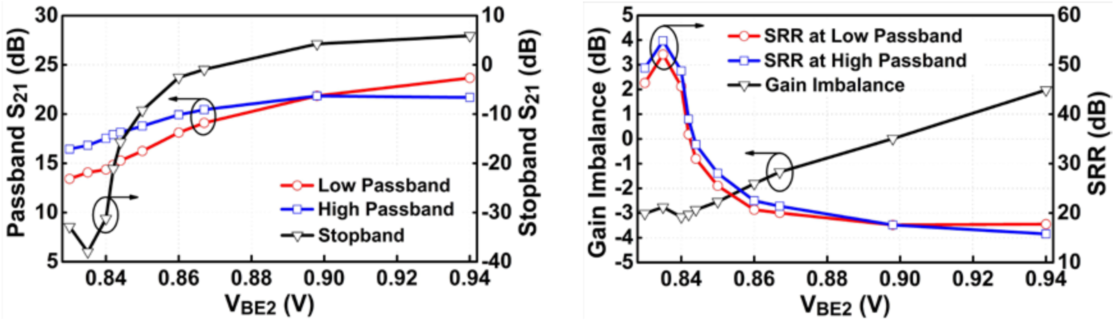

(a) (b)

Fig. 4.10 (a) Measured S_{21} of the concurrent dual-band LNA with feedback transformer load in passbands and stopband. (b) Measured gain imbalance and SRR obtained from (a).

largest SRRs occur at lower bias levels (0.846/0.832 V for the dual-band LNA with feedback inductor/transformer) with slightly higher gain imbalances than the simulated ones (0.9/0.886 V). These discrepancies mainly originated from the process variation of the capacitor C_2, which slightly changes the stopband notch frequency as well as the effective Q-factor of the passive *LC* notch filters. It should be noted that this process variation is usual for most amplifiers using integrated capacitors. Nevertheless, the

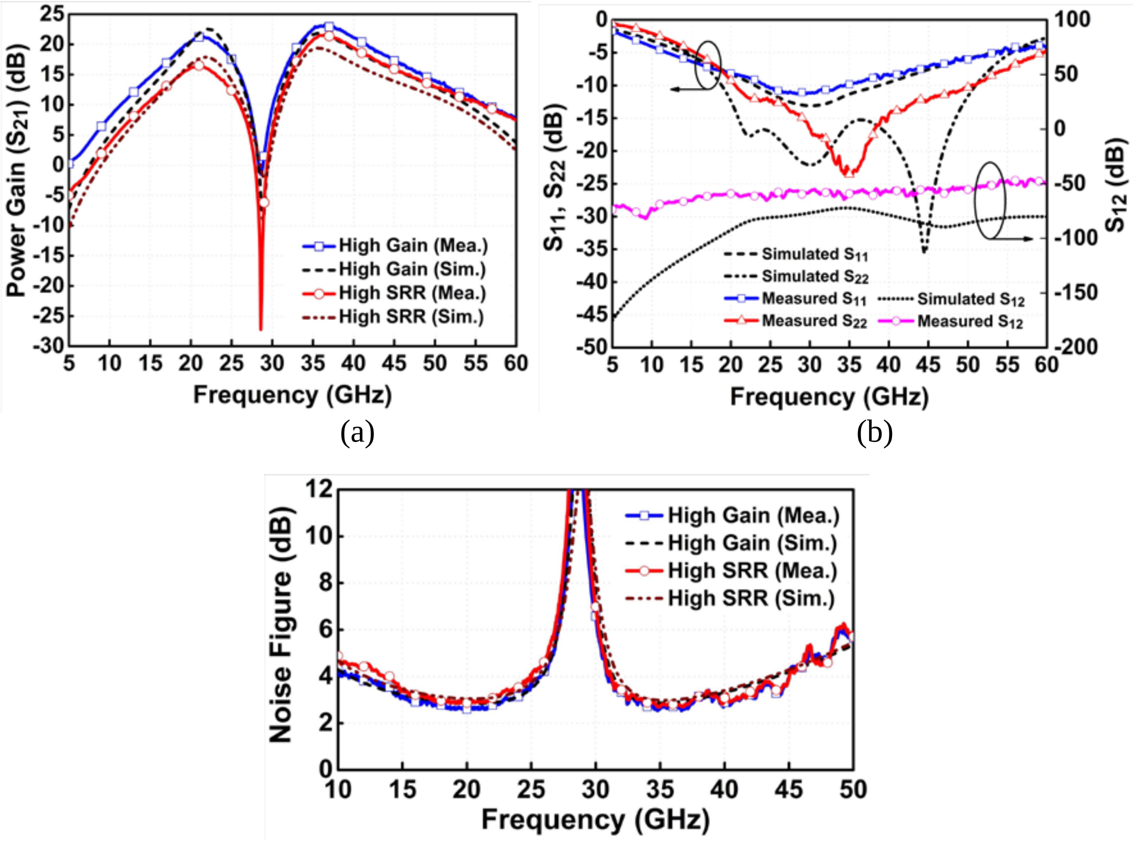

(a) (b)

(c)

Fig. 4.11 Measured and simulated results of the concurrent dual-band LNA with feedback inductor load in high gain and SRR modes: (a) power gain, (b) S_{11}, S_{22}, and S_{12}, and (c) NF.

developed concurrent dual-band LNAs employing the proposed feedback dual-band loads can overcome the effective Q-factor change of the passive notch filter by controlling the V_{BE2} of the second-stage's inverting amplifier, and thus they can provide high stopband rejection over the process variation as compared to conventional dual-band LNAs, which is a significant and useful feature in practice.

Figures 4.11 and 4.12 compare the simulated and measured results of the concurrent dual-band LNAs in both high gain and high SRR operation modes. As shown

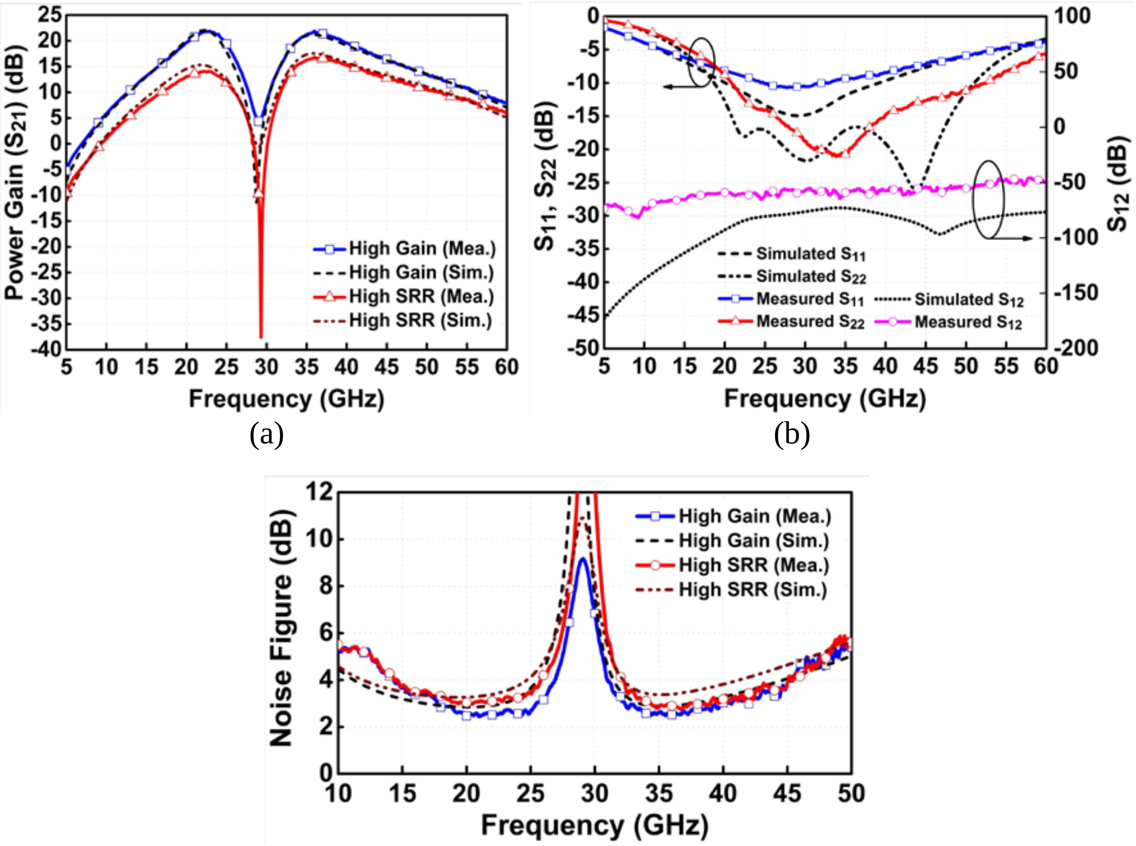

(a) (b)

(c)

Fig. 4.12 Measured and simulated results of the concurrent dual-band LNA with feedback transformer load in high gain and SRR modes: (a) power gain, (b) S_{11}, S_{22}, and S_{12}, and (c) NF.

in Fig. 4.11, the concurrent dual-band LNA with feedback inductor load in high gain mode achieves peak gains of 21.3/23.2 dB at 21.5/36.5 GHz, respectively. The measured 3-dB bandwidths of the low and high pass-bands are 6.6 GHz (18–24.6 GHz) and 8 GHz (33.4–41.4 GHz), respectively. The measured best NFs are 2.6/2.5 dB in the respective low/high passband. The measured IP_{1dB} and IIP_3 in the low/high passband are −23.4/−24 dBm and −15.3/−17.1 dBm, respectively. The concurrent dual-band LNA with feedback inductor load achieves the best SRRs of 43.9/48.8 dB with low/high passband gains of 16.6/21.5 dB, respectively.

The concurrent dual-band LNA with feedback transformer load in high gain mode exhibits almost identical passband gains of 21.8 dB at 23/36 GHz with the gain imbalance of less than 0.1 dB as seen in Fig. 4.12. This LNA achieves measured 3-dB bandwidths of 6 GHz (19.3–25.3 GHz)/8.2 GHz (33.1–41.3 GHz) and best NFs of 2.4/2.5 dB in the low/high passband, respectively. The IP_{1dB} of −26.2/−25.6 dBm and IIP_3 of −16.2/−16.4 dBm were measured in the respective low/high passband. In high SRR mode, the LNA achieves the best SRRs of 51.7/54.4 dB with low/high passband gains of 14.1/16.8 dB, respectively. It has also been confirmed that these LNAs are unconditionally stable for all operation modes.

Table 4.3 summarizes and compares the performances of concurrent multiband LNAs operating at similar frequencies above 10 GHz. Both the developed concurrent dual-band LNAs show the best NF and gain imbalance performances. To the best of the authors' knowledge, the concurrent dual-band LNA employing the proposed transformer feedback dual-band load also achieves the best SRRs with the lowest gain imbalance among the reported concurrent multiband LNAs including those operate below 10 GHz.

4.4 Summary and Conclusion

The inductor and transformer feedback dual-band loads have been proposed to overcome the low Q-factor of integrated inductors commonly encountered in concurrent multiband LNAs. Two concurrent dual-band LNAs using the proposed feedback dual-

TABLE 4.3
PERFORMANCE SUMMARY AND COMPARISON OF CONCURRENT MULTIBAND LNAs

Reference	Technology	Frequency (GHz)	Gain (dB)	NF (dB)	IIP$_3$ (dBm)	S$_{11}$ (dB)	Passband Gain Imbalance (dB)	Stopband Rejection Ratio[b] (dB)	Power (mW)	Area (mm^2)
[10]	0.18-μm CMOS	18	9.2	5.7	–2	–23	2.8	6.2	8	0.33
		24.5	12	6.4	–3	–24		9		
[11]	0.13-μm CMOS	10	25.3	5.3	N/A	–24.4	13.2	54	12	1.14
		24	12.1	10.4	N/A	–17.9		40.8		
[21]	0.18-μm SiGe BiCMOS	23.5	21.9	5.1	–10.4	–28	5.3	24	36	0.19
		35.7	16.6	7.2	–8.3	–14		18.7		
[23]	0.18-μm SiGe BiCMOS	13.5	22.4	3.4	–13.5	–9.5	3.5	41	36	0.59
		24	23.7	3.2	–17.1	–14.5		N/A		
		35	20.2	3.7	–16.1	–10.1		30		
This Work (LNA with Feedback Inductor)	**0.18-μm SiGe BiCMOS**	**21.5**	**21.3 (16.6)**[a]	**2.6 (2.9)**	**–15.3**	**–8.5**	**1.9 (4.9)**	**22.8 (43.9)**	**41.4 (23.4)**	**0.48**
		36.5	**23.2 (21.5)**	**2.5 (2.7)**	**–17.1**	**–9.6**		**24.7 (48.8)**		
This Work (LNA with Feedback Transformer)	**0.18-μm SiGe BiCMOS**	**23**	**21.8 (14.1)**	**2.4 (3.0)**	**–16.2**	**–9.2**	**<0.1 (2.7)**	**17.5 (51.7)**	**34.2 (22.5)**	**0.48**
		36	**21.8 (16.8)**	**2.5 (2.8)**	**–16.4**	**–9.4**		**17.5 (54.4)**		

[a] The values shown inside ( ) are measured results with the high SRR mode operation.
[b] Difference between the maximum gain at each passband and stopband loss.

band loads have been successfully developed for various *K*-/*Ka*-band applications. The developed concurrent dual-band LNAs achieve superior stopband rejection and gain balance performances over possible design variations including process variation by controlling the bias levels of their second-stage's inverting amplifier, which is attractive for practical implementations in actual RF systems. The concurrent dual-band LNA employing the transformer feedback dual-band load provides more flexibility for the creation of the stopband and passbands by optimizing the transformer design on a given feedback geometry. These dual-band LNAs achieve unprecedented NF and gain balance performances. Moreover, the concurrent dual-band LNA with the transformer feedback dual-band load achieves the highest SRR among the reported concurrent multiband LNAs. The proposed dual-band loads and corresponding concurrent dual-band LNAs could be extended for multiband design not only for amplifiers but also for other components.

CHAPTER V

CONCURRENT DUAL-BAND SINGLE-TO-DIFFERENTIAL LOW-NOISE AMPLIFIER*

Single-input to differential-output (single-to-differential) conversion circuits, such as passive and active baluns, 180-deg hybrid couplers, transformers, etc., have been widely used in many RF communication and radar systems. These single-to-differential circuits can be placed right after an LNA in RF receiver front-ends to convert a received single-ended RF signal into a pair of differential signals as desired. Single-to-differential LNAs can also be used in RF receiver front-ends in lieu of separate LNAs and baluns, effectively making low-noise amplified or active baluns. Many single-to-differential LNAs and active baluns operating above 20 GHz have been reported in single narrow [26]–[31] and broad [32]–[38] bands. Since most broadband single-to-differential LNAs and active baluns provide lower gain or even loss, they have higher noise figure (NF) as compared to those designed for narrow bands. They also occupy larger die area than their narrow-band counterparts. Therefore, for narrow-band applications, narrow-band single-to-differential LNAs and active baluns are more desirable than those designed for broadband operations due to their advantages of higher gain, lower NF, and smaller size.

Next-generation wireless communication, sensing, and radar systems are aimed for operating frequencies in the higher microwave (> 20 GHz) or millimeter-wave

---

*© 2015 IEEE. Reprinted, with permission, from J. Lee and C. Nguyen, “A novel concurrent dual-band single-to-differential low-noise amplifier architecture implementing transformer feedback and its design in K- and Ka-band on a 0.18-µm SiGe BiCMOS,” submitted to *IEEE Transaction on Microwave Theory and Techniques*, Aug. 2015.

regions. Furthermore, multiband multi-standard wireless communication, sensing and radar systems designed to operate over multiple frequency bands simultaneously in the high microwave or millimeter-wave regimes are also desired to increase data rates as well as to accommodate various applications combining multiple standards together. To support the development of those microwave and millimeter-wave multiband wireless communication, sensing and radar systems, several concurrent multiband single-end integrated circuits, such as LNAs [11], [21]–[23], [39] and power amplifiers [25], [40], have been developed. Moreover, there have been just two switching (or reconfigurable) dual-band balun-LNAs with only simulated results reported for applications below 10 GHz [41], [42]. To date, no concurrent multiband single-to-differential amplifiers have been reported above 10 GHz despite of their essential role in multiband RF systems at these frequencies. Development of such amplifiers is therefore essential, especially those operating in the high microwave and millimeter-wave regions and those designed to maintain the advantages of high gain, low NF, and small size of narrow single-band single-to-differential LNAs as mentioned earlier over multiple bands.

In this chapter, the first true concurrent dual-band single-to-differential LNA and its design on 0.18-μm BiCMOS for various *K*-/*Ka*-band applications are presented. The designed dual-band single-to-differential LNA converts two simultaneous independent single-ended input signals at around 22 and 36 GHz into 180° out-of-phase differential signals at its output without any switching activity. The LNA especially employs a new transformer feedback dual-band load in order to provide high gain and low NF in the two passbands as well as to produce a high attenuation in the stopband (around 29 GHz) placed between the passbands. A detailed operating principle of the new transformer feedback dual-band load is analyzed first, and the design and measurement results of the developed dual-band single-to-differential LNA are then presented.

5.1 Review of Single-ended Feedback Multiband Loads

Concurrent dual-band LNAs simultaneously receive and amplify signals in two passbands, and then deliver them to the following stages without any switching mechanism. At the same time, they also create a notch in the stopband to attenuate the undesired interference, image, or blocker signals. The conventional dual-band resonator reported in [5] and [21] can be used as a passive dual-band load at the output of an amplifier to create a concurrent dual-band response by combining the wideband response and the notch response of two *LC* pairs. Since the stopband rejection performance of most concurrent dual-band amplifiers using the conventional passive dual-band load is mainly determined by the Q-factor of the constituent integrated notch inductor, the notch inductor should be designed to have a high Q-factor at the stopband frequency (e.g. Q > 30 for SRR > 20 dB) as seen in Ch. II [23]. However, the design of high-Q integrated inductors at millimeter-wave frequencies is challenging due to unavoidable parasitic components. In order to compensate the low Q-factor of integrated notch inductors and provide high stopband rejection performance, the inductor feedback tri-band load was developed in [22] and [23], which was described in Ch. II. The reported concurrent tri-band LNA employing the feedback tri-band load [23] achieved high SRRs of more than 30 dB as seen in Ch. III.

In order to provide more degrees of freedom in the design of the notch inductor as well as to effectively use its physical layout area in the given feedback path, the passive transformer-based feedback dual-band load was developed as presented in Ch. IV. The reported transformer feedback dual-band load provides more flexibility in the design of an integrated notch inductor as well as high stopband rejection performance by adjusting the self-inductance values of the two winding inductors and optimizing the magnetic coupling coefficient k on a given periphery of the feedback path. The transformer feedback dual-band load additionally provides the stopband rejection control capability to maintain high SRR over undesired process variation. The concurrent dual-band LNA using the transformer feedback dual-band load in Ch. IV exhibited more than 50-dB SRR.

Although the reported concurrent multi-band loads using feedback inductors and transformers can achieve good stopband rejection performance, they are only suitable for single-input to single-output (single-ended) amplifiers. In the following section, we will present a novel transformer feedback single-to-differential dual-band load suitable for concurrent dual-band single-to-differential LNAs.

5.2 Design of Single-to-Differential Transformer Feedback Dual-band Load

Figure 5.1(a) shows a simplified equivalent circuit of the proposed single-to-differential transformer feedback dual-band load. It is created based on the transformer feedback single-ended dual-band load shown in Fig. 4.2. Each terminal of the primary winding inductor (L_{2P}) is connected to the differential output node Y–Y' of the single-to-

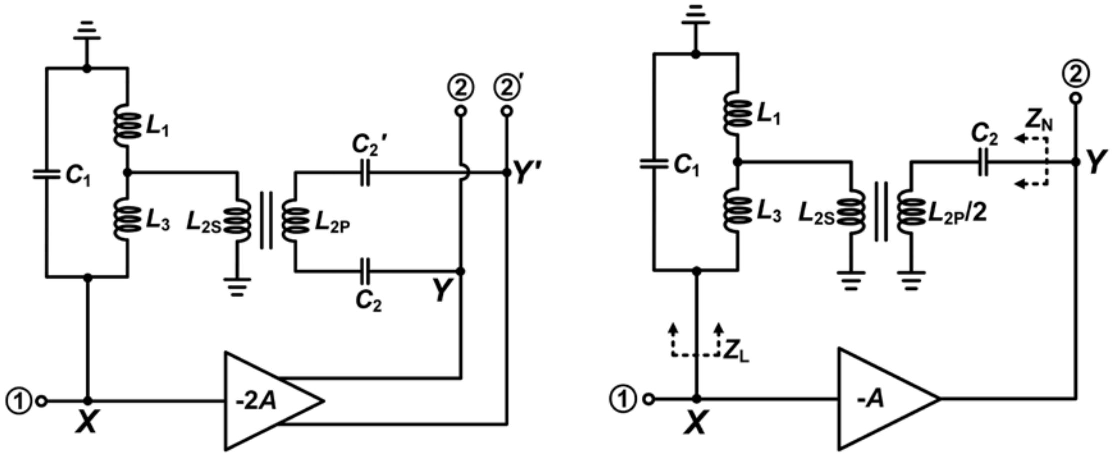

(a) (b)

Fig. 5.1 (a) Full equivalent circuit and (b) a half-circuit of the proposed single-input to differential-output transformer feedback dual-band load.

differential inverting amplifier (–2*A*) in series with the two notch capacitors (C_2, C_2'). The two capacitors used in the feedback notch filter are identical ($C_2' = C_2$). The stopband notch is mainly created by the combination of L_{2P}, C_2 and C_2', while the inverting amplifier, functioning as a second-stage amplifier of the proposed LNA (see Fig. 5.2) to be described in Section III, provides the single-to-differential signal conversion over the entire passbands

The operating principle of the proposed single-to-differential transformer feedback dual-band load can be described with a half-circuit as shown in Fig. 5.1(b). In the half-circuit, the gain of the single-to-differential inverting amplifier is changed from –2*A* to –*A* representing a single-ended inverting amplifier. Also, the primary inductance (L_{2P}) of the transformer is reduced by a half ($L_{2P}/2$) and only one capacitor is used for the analysis. Consequently, the proposed transformer feedback single-to-differential dual-band load can be converted into a single-ended dual-band load and analyzed similarly to that presented in Fig. 4.2(b).

The load impedance Z_L of the single-ended transformer feedback dual-band load in Fig. 5.1(b) seen at node X can be obtained as

$$\begin{aligned} Z_\mathrm{L}(s) &= \frac{N_\mathrm{L}(s)}{D_\mathrm{L}(s)} \\ &= \frac{s^3[(L_1+L_3)M'+L_1L_3]C_2 + s(L_1+L_3)}{\begin{bmatrix} s^4[(L_1+L_3)M'+L_1L_3]C_1C_2 + \\ s^2[(L_1+L_3)C_1+(L_1+M')C_2]+1 \end{bmatrix}} \end{aligned} \tag{5.1}$$

where, $M' = k\sqrt{\left(L_{2P}/2\right)L_{2S}}$. The feedback notch impedance Z_N seen at node Y can be written as

$$\begin{aligned} Z_\mathrm{N}(s) &= \frac{N_\mathrm{N}(s)}{D_\mathrm{N}(s)} \\ &= \frac{\begin{bmatrix} s^4[(L_1+L_3)M'+L_1L_3)C_1C_2 + \\ s^2[(L_1+L_3)C_1+(L_1+M')C_2]+1 \end{bmatrix}}{s^3(L_1+L_3)C_1C_2 + sC_2} \end{aligned} \tag{5.2}$$

From (5.1), the stopband and passband frequencies of the proposed transformer feedback single-to-differential dual-band load can be written as

$$\omega_{S,Z_L} = \sqrt{\frac{1}{(M'+L_P)C_2}} \tag{5.3}$$

and

$$\omega_{P1,2,Z_L} = \sqrt{\frac{\frac{L_1+M'}{L_1+L_3}\cdot\frac{C_2}{C_1}+1 \pm \sqrt{\left(\frac{L_1+M'}{L_1+L_3}\cdot\frac{C_2}{C_1}+1\right)^2 - 4\frac{C_2}{C_1}\cdot\frac{M'+L_P}{L_1+L_3}}}{2C_2\left(M'+L_P\right)}} \tag{5.4}$$

respectively, where $L_P=L_1L_3/(L_1+L_3)$. It is apparent from (5.3) and (5.4) that the proposed single-to-differential transformer feedback dual-band load in Fig. 5.1(a) can provide more flexibility in controlling the effective Q-factor of the stopband notch inductor ($M' + L_P$).

The operating principles of the proposed single-to-differential transformer feedback dual-band load can be explained by referring to Fig. 5.1 and the feedback tri-band and dual-band loads presented in Ch. II [23] and Ch. IV, respectively. In Fig. 5.1, at node X, most of the stopband signal at the frequency of $\omega_{S,ZL}$ given in (5.3) flows into the dual-band load and then feed-forwards to node Y due to a low impedance load at Y. On the other hand, the two passband signals experience a high impedance load at node X, so they travel through the inverting amplifier together with a small amount of the residual stopband signal reflected from the dual-band load. When the feedforwarded and the inverted stopband signals, after amplified by the gain of $-A$, have identical amplitude with 180° out-of-phase at node Y, they are cancelled out and an infinite notch occurs theoretically.

At node Y, since the numerator N_N of the notch impedance Z_N in (5.2) is equal to the denominator D_L in (5.1), the two zeros in (5.2) are exactly placed at the same location of the two poles in (5.1). Therefore, the passband signals see the low impedance Z_N through the transformer notch of the feedback path. This creates a dual-band notch filter at the passband frequencies at node Y and provides a negative feedback loop for the passband signals. Since the negative feedback passband signals and the cancellation of the feedforwarded and inverted stopband signals occur at the same time independently, the proposed single-to-differential transformer feedback dual-band load can create a clear concurrent dual-band response with high stopband rejection performance. Moreover, by varying the bias levels of the single-to-differential inverting amplifier, the proposed dual-band load provides an ability to control the stopband rejection performance as will be seen in Section 5.3.

5.3 Design of Concurrent Dual-band Single-to-Differential LNA

Figure 5.2 shows the schematic of the 22/36GHz concurrent dual-band single-to-differential LNA designed using the TowerJazz's 0.18-μm BiCMOS process [24]. The

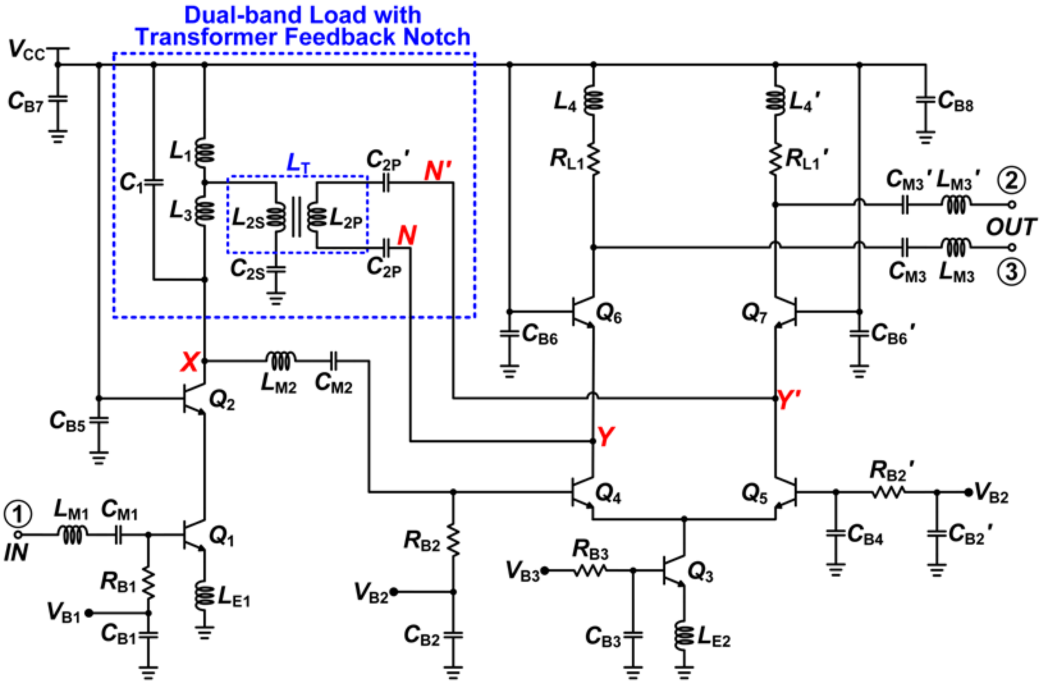

Fig. 5.2 Schematic of the concurrent dual-band single-input to differential-output LNA employing the transformer feedback dual-band load.

TABLE 5.1
COMPONENT VALUES OF CONCURRENT DUAL-BAND SINGLE-TO-DIFFERENTIAL LNA

<table>
<tr><th colspan="2">Component</th><th>Value</th><th>Component</th><th>Value</th></tr>
<tr><td colspan="2">L_{M1}</td><td>250 pH</td><td>C_{M1}</td><td>1.58 pF</td></tr>
<tr><td colspan="2">L_{M2}</td><td>170 pH</td><td>C_{M2}</td><td>86.2 fF</td></tr>
<tr><td colspan="2">L_{M3}, L_{M3}'</td><td>290 pH</td><td>C_{M3}, C_{M3}'</td><td>260.6 fF</td></tr>
<tr><td colspan="2">L_{1}</td><td>50 pH</td><td>C_{1}</td><td>43.7 fF</td></tr>
<tr><td rowspan="2">L_{T}</td><td>L_{2P}</td><td>150 pH</td><td>C_{2S}</td><td>4.94 pF</td></tr>
<tr><td>L_{2S}</td><td>146 pH</td><td>C_{2P}, C_{2P}'</td><td>577.2 fF</td></tr>
<tr><td colspan="2">L_{3}</td><td>100 pH</td><td>C_{B1}</td><td>9.87 pF</td></tr>
<tr><td colspan="2">L_{4}, L_{4}'</td><td>200 pH</td><td>$C_{\mathrm{B2,4}}$, C_{B2}'</td><td>4.94 pF</td></tr>
<tr><td colspan="2">L_{E1}</td><td>33.5 pH</td><td>C_{B3}</td><td>1.41 pF</td></tr>
<tr><td colspan="2">L_{E2}</td><td>30 pH</td><td>C_{B5}</td><td>10.97 pF</td></tr>
<tr><td colspan="2">R_{L1}, R_{L1}'</td><td>21.7 Ohm</td><td>$C_{\mathrm{B5,6}}$, C_{B6}'</td><td>6.04 pF</td></tr>
<tr><td colspan="2">$R_{\mathrm{B1,2,3}}$, R_{B2}'</td><td>2 kOhm</td><td>C_{B7} / C_{B8}</td><td>35.4 / 51.8 pF</td></tr>
</table>

transformer feedback dual-band load shown in Fig. 5.1(a) is placed between the first-stage load (node X) and the differential output node (Y–Y') of the single-to-differential inverting amplifier. The concurrent dual-band single-to-differential LNA receives two independent single-ended input signals in two separate passbands around 22 and 36 GHz, amplifies, and converts them into differential-output signals simultaneously, while attenuating undesired signals around 29 GHz. The values of the passive components used in the LNA are summarized in Table 5.1. All the inductors and interconnection lines are thoroughly modeled and extracted by using the HyperLynx 3D EM simulator (IE3D) [17].

The first stage of the concurrent dual-band single-to-differential LNA is designed using a cascode topology ($Q_{1\text{-}2}$) to achieve both high gain and reverse isolation. A large capacitor (C_{2S}) is connected in series with the secondary winding inductor (L_{2S}) of the transformer to prevent the dc current from flowing to the ground through L_{2S}. The second stage is based on a differential amplifier ($Q_{4\text{-}7}$) with a tail current source (Q_3), and it acts as the inverting amplifier with a gain of $-2A$ as shown in Fig. 5.1(a). All transistors ($Q_{1\text{-}7}$) have an identical size with a one-finger emitter having 0.13-μm width and 10.16-μm length, and two-finger base and collector. It should be noted that, for simplicity, the inverting amplifiers of the equivalent circuits as shown in Fig. 5.1 are based on an ideal amplifier model including the inter-stage matching inductor (L_{M2}) and capacitor (C_{M2}). In practice, the inter-stage matching components as well as the non-ideal common ground condition at the differential amplifier's input affect the dual-band response and need to be taken in to account in the design process.

A wideband matching [18] is used for the input network to cover the entire dual passbands. This wideband matching circuit uses less number of inductors and interconnection lines as compared to conventional multiband matching circuits, hence resulting in smaller size and routing metal resistances leading to potentially lower NF. In addition, in order to achieve good input and output matching as well as stability over the desired passbands, the second-stage load resistor (R_{L1}, R_{L1}') and the emitter degeneration inductors (L_{E1}, L_{E2}) are used.

Fig. 5.3 shows a photograph of the developed concurrent dual-band single-to-differential LNA, which shows various inductors and interconnection lines implemented using spiral structures, microstrip line, coplanar waveguide (CPW), and grounded coplanar waveguide (GCPW). Especially, the inter-stage matching inductor L_{M2} is

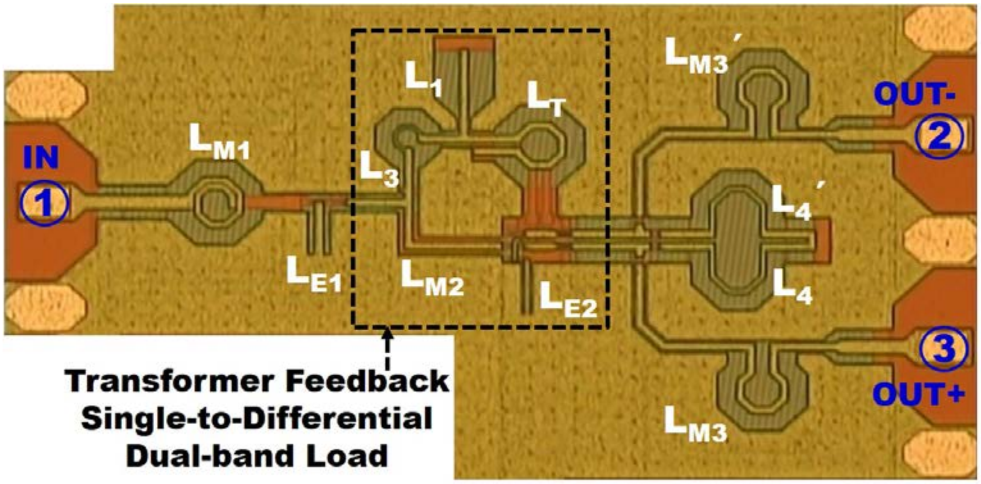

(a)

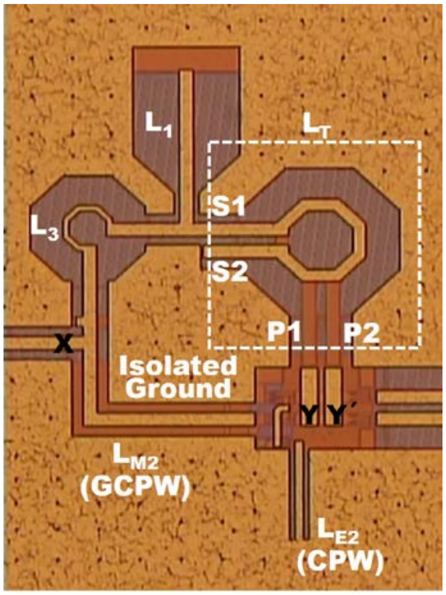

(b)

Fig. 5.3 (a) Microphotograph of the fabricated concurrent dual-band single-to-differential LNA and (b) Close-up microphotograph around the transformer feedback single-to-differential dual-band load shown in (a).

realized using the GCPW line, which utilizes the small isolated ground area, enclosed by the transformer feedback path between *X* and *Y*–*Y*´, as one of the CPW's ground lines, facilitating the connection of the isolated ground patch to the large main ground plane as

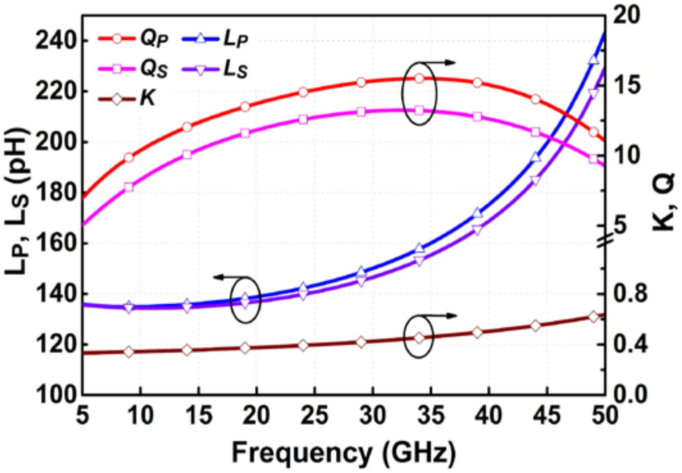

Fig. 5.4 Transformer 3D EM simulation results for self-inductances (L_P, L_S), Q-factor (Q_P and Q_S for the respective primary and secondary inductors), and mutual coupling coefficient (K).

shown in Fig. 5.3, thereby effectively creating a better ground. The *L*-shape transformer L_T shown in Fig. 5.3(b) is designed using the stacked top-most metals M_6 and M_5. The designed transformer exhibits the self-inductances of 150/146 pH, *Q*-factors of 13.1/15.3 for the primary/secondary inductors, respectively, and magnetic coupling coefficient *K* of 0.43 at 30 GHz as shown in Fig. 5.4. Since the parasitic capacitance at the first-stage's output node *X* causes more detrimental effect on the LNA gain degradation than that at the second-stage's node *Y*, the top metal M_6 is used for the secondary inductor (S1–S2) to reduce the parasitic capacitance at node *X*, while the metal M_5 is used for the primary inductor (P1–P2) connected to node *Y*–*Y*´ as seen in Fig. 3. Extensive EM simulations for the components in the feedback dual-band loop were performed – from individual inductors to the whole feedback dual-band load structure including the load inductors (L_1, L_3), the feedback transformer (L_T), and the inter-stage matching inductor (L_{M2}).

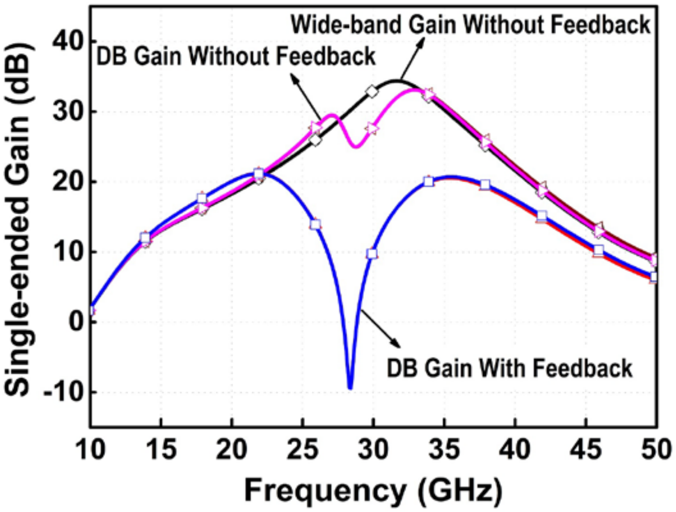

Fig. 5.5 Single-ended power gain (S_{21}, S_{31}) simulation results of the concurrent dual-band single-to-differential LNA with and without transformer feedback.

The advantage of proposed feedback dual-band load toward high stopband rejection performance has been verified as shown in Fig. 5. With the similar method presented in the developed tri-band LNA [23], the single-to-differential LNA with the transformer feedback dual-band load can be modified to two single-to-differential LNAs:

1) a wideband (or single-band) single-to-differential LNA by disconnecting the node *N*–*N´* from the node *Y*–*Y´*

2) a dual-band single-to-differential LNA with the modified transformer-based dual-band load without feedback loop by rerouting the node *N*–*N´* to the AC ground after detaching it from the node *Y*–*Y´*.

As seen in Fig. 5.5, the dual-band single-to-differential LNA without feedback only exhibits the worst-case SRR of 5 dB. On the other hand, the dual-band single-to-

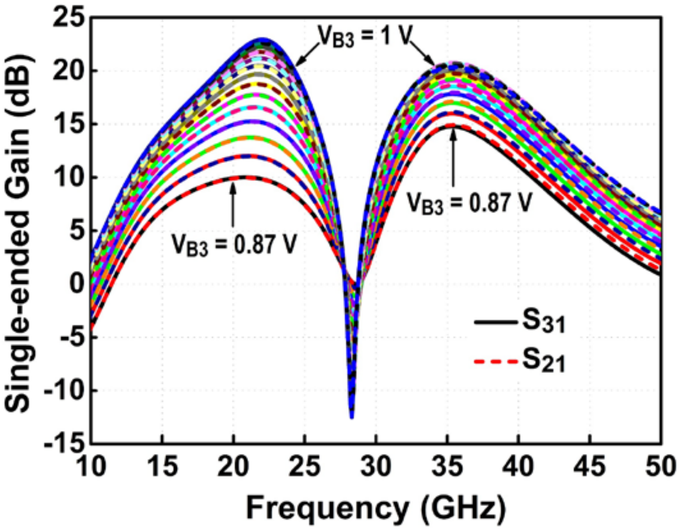

Fig. 5.6 Single-ended power gain (S_{21}, S_{31}) simulation results of the concurrent dual-band single-to-differential LNA for different V_{BE3} from 0.87 V to 1 V with a 0.01-V step.

differential LNA with the proposed feedback dual-and load significantly improves the stopband rejection performance with the SRR of higher than 30 dB. The substantial improvement of stopband rejection performance by the designed dual-band single-to-differential LNA validates the effectiveness and unique operation characteristics of the proposed transformer feedback dual-band load. It is observed that the feedback loop can widen the overall bandwidth by reducing the passband gains, and the stopband notch frequency is shifted down due to the loading effect from the second-stage node Y–Y'.

The differential pair transistors ($Q_{4\text{-}5}$) including the tail current source transistor (Q_3) of the LNA's second-stage in Fig. 5.2 act as the inverting amplifier of the transformer feedback dual-band load shown in Fig. 5.1(a). Thus, by controlling the bias voltage V_{B3} of the inverting amplifier, the designed concurrent dual-band single-to-differential LNA can provide fine tuning ability for both the passband gains and SRR at the same time as shown in Fig. 5.6. As V_{B3} is increased from 0.87 V to 1 V with 0.01-V step, higher passband gains and stopband rejection can be obtained. It is also observed that the passband signals experience no detrimental effect from the stopband signal cancellation as the gain increases along with increasing V_{B3}. The deeper notches in the stopband occur when the inverted stopband signal by the second-stage's inverting amplifier and the feedforwarded stopband signal through the notch filter are close to the 180° out-of-phase at node Y–Y'.

When V_{B3} lower than 0. 95 V is applied, the peak gains at high-passband are higher than those at low-passband. However, once V_{B3} is increased more than 0.95 V, the peak gains at low-passband become larger than those at high-passband and the SRR is further enhanced. It is found that the peak gains at both low/high-passbands are identical as 20.4 dB with V_{B3} of 0.95 V, resulting in a total current of 18 mA at the tail current source Q_3. At this equilibrium bias condition, the designed concurrent dual-band single-to-differential LNA achieves the simulated SRR of 28.5 dB with the stopband notch response of −8.1 dB. This bias tuning technique is useful for finding the optimum bias point of the LNA to achieve not only low gain imbalance between the passbands, but also high SRR at the stopband, by compensating for possible changes of the Q-factor of the feedback dual-band load due to unavoidable design variations originating from process, voltage, and temperature changes. Therefore, the designed concurrent dual-band single-to-differential LNA can provide great flexibility for obtaining both optimum gain balance and SRR performances.

5.4 Experimental and Simulated Results

The concurrent dual-band single-to-differential LNA shown in Fig. 5.3 was fabricated with 0.18-μm BiCMOS process having f_T/f_{max} of 240/280 GHz [24] and has a core area of 1.02 mm × 0.68 mm. The LNA was measured on-wafer. The first-stage bias voltage (V_{B1}) was fixed at 0.9 V, which drew around 9.5 mA, and the second-stage bias (V_{B3}) was tuned to achieve minimum gain imbalance between the passbands (around 22 and 36 GHz) and maximum SRR at the same time.

Figure 5.7 shows the simulated and measured single-to- differential power gains of the LNA. The LNA achieves identical peak gains of 19.2 dB in each passband with

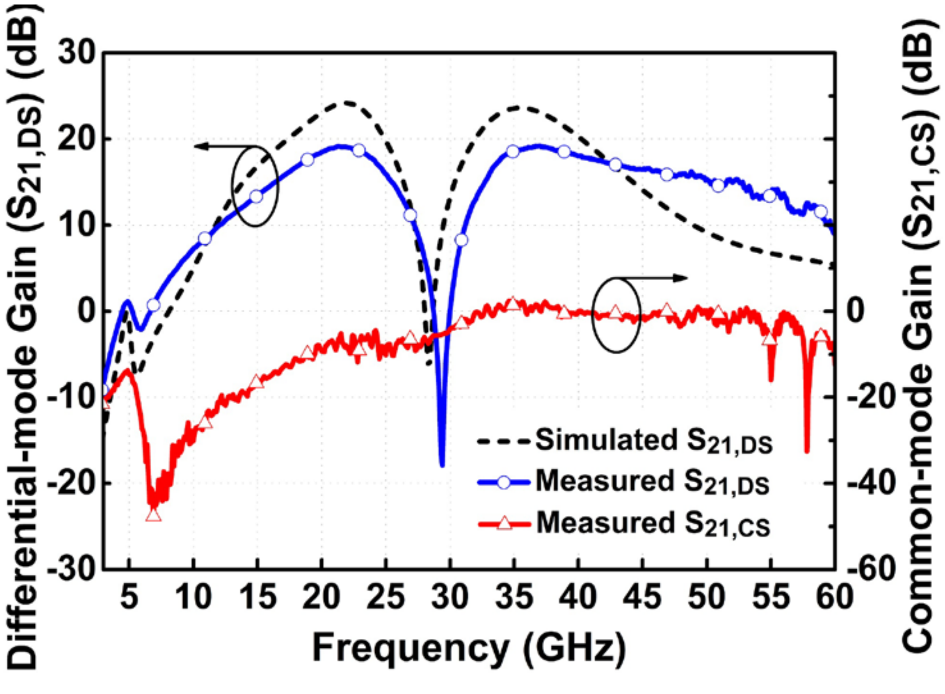

Fig. 5.7 Measured and simulated single-input to differential-output power gains ($S_{21,ds}$) and measured single-input to common-mode gain ($S_{21,cs}$).

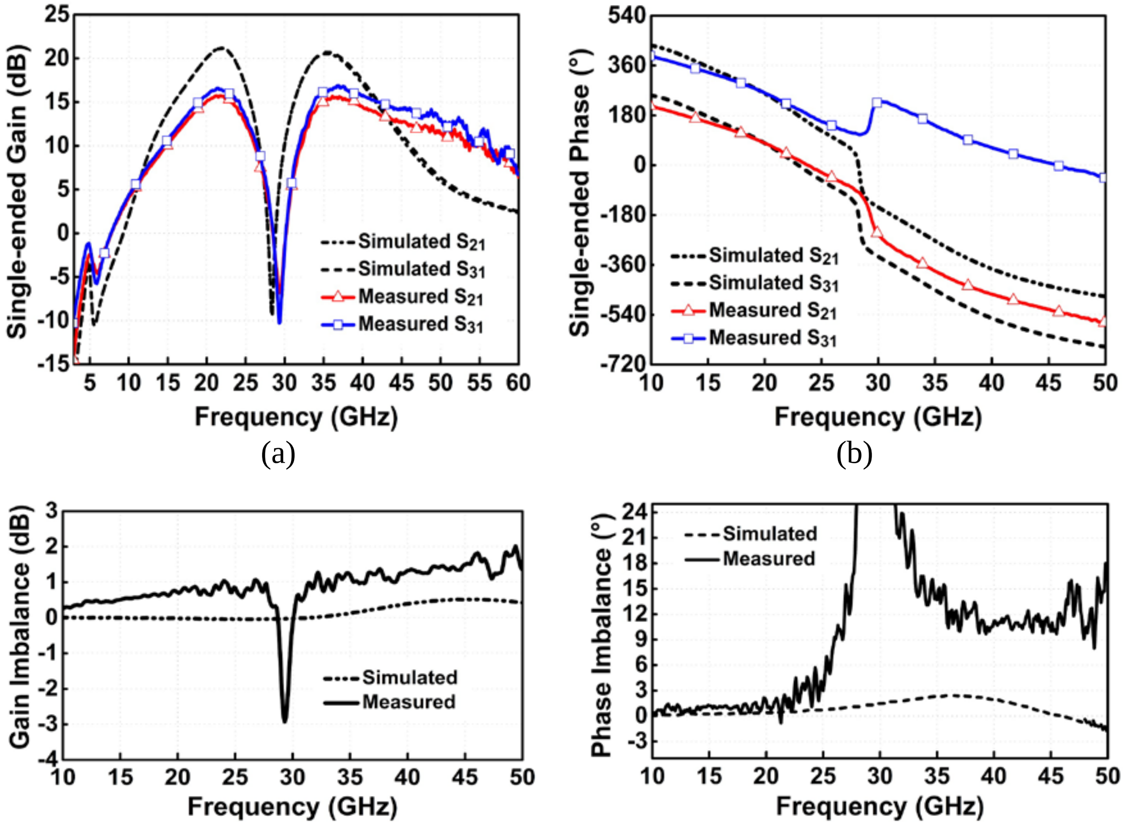

(a) (b)

(c) (d)

Fig. 5.8 Measured and simulated results for single-input to single-output: single-ended (S_{21}, S_{31}) power gain (a) and phase (b), differential gain imbalance (c), and differential phase imbalance (d).

the second-stage's bias current of 20 mA and shows a measured stopband notch response of −17.9 dB. The LNA hence achieves a SRR of 37.1 dB for the single-to-differential mode operation. It exhibits measured 3-dB bandwidths of 7.5 GHz (17.5–25 GHz) and 12.6 GHz (33.2–45.8 GHz) for the low and high passbands, respectively. The lowest measured single-input to common-mode gain ($S_{21,\mathrm{cs}}$) is −5.2/2.2 dB in the low/high passbands, respectively. The applied bias condition results in well-balanced measured

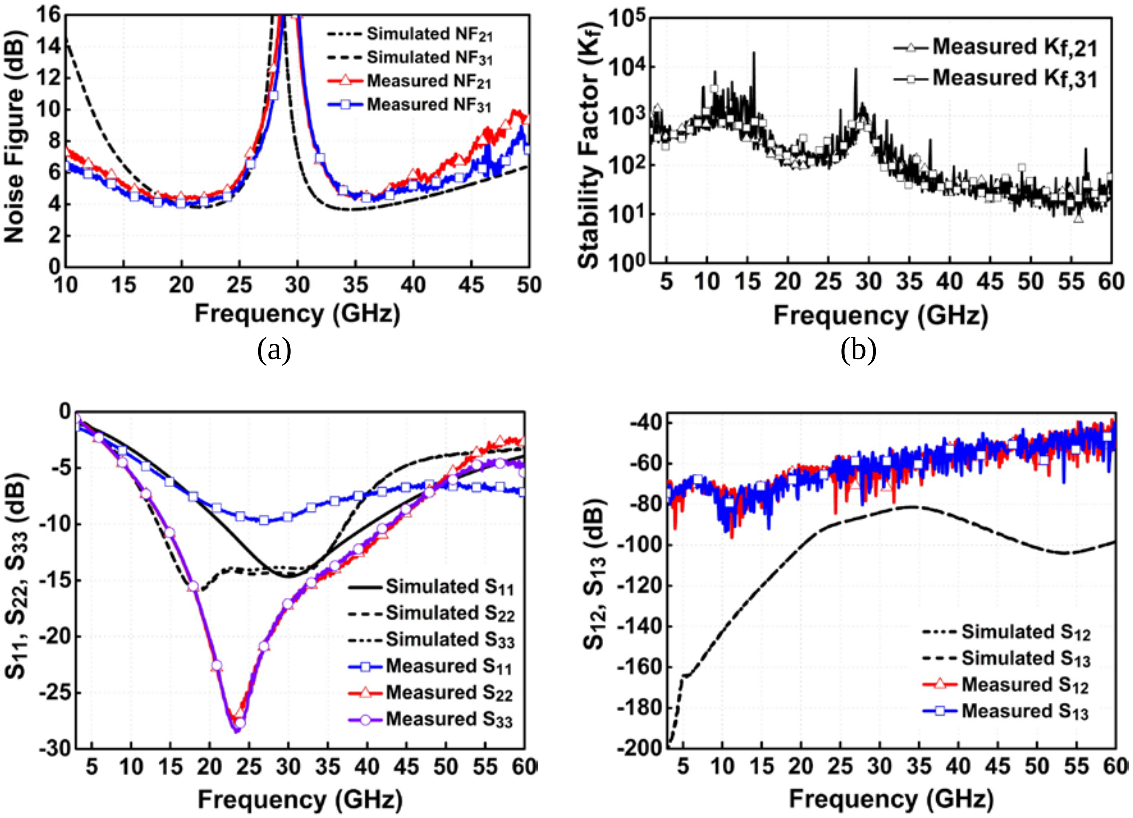

(a) (b)

(c) (d)

Fig. 5.9 Measured and simulated results comparison. (a) NF, (b) measured stability factor, (c) input and output matching (S_{11}, S_{22}, and S_{33}), (d) reverse isolation (S_{12} and S_{13}).

single-to-differential passband gains and hence was also used for the single-ended mode operation of the concurrent dual-band single-to-differential LNA.

Figures 5.8(a) and (b) show the simulated and measured single-ended mode power gains and phases at the two output ports (S_{21}, S_{31}) of the concurrent dual-band single-to- differential LNA, respectively, and Figs. 5.8(c) and (d) display the respective differential gain and phase imbalances. The measured peak gains for S_{21}/S_{31} are 15.7/16.6 dB at 21.5 GHz and 15.7/16.7 dB at 36 GHz, respectively. The LNA shows

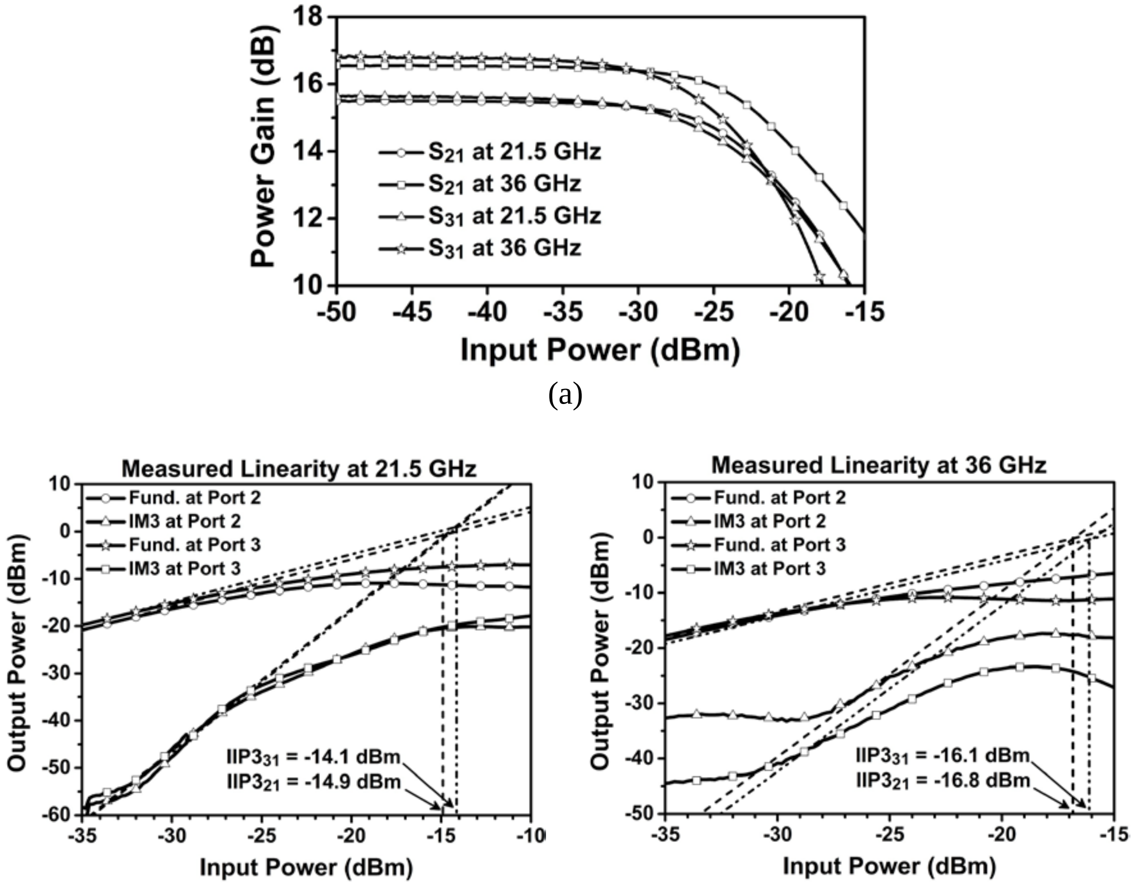

(a)

(b) (c)

Fig. 5.10 (a) Measured input P_{1dB}. Measured input IP_3 (IIP_3) at 21.5 GHz (low-passband) (b) and 36 GHz (high-passband) (c).

0.9/1.0-dB differential gain imbalances in the low/high passbands, respectively. The smallest measured differential phase imbalances of 0.5/10.4 degrees are observed in the low/high passbands, respectively. Fig. 5.9(a) shows the simulated and measured noise figures (NF_{21} and NF_{31}) of the LNA for the two signal paths (ports 1 to 2 and 1 to 3), respectively. The best NFs of 4.3/4.0 dB and 4.3/4.2 dB are obtained in the low and high

TABLE 5.2
Performance Summary of Single-to-Differential Baluns and LNAs

Reference	Technology	Frequency (GHz)	Gain (at S_{21} / S_{31}) (dB)	NF (NF_{21} / NF_{31}) (dB)	Input P_{1dB} ($IP_{1dB,21}$ / $IP_{1dB,31}$) (dBm)	Input IP_3 ($IIP_{3,21}$ / $IIP_{3,31}$) (dBm)	Gain Imbalance (dB)	Phase Imbalance (degree)	Power (mW)	Area (mm^2)
1 (Single-Band)	0.25-μm SiGe BiCMOS	20.5	6.31 / 6.7 (Single-ended)	4.89 / 5.91	0	9	0.39	39	46.2	1.6
2 (Single-Band)	0.13-μm CMOS	24	10.8 / 10.2 (14.7 at Single-to-Differential)	4.32 / 4.41	–10.7	—	0.6	0.47	20.2	0.82
3 (Single-Band)	0.25-μm SiGe:C BiCMOS	24	13.2 (Differential)	4.2	–18.5	–6	1	20[c]	39.6	0.33
4 (Single-Band)	0.13-μm CMOS	21	15.0 (Differential)	7.2	—	–16.8	1.8	0.3	26.4	0.2
5 (Single-Band)	0.13-μm SiGe BiCMOS	58.4	–1.4 / –1.8 (Single-ended)	—	—	—	1.2	10	10.4	0.04
6 (Single-Band)	90-nm CMOS	63	10.1 / 8.5 (Single-ended)	8.6	—	–7	1.7	6.8	19	0.275
21[a] (Switching Dual-Band)	0.18-μm CMOS	1.2	25[b] (Differential)	2.1	—	–5.7	—	—	6.3	0.357
		1.57	22[b] (Differential)	2.3	—	–3.3				
22[a] (Switching Dual-Band)	65-nm CMOS	4.5	15	4	–1.1	8	1	2.5	10.8	0.29
		8	18	4	—	5				
This Work (Concurrent Dual-Band)	**0.18-μm SiGe BiCMOS**	**21.5**	**15.7 / 16.6 (19.2 at Single-to-Differential)**	**4.3 / 4.0**	**–24.3 / –23.4**	**–14.9 / –14.1**	**0.9**	**0.5**	**73.8**	**0.69**
		36	**15.7 / 16.7 (19.2 at Single-to-Differential)**	**4.3 / 4.2**	**–25.8 / –26.9**	**–16.8 / –16.1**	**1.0**	**10.4**		

[a] Only simulated performances are reported.
[b] Voltage gain.
[c] Estimated value from the measurement result.

passbands, respectively. The simulated and measured input and output matching as well as reverse isolation are shown in Figs. 5.9(b) and (c), respectively. Fig. 5.9(d) displays the measured stability factors ($K_{f,21}$ and $K_{f,31}$) corresponding to the two output ports, showing that the LNA is unconditionally stable over all frequencies. Fig. 5.10 shows the measured linearity of the LNA. The input P_{1dB}'s corresponding to S_{21}/S_{31} are

−24.3/−23.4 and −25.8/−26.9 dBm in the low and high passbands, respectively. The input IP_3 points of −14.9/−14.1 and −16.8/−16.1 dBm were measured in the low and high passbands for the two signal paths, respectively.

Table 5.2 summarizes the measured results of the developed concurrent dual-band single-to-differential LNA and compares the performances of reported single-band single-to-differential active baluns and LNAs operating above 20 GHz as well as switching dual-band single-to-differential LNAs. It should be noted again that there have been no concurrent dual-band single-to-differential LNAs reported to date. The reported dual-band single-to-differential LNAs [41], [42] are based on “switching” and hence are not concurrent. Moreover, they operate below 10 GHz and their performances are based only on the simulated results. The developed concurrent dual-band single-to-differential LNA exhibits excellent gain, gain/phase balances, and NF performances as well as a great stopband rejection, validating the unique advantages of the proposed concurrent dual-band transformer feedback single-to- differential LNA.

5.5 Summary and Conclusion

The concurrent dual-band transformer feedback single-to-differential LNA employing a unique transformer feedback single-to-differential dual-band load has been proposed. The concurrent dual-band single-to-differential LNA was successfully developed for two different bands around 22 and 36 GHz using a 0.18-μm BiCMOS technology. The developed concurrent dual-band single-to-differential LNA achieves excellent gain balance and stopband rejection performances. The proposed transformer feedback single-to-differential dual-band load and concurrent dual-band transformer feedback single-to-differential LNA architecture could be extended for single-to-differential designs involving more than two bands not only for amplifiers but also for other components. The developed LNA is the first true concurrent dual-band single-to-differential amplifier operating up to millimeter-wave frequencies and without using switching mechanism.

CHAPTER VI

CONCURRENT DUAL-BAND MERGED LOW-NOISE AMPLIFIER AND MIXER

In this chapter, a new concurrent dual-band merged single-to-differential LNA and RF-to-IF down-conversion mixer implementing the proposed single-to-differential transformer feedback dual-band load (described in Ch. V) is presented. The single-to-differential transformer feedback dual-band load is used as a concurrent dual-band single-to-differential transconductance (g_m) amplifier, which simultaneously converts two independent single-ended RF voltage signals at around 24.5 and 36.5 GHz into the 180° out-of-phase differential current signals. Moreover, the concurrent dual-band single-to-differential transformer feedback dual-band load also lowers the conversion NF by providing some amount of gain at the first-stage amplifier.

The two cascode transistors at the second-stage of the single-to-differential LNA (shown in Fig. 5.2) are replaced with the four switching transistors at the proposed dual-band mixer core, which place on top of the concurrent dual-band transconductance amplifier. With a 21-GHz single-ended LO signal, the down-converted dual IF bands are located at 3.5/15.5 GHz for two passband signals at 24.5/36.5 GHz, respectively.

The developed merged LNA and mixer is the first fully integrated concurrent dual-band mixer operating up to millimeter-wave frequencies without using any switching mechanism.

6.1 Design of Concurrent Dual-band Merged LNA and Mixer

The developed single-to-differential transformer feedback concurrent dual-band load shown in Fig. 5.1 can also be used in the mixer design. Fig. 6.1 shows the proposed concurrent dual-band merged LNA and (RF-to-IF) down-conversion mixer. The first-stage amplifier ($Q_{1\text{-}2}$) and the second-stage differential pair ($Q_{3\text{-}5}$) are designed based on the concurrent dual-band single-to-differential LNA shown in Fig. 5.2. The transistors ($Q_{6\text{-}9}$) form a switching core of the double-balanced Gilbert-cell mixer [19].

The operation principle of the proposed concurrent dual-band merged LNA and mixer is similar to that of the concurrent dual-band single-to-differential LNA with the signal conversion executed by the Gilbert mixer. The single-to-differential transformer

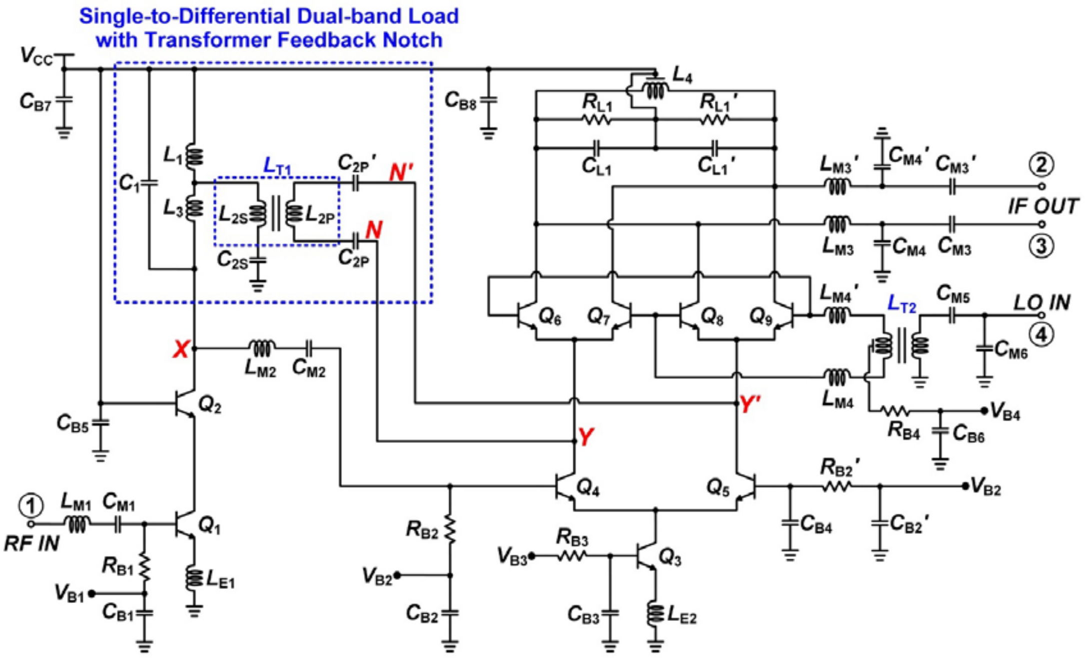

Fig. 6.1 Schematic of the concurrent dual-band merged LNA and mixer employing the

feedback dual-band load seen in Fig. 5.1 is used as a concurrent dual-band single-to-differential transconductance (g_m) amplifier, which simultaneously converts two independent single-ended RF voltage signals at around 24.5 and 36.5 GHz (received from Port 1) into the 180° out-of-phase differential current signals flowing into the mixer switching core. A 21-GHz single-ended LO signal is applied to Port 4 and converted into the differential LO signals via the transformer L_{T2}, and the differential LO signals are delivered to the gate of the switching transistors.

The amplified dual-band RF current signals flowing into the source of the four switching transistors will be down-converted to the IF domain (at 3.5 and 15.5 GHz) by the switching activity of the differential LO signals ($f_{IF} = f_{RF} - f_{LO}$). At the double-balanced Gilbert-cell mixer switching core, only two switching transistors (Q_6, Q_9) are turned on while the others (Q_7, Q_8) remain off and vice versa. The proposed concurrent dual-band merged LNA and mixer integrates the first-stage amplifier as a single-to-differential feedback dual-band load and hence it provides more gain by the integrated first-stage amplifier as compared to the conventional merged LNA and mixer which does not have the first-stage amplifier. The added gain by the first-stage amplification of the proposed merged LNA and mixer reduces the overall conversion NF of the mixer.

While the single-to-differential LNA in Fig. 5.2 uses a wideband matching at its output, the proposed concurrent dual-band merged LNA and mixer matches its output to two down-converted IF bands at 3.5/15.5 GHz (Ports 2 and 3), respectively. The differential inductor (L_4), two capacitors (C_{L1}, C_{L1}') and two de-Q resistors (R_{L1}, R_{L1}')

are used as the mixer output load together with the matching inductors (L_{M3}, L_{M3}') and capacitors (C_{M3-4}, C_{M3-4}').

The differential pair transistors (Q_{4-5}) including the tail current source transistor (Q_3) of the second-stage transconductance amplifier in Fig. 6.1 act as the inverting amplifier of the transformer feedback dual-band load as seen in Fig. 5.1. Thus, by controlling the bias voltage V_{B3} of the inverting amplifier, the designed concurrent dual-band merged LNA and mixer can also control both the passband gains and SRR at the same time. The designed merged LNA and mixer shows a substantial improvement of stopband rejection performance and validates the effectiveness and unique operation characteristics of the proposed transformer feedback dual-band load and its use in the down-conversion mixer.

6.2 Experimental and Simulated Results

The concurrent dual-band merged LNA and mixer was fabricated with 0.18-μm BiCMOS process having f_T/f_{max} of 240/280 GHz [24] as shown in Fig. 6.2. It has a core area of 1.2 mm × 0.8 mm and was measured on-wafer. The merged LNA and mixer layout is based on the same platform of the single-to-differential LNA shown in Fig. 5.3. Thus, the same single-to-differential transformer feedback dual-band load seen in Fig. 5.3(b) was used in the merged LNA and mixer as shown in Fig. 6.2(b), but the mixer switching core transistors as well as the matching components at both the LO input and IF output were redesigned.

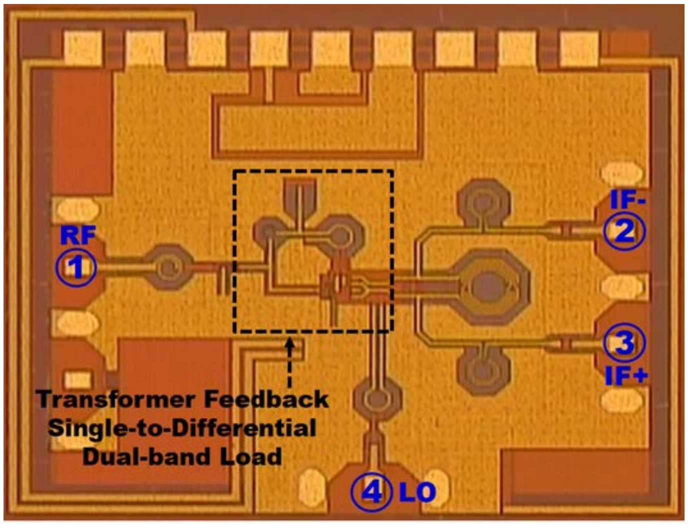

(a)

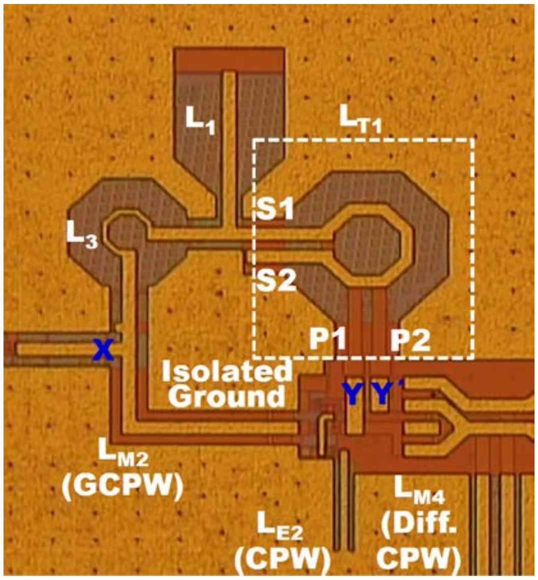

(b)

Fig. 6.2 (a) Microphotograph of the fabricated concurrent dual-band single-to-differential merged LNA and mixer and (b) Close-up microphotograph around the transformer feedback single-to-differential dual-band load shown in (a).

With a 2.5-V supply voltage, the merged LNA and mixer consumes the 62.5/92.5-mW power at high gain balance (GB)/high stopband rejection ratio (SRR)

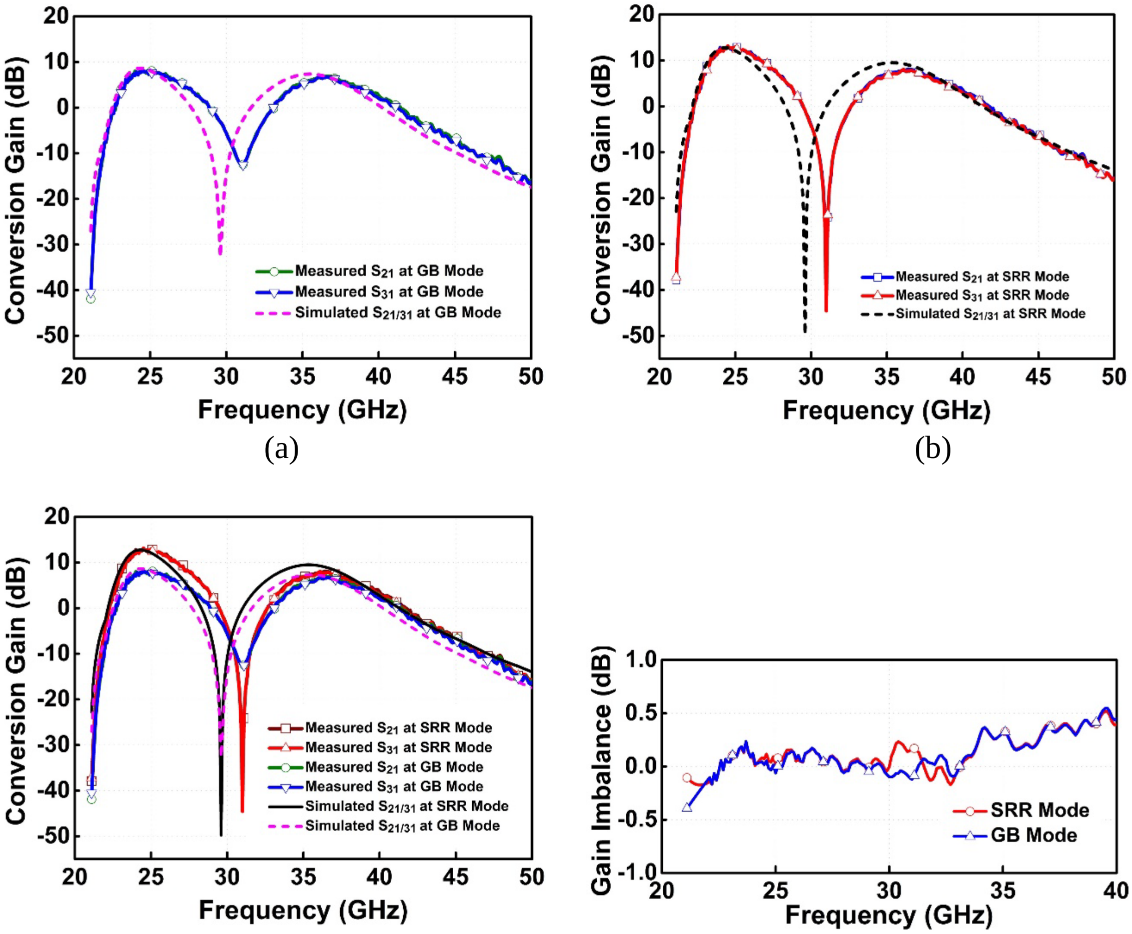

(c) (d)

Fig. 6.3 Measured and simulated single-ended conversion gain for Ports 1 to 2 and 1 to 3 (S_{21}, S_{31}): (a) GB mode, (b) SRR mode, and (c) combined conversion gain graphs of GB and SRR modes for comparison. (d) Measured differential gain imbalance between two signal paths ($|S_{21,\mathrm{dB}}| - |S_{31,\mathrm{dB}}|$).

modes, respectively. The first-stage bias voltage (V_{B1}) was fixed at 0.98 V, which drew around 12 mA, and the second-stage bias (V_{B3}) was tuned to control the passband gain and the SRR at the same time. Fig. 6.3 shows the measured conversion gain and differential gain imbalance responses of the concurrent dual-band merged LNA and mixer at the two output ports (S_{21}, S_{31}) for two representative operating conditions: 1) high gain-balance (GB) mode between two passbands (around 24.5 and 36.5 GHz) and 2) high stopband rejection ratio (SRR) mode. At the high GB mode, the gain differences between two passbands are minimized with lower stopband notch attenuation. On the other hand, at the high SRR mode, the stopband notch attenuation is maximized with a larger passband gain differences.

At high GB mode, the measured conversion gains for S_{21}/S_{31} paths are 8.1/8.3 dB at 24.5 GHz and 6.9/6.7 dB at 36.5 GHz, respectively, as shown in Fig. 6.3(a). The conversion gain differences between low- and high-passbands are 1.2/1.6 dB at respective S_{21}/S_{31} paths. The SRRs of 20.5/20.7 dB at low-band and 19.5/19.3 dB at high-band are obtained for respective S_{21}/S_{31} paths from the measured conversion gains at each passband. At high SRR mode, the measured conversion gains of 12.9/13.1 dB at 24.5 GHz and 8.0/7.8 dB at 36.5 GHz are obtained for S_{21}/S_{31} paths, respectively, as

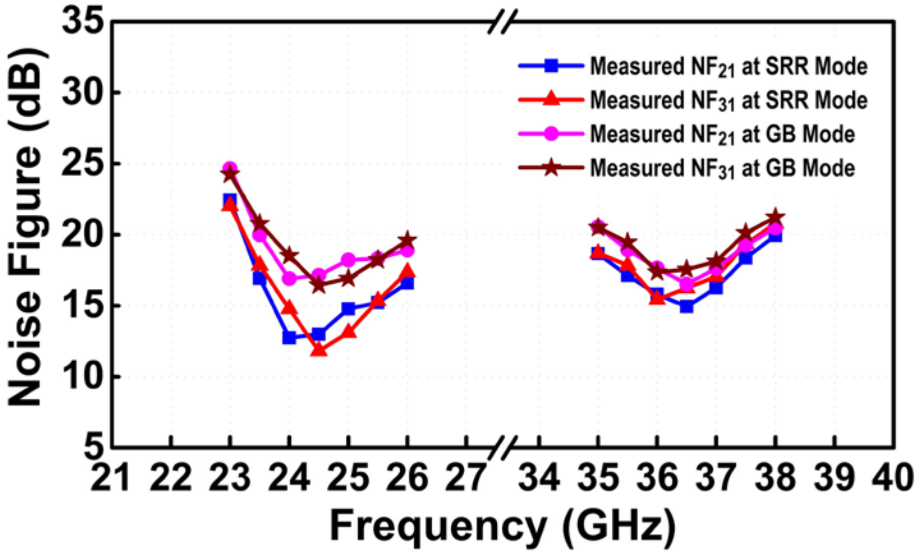

Fig. 6.4 Measured single-ended NF for Ports 1 to 2 and 1 to 3 (NF_{21}, NF_{31}).

shown in Fig. 6.3(b). The conversion gain differences between low- and high-passbands are 4.9/5.3 dB at respective S_{21}/S_{31} paths. The SRRs of 57.7/57.9 dB at low-band and 52.5/52.3 dB at high-band are obtained for respective S_{21}/S_{31} paths. Fig. 6.3(c) compares the conversion gain responses of both GB and SRR modes. The differential gain imbalances remain lower than 0.3/0.4 dB at low/high-passbands, respectively, as shown in Fig. 6.3(d).

Figure 6.4 shows the measured noise figures (NF_{21} and NF_{31}) of the merged LNA and mixer for the two signal paths (Ports 1 to 2 and 1 to 3), respectively. At high GB mode, the best NFs of 16.9/16.4 dB and 16.5/17.3 dB are obtained in the low- and high-passbands, respectively. At high SRR mode, the best NFs of 12.7/11.8 dB and 14.9/15.3 dB are obtained in the low-and high-passbands, respectively. The measured and simulated matching characteristics at RF, IF, and LO ports are shown in Fig. 6.5.

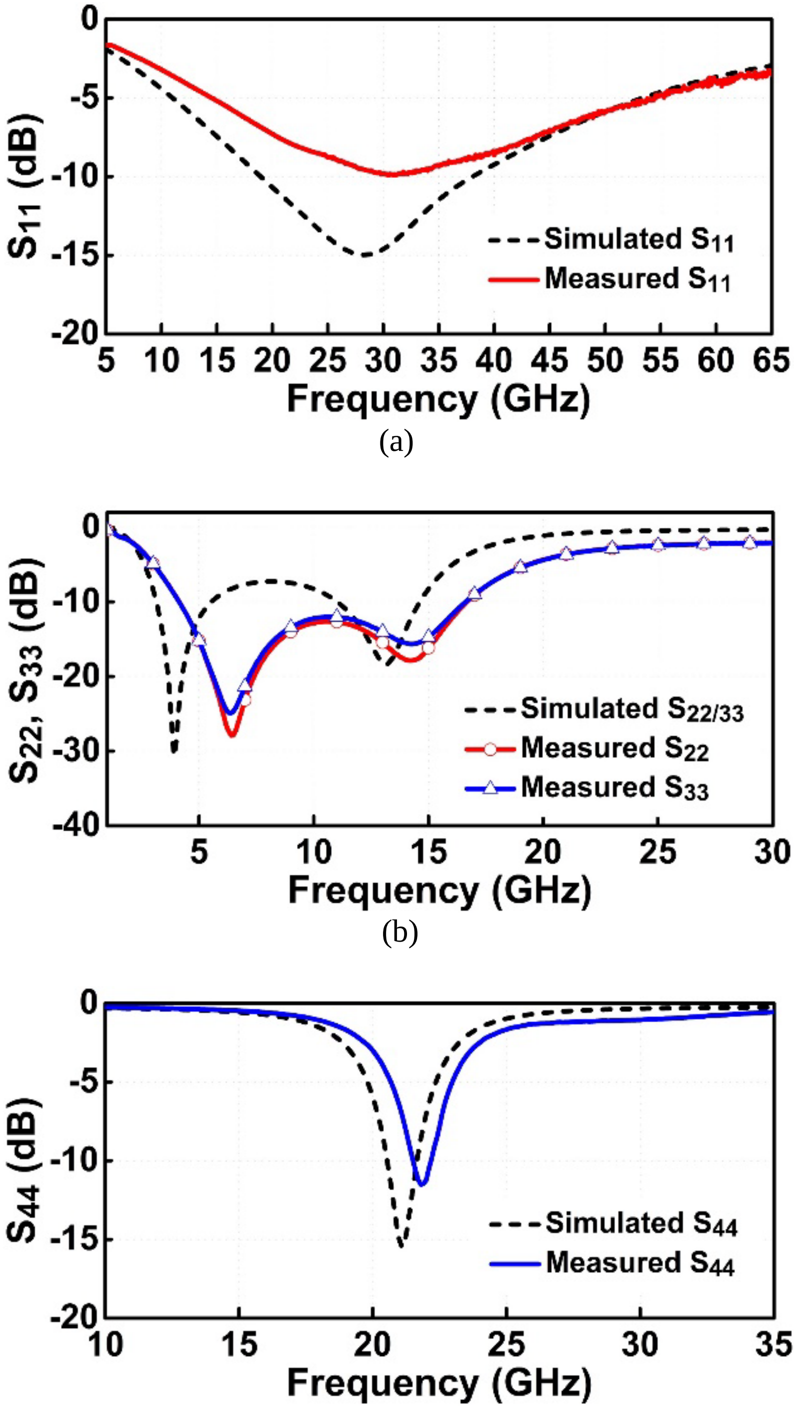

(a)

(b)

(c)

Fig. 6.5 Measured and simulated matching responses at: (a) RF input (Port1), (b) IF output (Ports 2 and 3), and (c) LO input (Port 4).

Figure 6.6 shows the measured conversion gain responses as a function of LO power level. Since the peak conversion gains occurs when the LO power of around −2 dBm is applied for all gain modes, this power level is chosen for a reference LO input power to measure the performance of merged LNA and mixer for the small signal performances described before as well as the two-tone inter-modulation measurement.

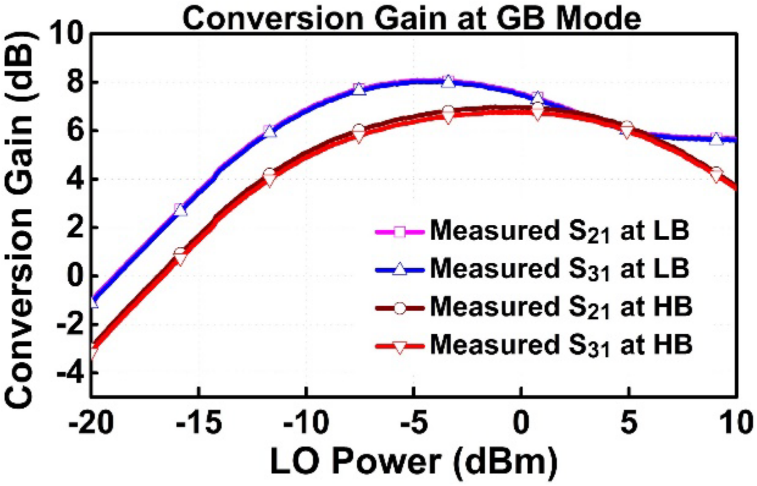

(a)

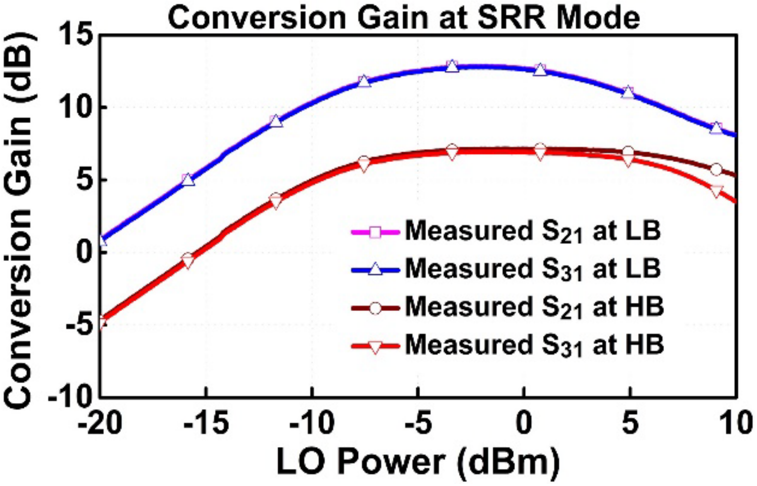

(b)

Fig. 6.6 Measured single-ended conversion gain for Ports 1 to 2 and 1 to 3 (S_{21}, S_{31}) as a function of LO power at: (a) high GB mode and (b) high SRR mode.

The measured conversion gains responses obtained by varying the RF input power are shown in Fig. 6.7. At high GB mode, the measured input P_{1dB} ($IP_{1dB,21}$/$IP_{1dB,31}$) for the two signal paths (Ports 1 to 2 and 1 to 3) are –24.7/–24.6 dB at 24.5 GHz and –27.4/–27.4 dB at 36.5 GHz, respectively. At high SRR mode, the measured $IP_{1dB,21}$/$IP_{1dB,31}$ are –23.8/–23.7 dB at 24.5 GHz and –28.4/–28.4 dB at 36.5 GHz, respectively.

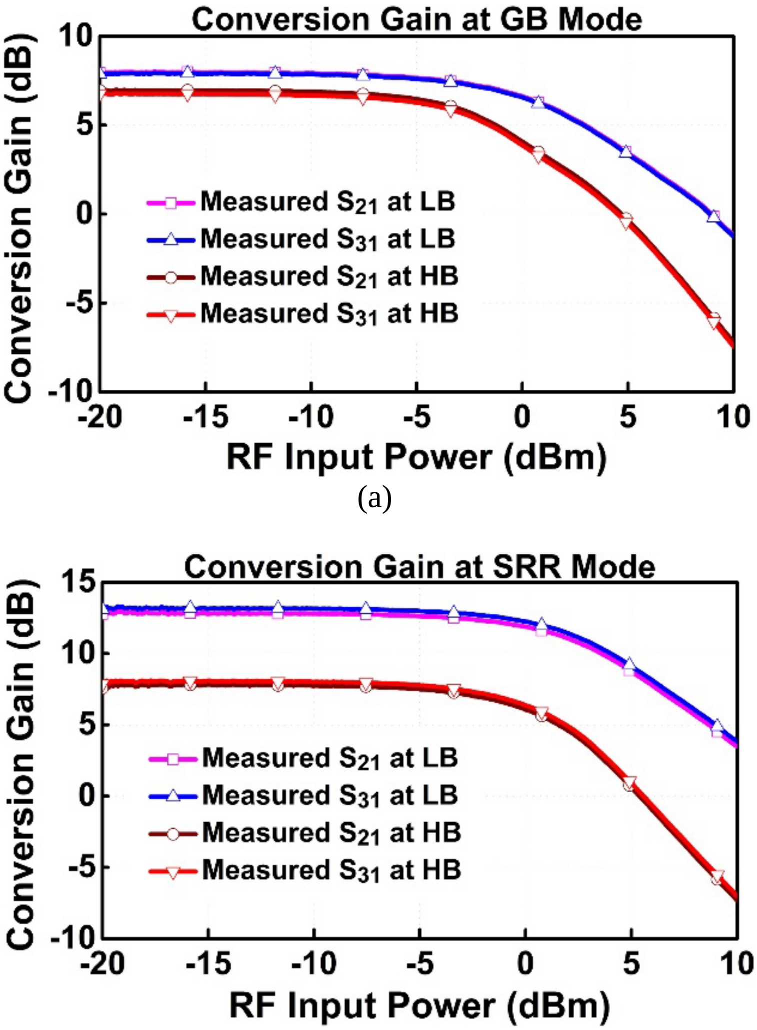

(a)

(b)

Fig. 6.7 Measured single-ended conversion gain for Ports 1 to 2 and 1 to 3 (S_{21}, S_{31}) as a function of RF power at: (a) high GB mode and (b) high SRR mode.

Figure 6.8 shows the measured input IP3 ($IIP_{3,21}/IIP_{3,31}$) for the two signal paths. The two-tone signals with 1-MHz spacing are applied for each passband located at 24.5/36.5 GHz. At high GB mode, the measured $IIP_{3,21}/IIP_{3,31}$ are –14.4/–14.3 dB at 24.5 GHz and –18.6/–18.4 dB at 36.5 GHz, respectively. At high SRR mode, the measured $IIP_{3,21}/IIP_{3,31}$ are –13.0/–12.9 dB at 24.5 GHz and –16.1/–15.9 dB at 36.5 GHz, respectively. The measured results of the developed merged LNA and mixer are summarized in Table 6.1.

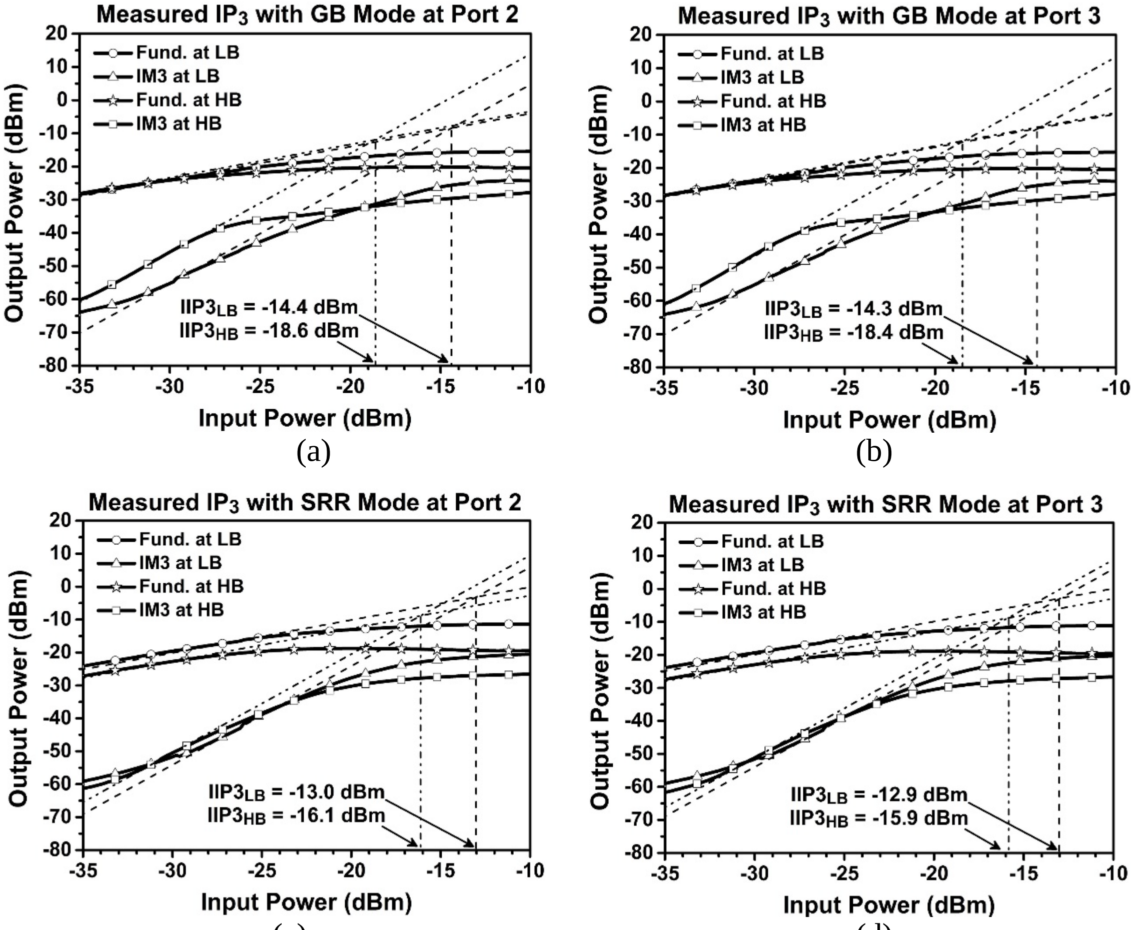

(a) (b)

(c) (d)

Fig. 6.8 Measured single-ended input IP_3: $IP_{3,21}$ (a) and $IP_{3,31}$ (b) at high GB mode. $IP_{3,21}$ (c) and $IP_{3,31}$ (d) at high SRR mode.

TABLE 6.1
MEASURED PERFORMANCE OF THE CONCURRENT DUAL-BAND MERGED LNA AND MIXER

Mixer Operation Mode	Frequency (GHz)	Conversion Gain (S_{21} / S_{31}) (dB)	NF (NF_{21} / NF_{31}) (dB)	Input P_{1dB} ($IP_{1dB,21}$ / $IP_{1dB,31}$) (dBm)	Input IP_3 ($IIP_{3,21}$ / $IIP_{3,31}$) (dBm)	Differential Gain Imbalance (dB)	Stopband Rejection Ratio (dB)	Isolation (dB)		
								RF-to-IF (S_{12} / S_{13})	LO-to-IF (S_{24} / S_{34})	LO-to-RF (S_{14})
High Gain Balance (GB)	24.5	8.1 / 8.3	16.9 / 16.4	–24.7 / –24.6	–14.4 / –14.3	< 0.3	20.5 / 20.7	26.7 / 31.5	32.8 / 31.5	46.1
	36.5	6.9 / 6.7	16.5 / 17.3	–27.4 / –27.4	–18.6 / –18.4	< 0.4	19.5 / 19.3	33.3 / 34.1		
High Stopband Rejection (SRR)	24.5	12.9 / 13.1	12.7 / 11.8	–23.8 / –23.7	–13.0 / –12.9	< 0.3	57.7 / 57.9	15.5 / 18.2	32.5 / 28.2	44.0
	36.5	8.0 / 7.8	14.9 / 15.3	–28.4 / –28.4	–16.1 / –15.9	< 0.4	52.5 / 52.3	24.5 / 26.5		

TABLE 6.2
PERFORMANCE SUMMARY AND COMPARISON OF DUAL-BAND MIXERS

Reference	Technology	Frequency (GHz)		Gain (at S_{21} / S_{31}) (dB)	NF (NF_{21} / NF_{31}) (dB)	Input P_{1dB} ($IP_{1dB,21}$ / $IP_{1dB,31}$) (dBm)	Input IP_3 ($IIP_{3,21}$ / $IIP_{3,31}$) (dBm)	Power (mW)	Area (mm^2)
[43][a] (Concurrent Dual-Band)	0.8-μm SiGe BiCMOS		0.9	10.5	12.6	–	2.6	22.2	1.79
			1.8	10.1	13	–	0.8		
[44][b] (Concurrent Dual-Band)	0.18-μm CMOS		2.4	5	10	–14	–3.5	6.7	–
			5.5	5.8	10	–15	–4.5		
[45] (Switching Dual-Band)	0.13-μm CMOS		5	10	8.7	–5	1[c]	68	0.525
			9.8	12	10.9	–5	1[c]		
[46][d] (Switching Dual-Band)	0.18-μm SiGe BiCMOS		3.5	6.7	17.1	–	7	14.4	–
			10.5	5.2	18	–	–1	12.6	
This Work (Concurrent Dual-Band)	**0.18-μm SiGe BiCMOS**	GB Mode	24.5	8.1 / 8.3	16.9 / 16.4	–24.7 / –24.6	–14.4 / –14.3	62.5	0.96
			36.5	6.9 / 6.7	16.5 / 17.3	–27.4 / –27.4	–18.6 / –18.4		
		SRR Mode	24.5	12.9 / 13.1	12.7 / 11.8	–23.8 / –23.7	–13.0 / –12.9	92.5	
			36.5	8.0 / 7.8	14.9 / 15.3	–28.4 / –28.4	–16.1 / –15.9		

[a] Off-chip matching components were used.

[b] Only simulated performances have been reported.

[c] Estimated value from the measurement result.

[d] Performance based on IF mixer.

Table 6.2 compares the performances of existing dual-band mixers. Even though the concurrent dual-band mixers were reported in [43] and [44], they operate at low RF and microwave frequencies below 6 GHz. Moreover, the dual-band mixer in [43] was not fully integrated since it used off-chip high-Q matching components. The dual-band mixer in [44] was not fabricated and it presented only simulated performances. The concurrent dual-band mixer in [43] uses off-chip components, i.e. high-Q inductors, for input and output matching as well as for emitter degeneration. The concurrent dual-band mixer in [44] reports only simulation performances. The mixers in [45] and [46] operate based on switching mechanism, so they cannot receive and process two passbands simultaneously. The proposed dual-band merged LNA and mixer is the first fully integrated concurrent dual-band merged LNA and mixer operating up to millimeter-wave region, and it achieves the highest conversion gain with good gain balance and NF performances while operating at highest frequency region.

6.3 Summary and Conclusion

The fully integrated concurrent dual-band merged LNA and mixer employing a unique single-to-differential transformer feedback dual-band load has been successfully developed for two different bands around 24.5 and 36.5 GHz using a 0.18-μm BiCMOS technology. The developed concurrent dual-band merged LNA and mixer achieves excellent conversion gain and stopband rejection performances. The proposed single-to-differential transformer feedback dual-band load and concurrent dual-band merged LNA and mixer architecture could be extended for single-to-differential designs involving more than two bands not only for amplifiers but also for other components. In addition, the proposed concurrent dual-band single-to-differential transconductance amplifier stage could be an essential component to develop a true concurrent dual-band receiver system. The developed merged LNA and mixer is the first fully integrated concurrent dual-band mixer operating up to millimeter-wave frequencies and without using switching mechanism.

CHAPTER VII

CONCURRENT DUAL-BAND RECEIVER FRONT-END

In this chapter, a new concurrent dual-band receiver front-end is proposed. It consists of the concurrent dual-band LNA using the single-to-single transformer feedback dual-band load presented in Ch. IV and the concurrent dual-band merged LNA and mixer employing the single-to-differential transformer feedback dual-band load presented in Ch. VI. The receiver front-end operates with RF passband frequencies at around 24.5/36.5 GHz, LO frequency at 21 GHz, and accordingly IF frequencies at 3.5/15.5 GHz ($f_{IF} = f_{RF} - f_{LO}$). Since both of the dual-band LNA and the dual-band merged LNA and mixer have the functionality of controlling the stopband rejection and the passband gain balance by adjusting the bias level of second-stage inverting amplifier, the proposed receiver front-end has versatile operation modes by combining each operation mode of the dual-band LNA and the merged LNA and mixer. The developed concurrent dual-band receiver front-end achieves the highest gain and the best NF performances as well as the largest SRRs, while operating at highest frequencies up to millimeter-wave region, among the concurrent dual-band receivers reported to date.

7.1 Design of Concurrent Dual-band Receiver Front-end

The concurrent dual-band receiver architecture mentioned in Ch. I is shown again in Fig. 7.1. The designed receiver front-end (enclosed by the dashed line) consists of the concurrent dual-band LNA implementing the single-to-single transformer feedback dual-

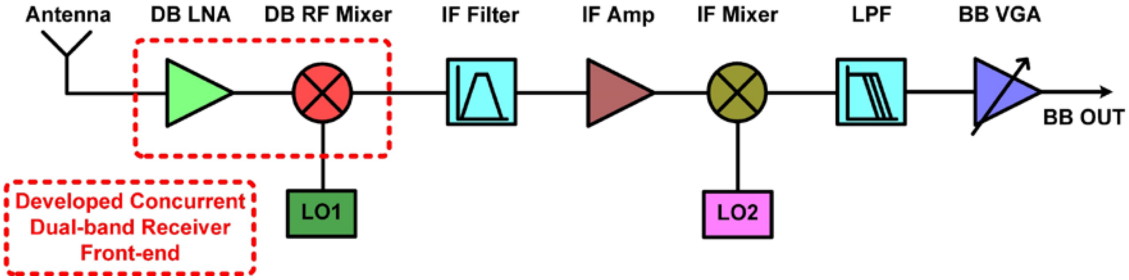

Fig. 7.1 Developed receiver front-end as part of a concurrent dual-band double-conversion receiver.

band load (Fig. 4.4) and the concurrent dual-band merged LNA and mixer employing the single-to-differential transformer feedback dual-band load (Fig. 6.1). Since the developed dual-band LNA exhibits the high gain of 21.8 dB at both passbands as well as the low NF of 2.4/2.5 dB at low/high-passband, respectively, it is used as the first building block of the proposed receiver front-end to increase overall receiver conversion gain and hence to reduce the total receiver NF. Thereafter, the merged LNA and mixer converts the single-ended dual passband input voltage signals into the differential current signals and down-converts them to the IF signals, simultaneously.

The developed dual-band LNA exhibits the passband peak gains at 23/36 GHz and the stopband notch at 30 GHz, while the developed dual-band merged LNA and mixer achieves the passband peak conversion gains at 24.5/36.5 GHz and the stopband notch at 30.6 GHz. Since both of the dual-band LNA and the dual-band merged LNA and mixer have the functionality of controlling the stopband rejection and the passband gain balance by adjusting the bias level of the second-stage inverting amplifier, the

TABLE 7.1
OPERATION MODES SUMMARY OF THE PROPOSED CONCURRENT DUAL-BAND RECEIVER FRONT-END

Receiver Front-end Operation Modes	Dual-band LNA Operation Modes	Merged LNA and Mixer Operation Modes
Rx Mode 1: Low Gain (LG)	Mode A: LGSRR	Mode C: LGGB
Rx Mode 2: Gain Balance (GB)	Mode B: HGGB	Mode C: LGGB
Rx Mode 3: High Gain (HG)	Mode B: HGGB	Mode D: HGSRR
Rx Mode 4: High SRR (SRR)	Mode A: LGSRR	Mode D: HGSRR
Rx Mode 5: Notch Balance (NB)	Transition between Rx Mode 3 and Rx Mode 4	

proposed receiver front-end has versatile operation modes by combining each operation mode of the dual-band LNA and the merged LNA and mixer.

The developed dual-band LNA has two representative operation modes: 1) low-gain and high SRR (Mode A: LGSRR) and 2) high-gain and gain balance (Mode B: HGGB). While, the developed merged LNA and mixer has two important operation modes with 1) low-gain and gain balance (Mode C: LGGB) and 2) high-gain and high SRR (Mode D: HGSRR). By combining these operation modes, the proposed receiver front-end exhibits four distinguishable operation mode and one unique transition mode as summarized in Table 7.1.

At Rx mode 1, the dual-band receiver front-end exhibits the lowest gain performance as well as the largest stopband notch at 30 GHz since the dual-band LNA is optimized to achieve the highest SRR. At Rx mode 2, the dual-band receiver achieves the best gain balance performance between each passbands with lower stopband attenuation. The dual-band receiver front-end achieves the highest gain and the lowest NF at Rx mode 3, and the 30.6-GHz stopband notch mainly occurs as the merged LNA and mixer is optimized to obtain high SRR. At Rx mode 4, the receiver front-end shows the largest stopband rejection performance at both 30 and 30.6 GHz with well-balanced gain and moderate NF performances. The dual-band receiver front-end also can be optimized to achieve the same stopband attenuation level with balanced notches at both 30 and 30.6 GHz at Rx mode 5.

7.2 Experimental and Simulated Results

Fig. 7.2 shows the microphotograph of the fabricated concurrent dual-band receiver front-end on a 0.18-μm BiCMOS process having f_T/f_{max} of 240/280 GHz [24]. It has a core area of 2.23 mm × 0.8 mm and was measured on-wafer. Since the dual-band LNA and the merged LNA and mixer have the 50-Ohm input/output load impedances, the GCPW line is used to connect between the output of dual-band LNA and the input of merged LNA and mixer.

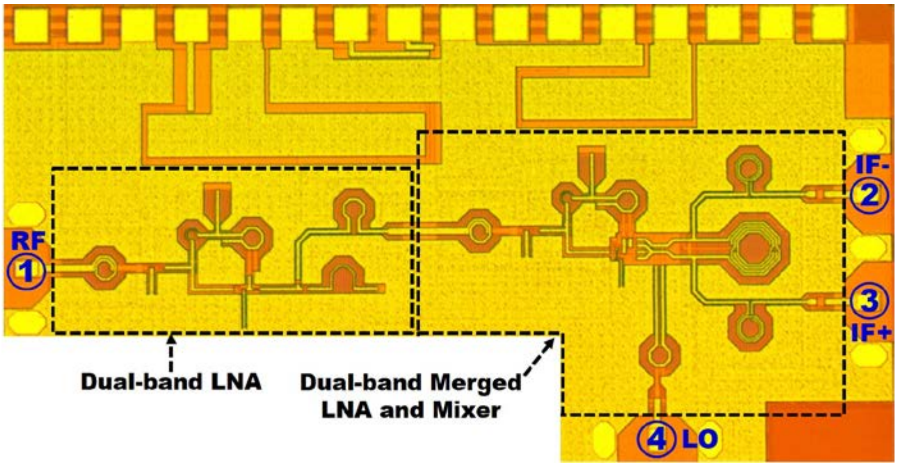

Fig. 7.2 Microphotograph of the fabricated concurrent dual-band receiver front-end consisting of the dual-band LNA shown in Fig. 4.4 followed by the dual-band merged LNA and mixer shown in Fig. 6.1.

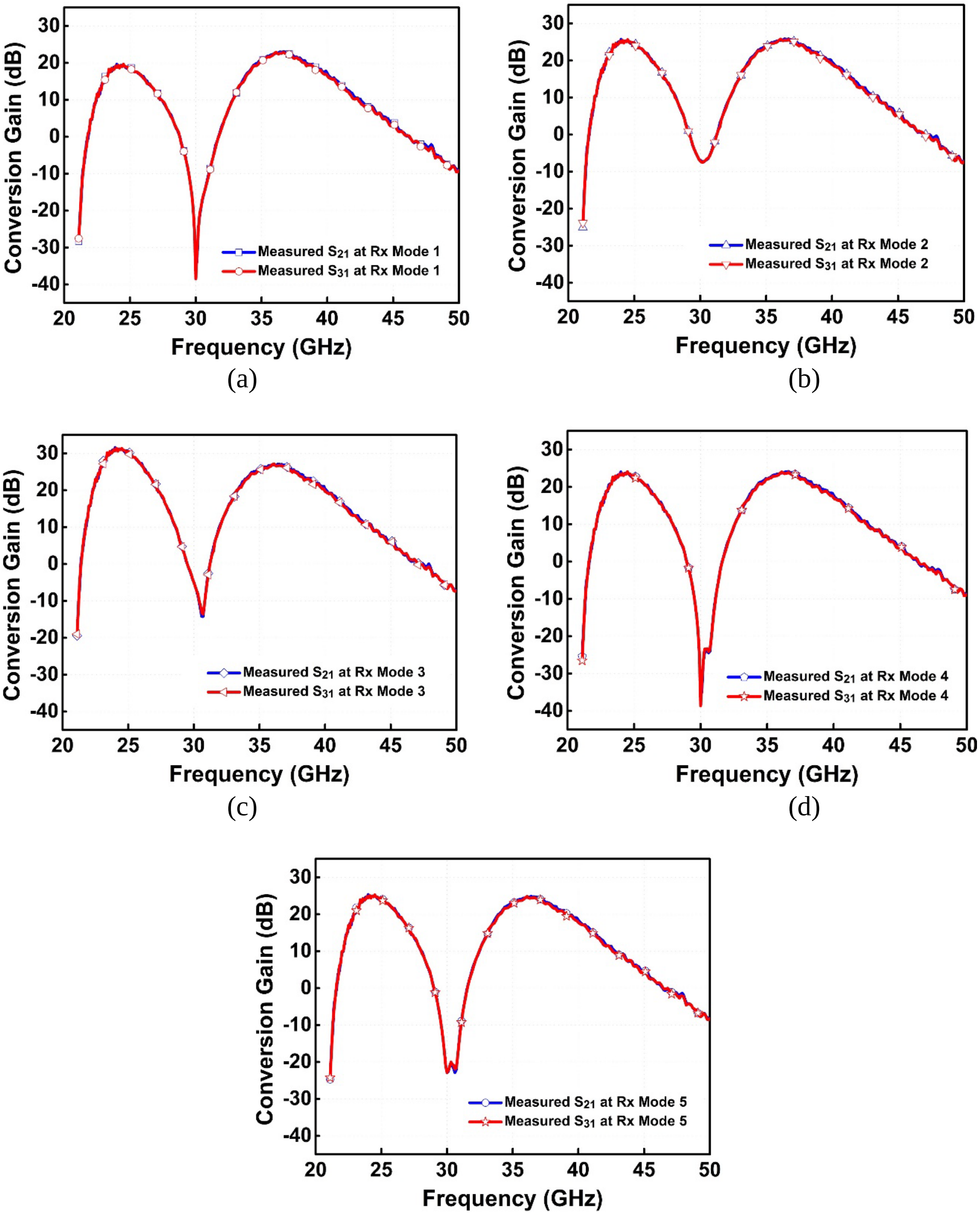

(a) (b)

(c) (d)

(e)

Fig. 7.3 Measured single-ended conversion gains of the receiver front-end for S_{21} and S_{31} paths: (a) Rx mode 1 for low-gain, (b) Rx mode 2 for passband gain balance, (c) Rx mode 3 for high-gain, (d) Rx mode 4 for high SRR, and (e) Rx mode 5 for stopband notch balance.

The dual-band LNA uses a 1.8-V supply voltage, while, the merged LNA and mixer operates with a 2.5-V supply voltage. The developed concurrent dual-band receiver front-end consumes the 112.5/123.4/153.7/137.5/139.3-mW power at Rx modes 1/2/3/4/5, respectively.

Figure 7.3 shows the measured conversion gain responses of the fabricated concurrent dual-band receiver front-end at five different receiver operation modes described in Table 7.1 and Fig. 7.4 shows the measured single-ended NF responses of the receiver front-end for Rx modes 1 to 4. The measured and simulated matching characteristics are also shown in Fig. 7.5. The measured results of conversion gain, NF, SRR, and passband gain difference are summarized in Table 7.2 in detail. In this dissertation, among the five representative operation modes, the measured results of two operation modes for Rx modes 3 and 4 are discussed as follows because they are related to the most important characteristics of the proposed receiver front-end, such as gain, NF and SRR.

At Rx mode 3 for high gain, the measured single-ended conversion gains of the developed concurrent dual-band receiver front-end for S_{21}/S_{31} paths are 31.6/31.3 dB at 24 GHz and 27.0/26.7 dB at 36.5 GHz, respectively. From the measured stopband notch of –14.2 dB at 30.6 GHz, the SRRs of 45.8/45.5 dB at low-band and 41.2/40.9 dB at high-band for respective S_{21}/S_{31} paths are obtained. The best NFs of 3.3/2.9 dB and 2.6/3.0 dB are obtained in the low and high passbands, respectively at Rx mode 3. The concurrent dual-band receiver front-end achieves the best gain and NF performances at Rx mode 3.

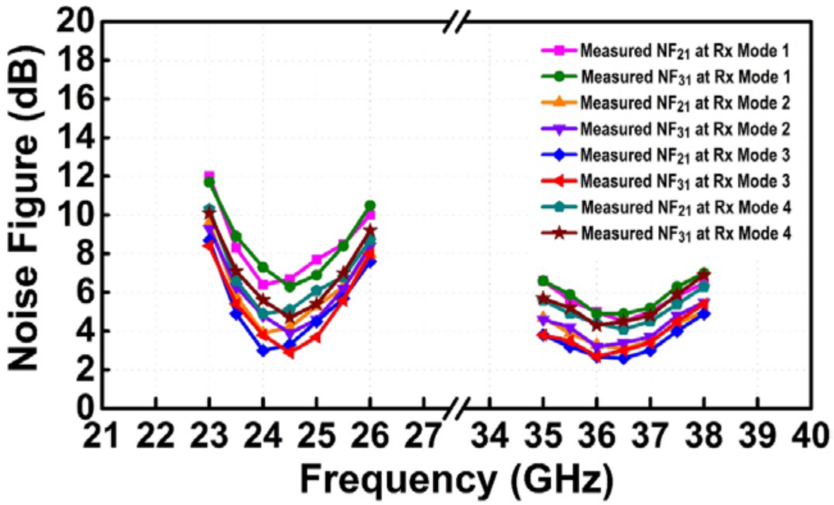

Fig. 7.4 Measured single-ended NFs at Port 2 and Port 3 (NF_{21}, NF_{31}).

At Rx mode 4 for high SRR, the measured conversion gains at 24 GHz and 36.5 GHz are identical as 24.0/23.6 dB for S_{21}/S_{31} paths, respectively. The measured maximum stopband notches of –38.2/–24.4 dB are obtained at 30/30.6 GHz, respectively. The calculated SRRs of 62.2/61.8 dB at low-band and high-band for respective S_{21}/S_{31} paths are exhibited. The best NFs of 5.1/4.7 dB and 4.1/4.5 dB are obtained in the low and high passbands, respectively, at Rx mode 4. To the best of our knowledge, the measured SRRs at Rx mode 4 of the developed concurrent dual-band receiver front-end are the best stopband performance up to date.

The measured matching responses at Rx mode 3 are shown in Fig. 7.5, and it is found that the matching frequencies were slightly shifted up at each port. It mainly originates from the smaller capacitance values on the fabricated die as compared to the capacitances used in the schematic design. For all Rx operation modes, it is shown that

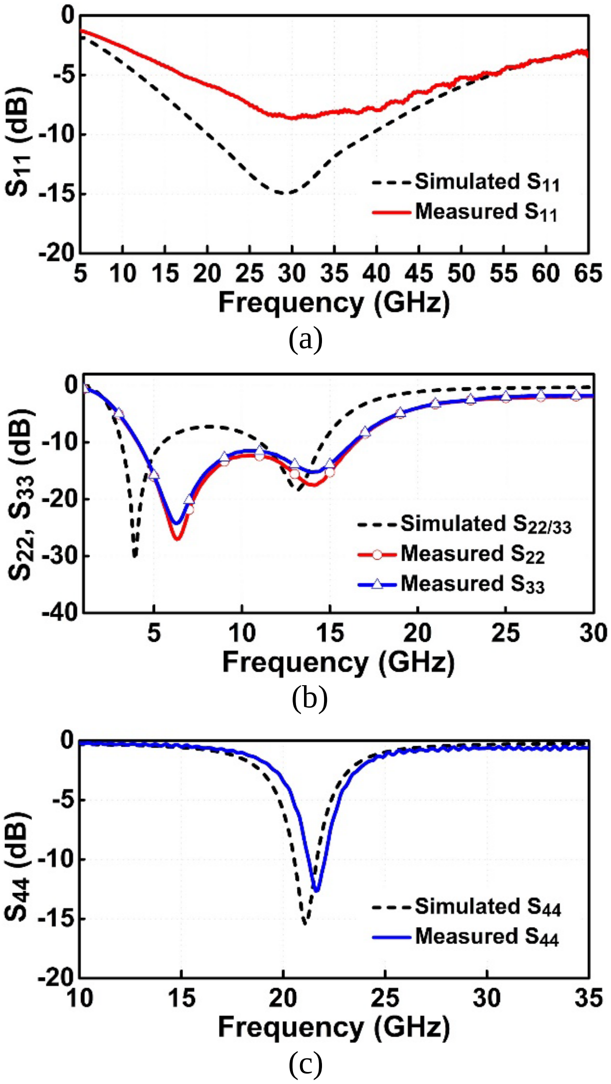

Fig. 7.5 Measured and simulated matching responses at: (a) RF input (Port1), (b) IF output (Ports 2 and 3), and (c) LO input (Port 4).

the matching responses have very little variation, and they are similar to those shown in Fig. 7.5. Even though, the matching frequencies were shifted up, it does not affect to the operation of the receiver front-end. The receiver front-end was measured with RF passband frequencies at 24.5/36.5 GHz, LO frequency at 21 GHz, and IF frequencies at 3.5/15.5 GHz ($f_{IF} = f_{RF} - f_{LO}$), accordingly.

TABLE 7.2
PERFORMANCE SUMMARY OF CONCURRENT DUAL-BAND RECEIVER FRONT-END

Receiver Front-end Operation Mode	Frequency (GHz)	Conversion Gain (S_{21} / S_{31}) (dB)	NF (NF_{21} / NF_{31}) (dB)	Stopband Rejection Ratio (dB)	Passband Gain Difference (S_{21} / S_{31}) (dB)	Input P_{1dB} ($IP_{1dB,21}$ / $IP_{1dB,31}$) (dBm)	Input IP_3 ($IIP_{3,21}$ / $IIP_{3,31}$) (dBm)
Rx Mode 1: Low Gain (LG)	24	19.6 / 19.3	6.7 / 6.3	57.7 / 57.4	3.3 / 3.2	–36.9 / –36.9	–27.9 / –28.1
	30	–38.1	–	–		–	–
	36.5	22.9 / 22.5	4.5 / 4.9	61.0 / 60.6		–43.5 / –43.4	–35.6 / –36.1
Rx Mode 2: Gain Balance (GB)	24	25.7 / 25.4	4.2 / 3.9	32.9 / 32.6	< 0.1 / < 0.1	–42.7 / –42.7	–33.5 / –33.9
	30.2	–7.2	–	–		–	–
	36.5	25.7 / 25.4	3.1 / 3.4	32.9 / 32.6		–46.7 / –46.7	–38.3 / –39.5
Rx Mode 3: High Gain (HG)	24	31.6 / 31.3	3.3 / 2.9	45.8 / 45.5	4.6 / 4.6	–43.3 / –43.3	–34.5 / –33.1
	30.6	–14.2	–	–		–	–
	36.5	27.0 / 26.7	2.6 / 3.0	41.2 / 40.9		–44.9 / –44.9	–37.3 / –35.5
Rx Mode 4: High SRR (SRR)	24	24.0 / 23.6	5.1 / 4.7	62.2 / 61.8	< 0.1 / < 0.1	–36.0 / –36.0	–26.1 / –24.7
	30 / 30.6	–38.2 / –24.4	–	–		–	–
	36.5	24.0 / 23.6	4.1 / 4.5	62.2 / 61.8		–42.3 / –42.3	–31.3 / –32.1
Rx Mode 5: Notch Balance (NB)	24	25.3 / 25.0	–	48.1 / 47.8	0.6 / 0.7	–	–
	30 / 30.6	–22.8 / –22.8	–	–		–	–
	36.5	24.7 / 24.3	–	47.5 / 47.1		–	–

Figure 7.6 shows the measured single-ended conversion gain responses for S_{21}/S_{31} paths by varying the LO power at Rx modes 1 to 4. It is found that the dual-band receiver front-end exhibits the flat conversion gain responses over the LO power level from around −5 to 5 dBm for all Rx modes. Therefore, the LO power of −2 dBm is used as a reference condition to measure the receiver front-end performances for all Rx operation modes.

Figure 7.7 shows the measured input P_{1dB} responses of the receiver front-end for Rx modes 1 to 4. At Rx mode 3, the measured input P_{1dB} ($IP_{1dB,21}$/$IP_{1dB,31}$) for the two signal paths (Ports 1 to 2 and 1 to 3) are identical as –43.3/–44.9 dB at 24.5/36.5 GHz, respectively. At Rx mode 4, the measured IP_{1dB} for two signal paths are –36.0/–42.3 dB at 24.5/36.5 GHz, respectively.

Figure 7.8 shows the measured input IP3 ($IIP_{3,21}$/$IIP_{3,31}$) for the two signal paths for Rx modes 1 to 4. The two-tone signals with 1-MHz spacing are applied for each passband located at 24.5/36.5 GHz. At Rx mode 3, the measured $IIP_{3,21}$/$IIP_{3,31}$ are –

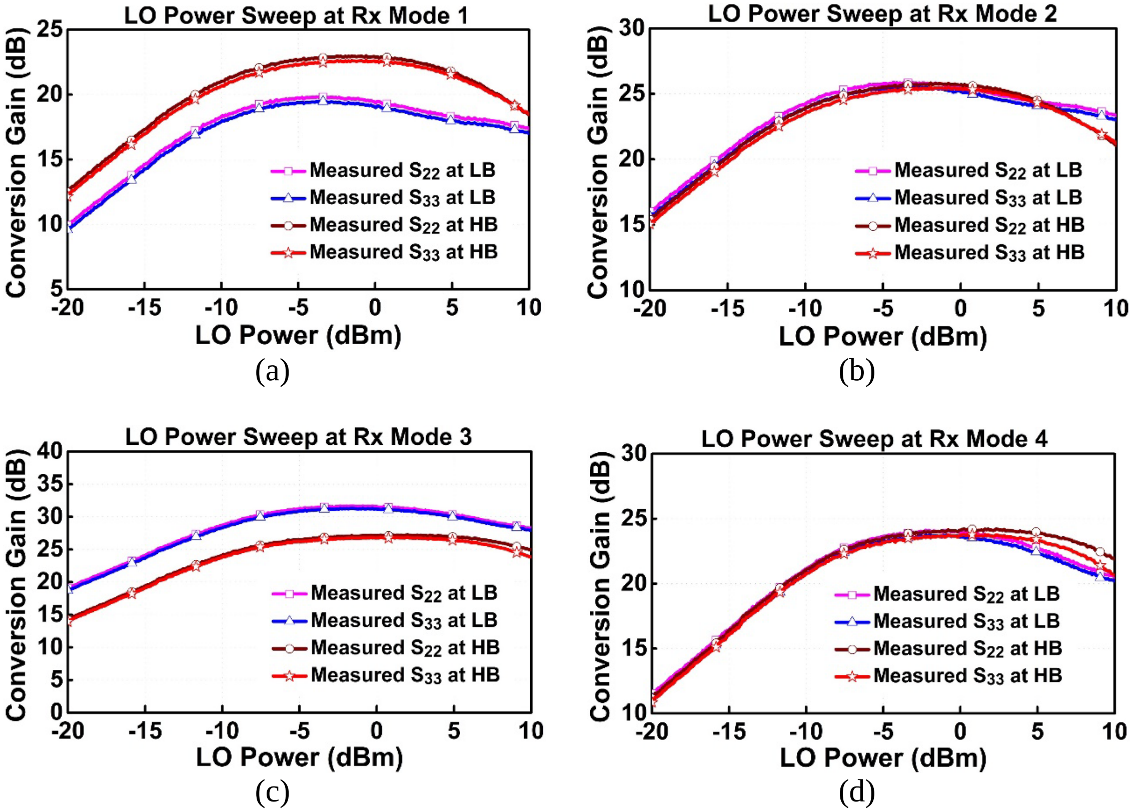

(a) (b)

(c) (d)

Fig. 7.6 Measured single-ended conversion gain for Ports 1 to 2 and 1 to 3 (S_{21}, S_{31}) as a function of LO power at: (a) Rx mode 1, (b) Rx mode 2, (c) Rx mode 3, and (4) Rx mode 4.

34.5/–33.1 dB at 24.5 GHz and –37.3/–35.5 dB at 36.5 GHz, respectively. At Rx mode 4, the measured IIP$_{3,21}$/IIP$_{3,31}$ are –26.1/–24.7 dB at 24.5 GHz and –31.3/–32.1 dB at 36.5 GHz, respectively. The detailed measured results of the fabricated concurrent dual-band receiver front-end for all Rx modes are summarized in Table 7.2.

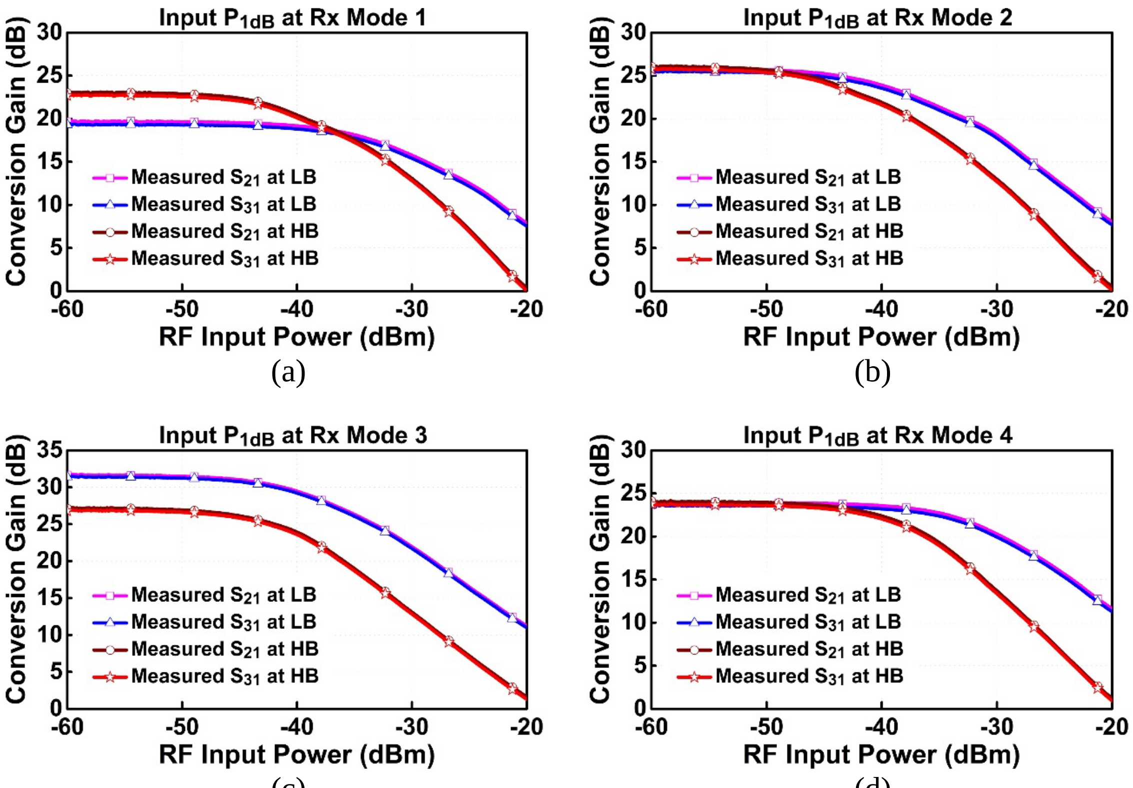

(a) (b)

(c) (d)

Fig. 7.7 Measured single-ended input P$_{1dB}$ for Ports 1 to 2 and 1 to 3 (S_{21}, S_{31}) as a function of RF power at: (a) Rx mode 1, (b) Rx mode 2, (c) Rx mode 3, and (4) Rx mode 4.

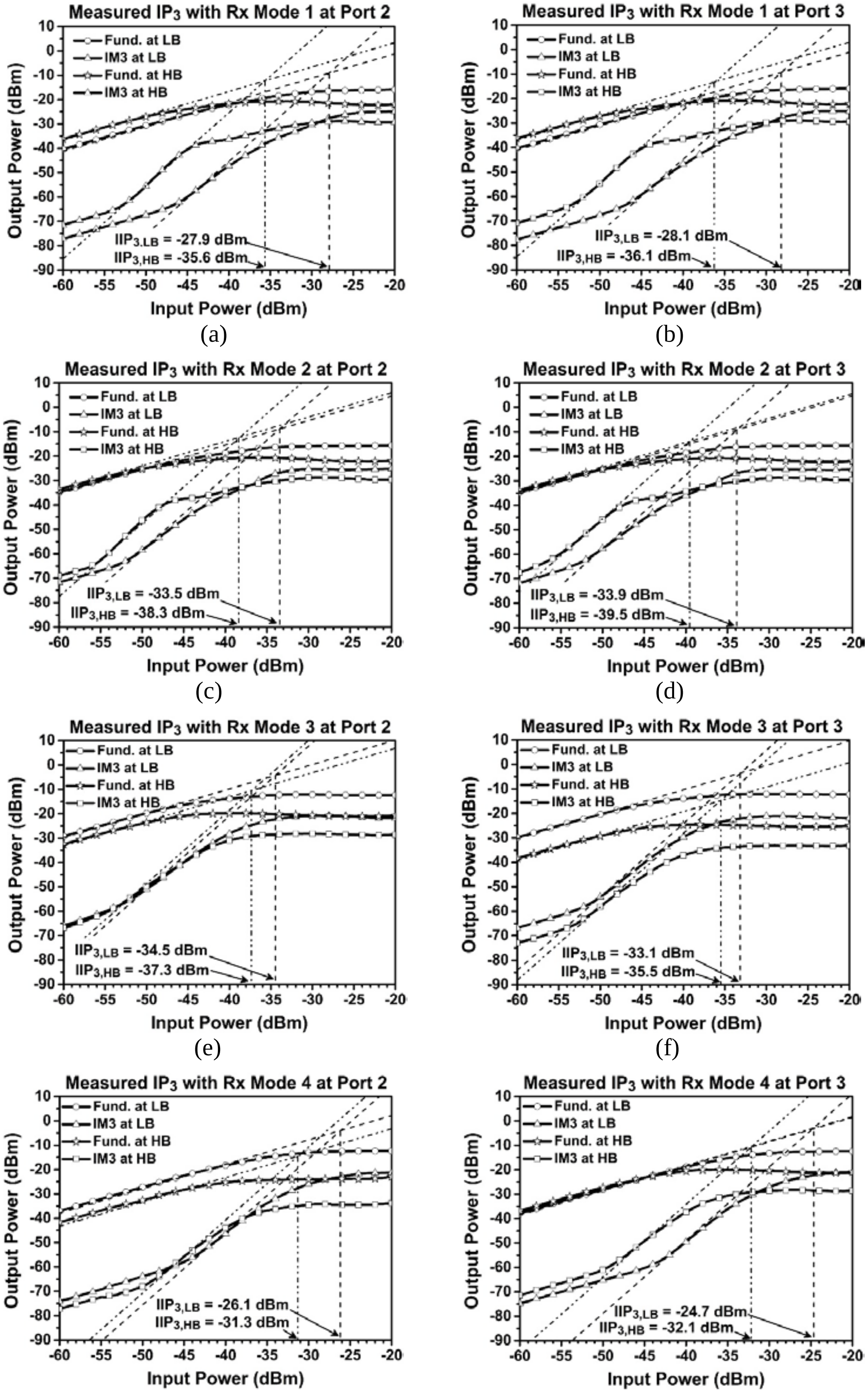

(a) (b)

(c) (d)

(e) (f)

(g) (h)

Fig. 7.8 Measured single-ended input IP$_3$: IIP$_{3,21}$ at Port 2 (a), (c), (e), (g) and IIP$_{3,31}$ at Port 3 (b), (d), (f), (h) for Rx modes 1 to 4, respectively.

TABLE 7.3
PORT-TO-PORT ISOLATION OF CONCURRENT DUAL-BAND RECEIVER FRONT-END

Receiver Front-end Operation Mode	Frequency (GHz)	RF-to-IF (P1-P2 / P1-P3) (dB)	LO-to-IF (P4-P2 / P4-P3) (dB)	LO-to-RF (P4-P1) (dB)
Rx Mode 1: Low Gain (LG)	24	11.2 / 16.1	37.3 / 34.6	59.8
	36.5	17.6 / 20.6		
Rx Mode 2: Gain Balance (GB)	24	5.8 / 10.2	38.0 / 34.5	59.5
	36.5	14.9 / 17.8		
Rx Mode 3: High Gain (HG)	24	–4.8 / –1	35.0 / 31.7	59.5
	36.5	8.9 / 10.1		
Rx Mode 4: High SRR (SRR)	24	2.3 / 6.2	34.7 / 31.9	59.7
	36.5	11.4 / 12.8		

The measured port-to-port isolation performances of the receiver front-end are also summarized in Table 7.3. The receiver front-end obtains excellent isolation performances larger than 31.7/59.5 dB for LO-to-IF/LO-to-RF ports, respectively. While, the receiver front-end exhibits lower isolation performances for RF-to-IF ports due to the fact that the developed receiver front-end does not include the IF filter (shown in Fig. 7.1) at its output.

Table 7.4 summarizes and compares the performances of both concurrent and switching dual-band receivers. Even though the concurrent dual-band receiver in [47] exhibits the maximum SRR of around 33 dB, it was only based on the simulation results and has not been fabricated. The concurrent dual-band receiver in [8] used a dual-band LNA followed by a wideband mixer, and it has the measured best SRR around 9.2 dB,

TABLE 7.4
PERFORMANCE COMPARISON OF DUAL-BAND RECEIVERS

Reference	Technology	Frequency (GHz)		Gain (S_{21}/S_{31}) (dB)	NF (NF_{21}/NF_{31}) (dB)	Input P_{1dB} ($IP_{1dB,21}/IP_{1dB,31}$) (dBm)	Input IP_3 ($IIP_{3,21}/IIP_{3,31}$) (dBm)	Stopband Rejection Ratio (dB)	Power (mW)	Area (mm^2)
[47][a] (Concurrent Dual-Band)	0.18-μm CMOS		2.45	17.6	3.5	—	—	33	84.3	4.165
			5.25	11.8	6.3	—	—	27		
[8] (Concurrent Dual-Band)	0.18-μm CMOS		3.96	23.2	5.2	–12.5	1	9.2	18	1.7
			7.128	22.8	5.3	–11.5	3.3	8.8		
[12][b] (Concurrent Dual-Band)	0.13-μm CMOS		8	10	8.2	–26	–17	—	68	15.6
			14	12	11.8	–17	–6	—		
[46] (Switching Dual-Band)	0.18-μm SiGe BiCMOS		24	21	8	—	–18	—	60	0.7
			31	18	9.5	—	–17	—		
[48] (Switching Dual-Band)	90-nm CMOS		2.5	27.5	—	–28	–16	—	42	0.35
			5.8	26.5	—	–27.1	–16.5	—		
This Work (Concurrent Dual-Band)	0.18-μm SiGe BiCMOS	Rx Mode 3	24.5	31.6 / 31.3	3.3 / 2.9	–43.3 / –43.3	–34.5 / –33.1	45.8 / 45.5	153.7	1.784
			36.5	27.0 / 26.7	2.6 / 3.0	–44.9 / –44.9	–37.3 / –35.5	41.2 / 40.9		
		Rx Mode 4	24.5	24.0 / 23.6	5.1 / 4.7	–36.0 / –36.0	–26.1 / –24.7	62.2 / 61.8	137.5	
			36.5	24.0 / 23.6	4.1 / 4.5	–42.3 / –42.3	–31.3 / –32.1	62.2 / 61.8		

[a] Full receiver including LO circuits. Only simulated performances have been reported.
[b] Fully integrated phased array receiver including LO and baseband circuits.

which is not sufficient in practical RF systems. The concurrent dual-band phased array receiver shown in [12] used a tunable current dual-band amplifier with one wideband input path and two separate output paths for low- and high-band. Since it has two independent amplifiers in each signal path, it requires additional power and area consumption. On the other hand, the dual-band receivers in [46] and [48] operate based on switching mechanism, so they can receive and process only one passband at a time.

The dual-band receiver in [46] actually used a wideband LNA and a wideband RF-to-IF down-conversion mixer for the receiver front-end followed by a 3.5/10.5-GHz switchable dual-band IF-to-BB down-conversion mixer. To the best of our knowledge, the developed concurrent dual-band receiver front-end achieves the highest gain and the best NF performances as well as the largest SRRs among the concurrent dual-band receivers reported to date, while operating at highest frequencies up to millimeter-wave region.

7.3 Summary and Conclusion

The 24.5/36.5-GHz concurrent dual-band receiver front-end composed of a concurrent dual-band LNA and a concurrent dual-band merged single-to-differential LNA and mixer has been developed successfully for various K-/Ka-band applications. By controlling the bias levels of second stage amplifiers of both dual-band LNA and merged LNA and mixer, the developed dual-band receiver front-end provide versatile receiver operation modes with the combination of the passband gain balance performances as well as the stopband rejection performances at two different notch frequencies according to the different bias levels. Since each Rx operation mode exhibits the unique passband conversion gain and stopband notch characteristics, the proposed concurrent dual-band receiver front-end can be used as an adaptive receiver front-end with great flexibility to overcome the various receiver path environment as well as the process, voltage, and temperature variations in practical RF systems.

CHAPTER VIII

SUMMARY AND CONCLUSION

The fully integrated multiband radio frequency (RF) receiver front-end and its building blocks for various Ku-/K-/Ka-band applications were successfully developed in 0.18-μm SiGe BiCMOS technologies. The developed receiver building blocks implementing various new feedback multiband load architectures achieved the unprecedented stopband rejection performances by overcoming the low quality (Q) factor originated from the integrated passive inductors used in existing multiband LNAs and receivers.

The 13.5/24/35-GHz concurrent tri-band LNA implementing a novel feedback tri-band load composed of two feedback notch filters was firstly presented. Comparative analysis and design principles of the conventional tri-band load and the proposed modified and feedback tri-band loads, and their use in tri-band LNA design were presented. The proposed feedback tri-band load overcomes the low Q-factor of integrated inductors, and hence provides superior stopband rejection performance. The developed 13.5/24/35-GHz concurrent tri-band LNA achieved stable and high SRRs of more than 30 dB without additional area and power consumption.

Two K-/Ka-band concurrent dual-band LNAs employing two different types of feedback dual-band loads were developed by significantly expanding the feedback notch technique used in the concurrent tri-band LNA. The 21.5/36.5-GHz concurrent dual-band LNA used an inductor feedback dual-band load and the 23/36-GHz concurrent dual-band LNA used a new transformer feedback dual-band load. The latter provides more degrees of freedom for the creation of the stopband and passbands as compared to the former. The dual-band LNAs have the unique characteristic to control the stopband rejection ratio by adjusting the bias level of second-stage amplifier. Both the developed concurrent dual-band LNAs achieved the best NF and gain-balance performances among the concurrent multiband LNAs reported at high microwave and millimeter-wave frequencies.

The new concurrent dual-band single-to-differential transformer feedback dual-band load as well as its use in the concurrent dual-band single-to-differential LNA were also presented. The designed concurrent dual-band single-to-differential LNA converts two simultaneous independent single-ended input signals at around 22 and 36 GHz into 180° out-of-phase differential signals at its output without any switching activity by employing the proposed single-to-differential transformer feedback dual-band load. The developed concurrent dual-band single-to-differential LNA achieved excellent gain, gain/phase balances, and NF performances as well as a great stopband rejection. The developed LNA is the first true concurrent dual-band single-to-differential amplifier operating up to millimeter-wave frequencies and without using switching mechanism.

The concurrent dual-band merged single-to-differential LNA and mixer implementing the proposed single-to-differential transformer feedback dual-band load was presented. The single-to-differential transformer feedback dual-band load was used as a concurrent dual-band transconductance (g_m) amplifier. With a 21-GHz single-ended LO signal, the down-converted dual IF bands are located at 3.5/15.5 GHz for two passband signals at 24.5/36.5 GHz, respectively. The developed merged LNA and mixer is the first fully integrated concurrent dual-band mixer operating up to millimeter-wave frequencies without using any switching mechanism.

The 24.5/36.5-GHz concurrent dual-band receiver front-end was finally presented. It consisted of the concurrent dual-band LNA using the single-to-single transformer feedback dual-band load and the concurrent dual-band merged LNA and mixer employing the single-to-differential transformer feedback dual-band load. The receiver front-end operates with RF passband frequencies at 24.5/36.5 GHz, LO frequency at 21 GHz, and IF frequencies at 3.5/15.5 GHz, accordingly. Since both of the dual-band LNA and the dual-band merged LNA and mixer have the functionality of controlling the stopband rejection and the passband gain balance by adjusting the bias level of second-stage inverting amplifier, the developed receiver front-end has versatile operation modes by combining each operation mode of the dual-band LNA and the merged LNA and mixer. The developed concurrent dual-band receiver front-end achieved the highest gain and the best NF performances as well as the largest SRRs, while operating at highest frequencies up to millimeter-wave region, among the concurrent dual-band receivers reported to date.

REFERENCES

[1] B. Bakkaloglu, P. Fontaine, A. N. Mohieldin, S. Peng, S. J. Fang, and F. Dülger, "A 1.5-V multi-mode quad-band RF receiver for GSM/EDGE/CDMA2K in 90-nm digital CMOS process," *IEEE J. Solid-State Circuits*, vol. 41, no. 5, pp. 1149–1159, May 2006.

[2] I. Vassiliou, K. Vavelidis, N. Haralabidis, A. Kyranas, Y. Kokolakis, S. Bouras, G. Kamoulakos, C. Kapnistis, S. Kavadias, N. Kanakaris, E. Metaxakis, C. Kokozidis, and H. Peyravi, "A 65 nm CMOS multistandard, multiband TV tuner for mobile and multimedia applications," *IEEE J. Solid-State Circuits*, vol. 43, no. 7, pp. 1522–1533, July 2008.

[3] M. Jeong, B. Kim, Y. Cho, Y. Kim, S. Kim, H. Yoo, J. Lee, J. K. Lee, K. S. Jung, J. Lee, J. Lee, H. Yan, G. Taylor, and B.-E. Kim, "A 65nm CMOS low-power small-size multistandard, multiband mobile broadcasting receiver SoC," in *IEEE Int. Solid-State Circuits Conf. Tech. Dig.*, Feb. 2010, pp. 460–461.

[4] V. Giannini, P. Nuzzo, C. Soens, K. Vengattaramane, J. Ryckaert, M. Goffioul, B. Debaillie, J. Borremans, J. V. Driessche, J. Craninckx, and M. Ingels, "A 2-mm^2 0.1–5 GHz software-defined radio receiver in 45-nm digital CMOS," *IEEE J. Solid-State Circuits*, vol. 44, no. 12, pp. 3486–3498, July 2008.

[5] H. Hashemi, and A. Hajimiri, “Concurrent multiband low-noise amplifiers—theory, design, and applications,” *IEEE Trans. Microw. Theory Techn.,* vol. 50, no. 1, pp. 288–301, Jan. 2002.

[6] Q. H. Huang, D. R. Huang, and H. R. Chuang, “A fully-integrated 2.4/5.7 GHz concurrent dual-band 0.18 μm CMOS LNA for an 802.11 WLAN direct conversion receiver,” *Microwave J.*, vol. 47, pp. 76–88, Feb. 2004.

[7] C. P. Moreira, E. Kerherve, P. Jarry, and D. Belot, “A concurrent fully-integrated BiFET LNA for W-CDMA/IEEE 802.11a applications,” in *IEEE Bipolar/BiCMOS Circuits Technol. Meeting Dig.*, 2006, pp. 1–4.

[8] G. Cusmai, M. Brandolini, P. Rossi, and F. Svelto, “A 0.18-μm selective receiver front-end for UWB applications,” *IEEE J. Solid-State Circuits*, vol. 41, no. 8, pp. 1764–1771, Aug. 2006.

[9] Y. T. Lin, T. Wang, and S. S. Lu, “Fully integrated concurrent dual-band low-noise amplifier with suspended inductors in SiGe 0.35 μm BiCMOS technology,” *Electron. Lett.*, vol. 44, no. 9, pp. 563–564, Apr. 2008.

[10] H.-S. Jhon, I. Song, J. Jeon, H. Jung, M. Koo, B.-G. Park, J.D. Lee, and H. Shin, “8 mW 17/24 GHz dual-band CMOS low-noise amplifier for ISM-band application,” *Electron. Lett.*, vol. 44, no. 23, pp. 1353–1354, Nov. 2008.

[11] K. Hsieh, H. Wu, K. Tsai, and C. C. Tzuang, “A dual-band 10/24-GHz amplifier design incorporating dual-frequency complex load matching,” *IEEE Trans. Microw. Theory Techn.*, vol. 60, no. 6, pp. 1649–1657, Jan. 2012.

[12] S. Jeon, Y. J. Wang, H. Wang, F. Bohn, A. Natarajan, A. Babakhani, and A. Hajimiri, “A scalable 6-to-18 GHz concurrent dual-band quad-beam phased-array receiver in CMOS,” *IEEE J. Solid-State Circuits*, vol. 43, no. 12, pp. 2660–2673, Dec. 2008.

[13] C. W. Ang, Y. Zheng, and C. H. Heng, “A multi-band CMOS low noise amplifier for multi-standard wireless receivers,” in *IEEE Int. Circuits Syst. Symp. Dig.*, 2007, pp. 2802–2805.

[14] C. F. Jou, K. H. Cheng, E. T. Lu, and Y. Wang, “Design of a fully integrated concurrent triple-band CMOS low noise amplifier,” in *IEEE Midwest Circuits Syst. Symp. Dig.*, 2003, vol.3, pp. 1239–1242.

[15] C. Y. Kao, Y. T. Chiang, and J. R. Yang, “A concurrent multi-band low-noise amplifier for WLAN/WiMAX applications,” in *IEEE Int. Electron./Inform. Technol. Conf. Dig.*, 2008, pp. 514–517.

[16] *SBC18H2 Design Manual*. Newport Beach, CA, USA: Jazz Semiconduct., 2013.

[17] IE3D, HyperLynx 3-D EM. Mentor Graphics, Wilsonville, OR, USA, 2013. [Online]. Available: http://www.mentor.com/products/pcb-system-design/circuit-simulation/hyperlynx-3d-em

[18] M. El-Nozahi, E. Sanchez-Sinencio, and K. Entesari, “A millimeter-wave (23–32 GHz) wideband BiCMOS low-noise amplifier,” *IEEE J. Solid-State Circuits,* vol. 45, no. 2, pp. 289–299, Feb. 2010.

[19] B. Razavi, *Design of Analog CMOS Integrated Circuits*. NewYork, NY, USA: McGraw-Hill, 2001.

[20] G. Gonzalez, *Microwave Transistor Amplifiers Analysis and Design*. Upper Saddle River, NJ, USA: Prentice-Hall, 1997.

[21] J. Lee and C. Nguyen, “A concurrent dual-band low-noise amplifier for K- and Ka-band applications in SiGe BiCMOS technology,” in *Proc. IEEE 2013 Asia-Pacific Microw. Conf.*, Nov. 2013, pp. 258–260.

[22] J. Lee and C. Nguyen, “A 13/24/35-GHz concurrent tri-band LNA with feedback notches,” in *IEEE Top. Silicon Monolithic Integr. Circuits RF Syst. Meeting Dig.*, Jan. 2013, pp. 252–254.

[23] J. Lee and C. Nguyen, “A concurrent tri-band low-noise amplifier with a novel tri-band load resonator employing feedback notches,” *IEEE Trans. Microw. Theory Techn.*, vol. 61, no. 12, pp. 4195–4208, Dec. 2013.

[24] *SBC18H3 Design Manual*. Newport Beach, CA, USA: Jazz Semiconductor Inc., 2014.

[25] K. Kim and C. Nguyen, “A concurrent *Ku/K/Ka* tri-band distributed power amplifier with negative-resistance active notch using SiGe BiCMOS process,” *IEEE Trans. Microw. Theory Techn.*, vol. 62, no. 1, pp. 125–136, Jan. 2014.

[26] B. Welch, K. T. Kornegay, H.-M. Park, and J. Laskar, “A 20-GHz low-noise amplifier with active balun in a 0.25-μm SiGe BICMOS technology,” *IEEE J. Solid-State Circuits*, vol. 40, no. 10, pp. 2092–2097, Oct. 2005.

[27] J.-F. Yeh, C.-Y. Yang, H.-C. Kuo, and H.-R. Chuang, “A 24-GHz transformer-based single-in differential-out CMOS low-noise amplifier,” in *Proc. IEEE Radio Frequency Integrated Circuits Symp.*, June 2009, pp. 299–302.

[28] E. V. D. Heijden, H. Veenstra, D. Hartskeerl, M. Notten and D. V. Goor, “Low noise amplifier with integrated balun for 24 GHz car radar,” in *IEEE Top. Silicon Monolithic Integr. Circuits RF Syst. Meeting Dig.*, Jan. 2008, pp. 78–81.

[29] K. Tsutsumi, R. Inagaki, T. Nakai, R. Takeuchi, and E. Taniguchi, “A 20 GHz low noise CMOS active balun using asymmetric transformer,” in *Proc. IEEE Asia-Pacific Microw. Conf.*, Nov. 2014, pp. 423–425.

[30] Y. Jin, M. Spirito, and J. Long, “A 60 GHz-band millimeter-wave active balun with ±5° phase error,” in *Proc. IEEE European Microw. Integr. Circuits Conf.*, Sep. 2010, pp. 210–213.

[31] H.-H. Chiang, F.-C. Huang, C.-S. Wang, and C.-K. Wang, “A 90 nm CMOS V-band low-noise active balun with broadband phase-correction technique,” *IEEE J. Solid-State Circuits*, vol. 46, no. 11, pp. 2583–2591, Nov. 2011.

[32] C. Viallon, D. Venturin, J. Graffeuil, and T. Parra, “Design of an original K-band active balun with improved broadband balanced behavior,” *IEEE Microw. Wireless Compon. Lett.*, vol. 15, no. 4, pp. 280–282, Apr. 2005.

[33] K. Jung, W. R. Eisenstadt, R. M. Fox, A. W. Ogden, and J. Yoon, “Broadband active balun using combined cascode–cascade configuration,” *IEEE Trans. Microw. Theory Techn.*, vol. 56, no. 8, pp. 1790–1796, Aug. 2008.

[34] B.-J. Huang, B.-J. Huang, K.-Y. Lin, and H. Wang, “A 2–40 GHz active balun using 0.13 μm CMOS process,” *IEEE Microw. Wireless Compon. Lett.*, vol. 19, no. 3, pp. 164–166, Mar. 2009.

[35] A. Gharib, R. Weigel, and D. Kissinger, “A 70 GHz bandwidth low-power active balun employing common-collector resistive feedback in 0.35 μm bipolar SiGe technology,” in *Proc. IEEE MTT-S International Microw. Symp.*, June 2014, pp. 1–3.

[36] S.-H. Weng, H.-Y. Chang, and C.-C. Chiong, “A DC–21 GHz low imbalance active balun using Darlington cell technique for high speed data communications,” *IEEE Microw. Wireless Compon. Lett.*, vol. 19, no. 11, pp. 728–730, Nov. 2009.

[37] M. Ferndahl and H.-O. Vickes, "The Matrix Balun—A transistor-based module for broadband applications," *IEEE Trans. Microw. Theory Techn.*, vol. 57, no. 1, pp. 53–60, Jan. 2009.

[38] A. Awny, C. Wipf, J. C. Scheytt, and A. Thiede, "Broadband 31–65 GHz inductorless active balun with 12.4 dB gain in 0.13 μm SiGe:C BiCMOS technology," in *Proc. IEEE European Microw. Integr. Circuits Conf.*, Oct. 2011, pp. 652–655.

[39] S. Wang and W.-J. Lin, "A 10/24-GHz CMOS/IPD monopulse receiver for angle-discrimination radars," *IEEE Trans. Circuits Syst. I, Reg. Papers*, vol. 61, no. 10, pp. 2999–3006, Oct. 2014.

[40] C. Huynh and C. Nguyen, "New technique for synthesizing concurrent dual-band impedance-matching filtering networks and 0.18-μm SiGe BiCMOS 25.5/37-GHz concurrent dual-band power amplifier," *IEEE Trans. Microw. Theory Techn.*, vol. 61, no. 11, pp. 3927–3939, Nov. 2013.

[41] J. Wu, P. Jiang, D. Chen, and J. Zhou, "A dual-band LNA with active balun for GNSS receivers," in *Proc. 10th IEEE International Conf. Solid-State Integr. Circuit Tech.*, Nov. 2010, pp. 665–667.

[42] V. Chironi, S. D'Amico, M. D. Matteis, and A. Baschirotto, "A dual-band balun LNA resilient to 5–6 GHz WLAN blockers for IR-UWB in 65nm CMOS," in *Proc. IEEE International Conf. IC Design & Tech.*, May 2013, pp. 171–174.

[43] T.A. Abdelrheem, H.Y. Elhak, and K.M. Sharaf, “A concurrent dual-band mixer for 900-MHz/1.8GHz RF front-ends,” in *IEEE Midwest Circuits Syst. Symp. Dig.*, 2003, vol.3, pp. 1291–1294.

[44] R.-L. Wang, Y.-K. Su, C. H. Liu, S.-C. Hung, P.-J. Yang, Y.-S. Lin, “A concurrent dual-band mixer with on-wafer balun for multi-standard applications,” *IEEE Asia Pacific Circuits Syst. Conf. Dig.*, 2008, pp. 304–307.

[45] B. R. Jackson and C. E. Saavedra, “A dual-band self-oscillating mixer for C-band and X-band applications,” *IEEE Trans. Microw. Theory Techn.*, vol. 58, no. 2, pp. 318–323, Feb. 2010.

[46] M. El-Nozahi, A. Amer, E. Sánchez-Sinencio, and K. Entesari, “A millimeter-wave (24/31-GHz) dual-band switchable harmonic receiver on 0.18-μm SiGe Process,” *IEEE Trans. Microw. Theory Techn.*, vol. 58, no. 11, pp. 2717–2730, Nov. 2010.

[47] C. F. Jou, K.-H. Cheng, W.-C. Lien, C. H. Wu, C. H. Yen, “Design of concurrent dual-band receiver front-end in 0.18um CMOS for WLANs IEEE 802.11a/b/g applications,” in *IEEE Midwest Circuits Syst. Symp. Dig.*, 2004, vol.1, pp. I-177–I-180.

[48] H.-K. Chen, K.-T. Lin, T. Wang, and S.-S. Lu, “A compact-size dual-band (tri-mode) receiver front-end with switched harmonic mixer and technology scaling,” in *Proc. IEEE Radio Frequency Integrated Circuits Symp.*, June 2011, pp. 1–4.